Towards Clinical Development and Implementation of Fast MR Spectroscopic Imaging Techniques

by

Nutandev Bikkamane Jayadev

A Dissertation Presented in Partial Fulfillment
of the Requirements for the Degree
Doctor of Philosophy

Approved April 2021 by the
Graduate Supervisory Committee:

Vikram Kodibagkar, Chair
John Chang
Ryan Robison
Barbara Smith
Sung-Min Sohn

ARIZONA STATE UNIVERSITY

May 2021

ABSTRACT

Magnetic resonance spectroscopic imaging (MRSI) is a non-invasive technique that offers a unique ability to provide the spatial distribution of relevant biochemical compounds (metabolites). The 'spectrum' of information provided by MRSI is used as biomarkers for the differential diagnosis of several diseases such as cancer or neurological disorders. Treatment responsive brain tumors can appear similar to non-responsive tumors on conventional anatomical MR images, earlier in the therapy, leading to a poor prognosis for many patients. Biomarkers such as lactate are particularly of interest in the oncological studies of solid tumors to determine their energy metabolism, blood flow, and hypoxia.

Despite the capability of nearly all clinical MRI scanners to perform MRSI only limited integration of MRSI into routine clinical studies has occurred to date. The major challenges affecting its true potential are the inherently long acquisition time, low signal-to-noise (SNR) of the signals, overlapping of spectral lines, or the presence of artifacts. The goal of this dissertation work is to facilitate MRSI in routine clinical studies without affecting the current patient throughput.

In this work, the Compressed Sensing (CS) strategy was used to accelerate conventional Point RESolved Spectroscopy (PRESS) MRSI by sampling well below the Shannon-Nyquist limit. Two undersampling strategies, namely the pseudo-random variable density and a novel *a priori* method was developed and implemented on a clinical scanner. Prospectively undersampled MRSI data was acquired from patients with various brain-related concerns. Spatial-spectral post processing and CS reconstruction pipeline was developed for multi-channel undersampled data. The fidelity of the CS-MRSI method was determined by comparing the CS reconstructed data to the fully sampled data. Statistical

results showed that the *a priori* approach maintained high spectral fidelity compared to the fully sampled reference for an 80% reduction in scan time. Next, an improvement to the CS-MRSI reconstruction was achieved by incorporating coil sensitivity maps as support in the iterative process. Further, a CS-MRSI-based fast lactate spectroscopic imaging method was developed and implemented to achieve complete water and fat suppression for accurate spatial localization and quantification of lactate in tumors. *In vitro* phantoms were developed, and the sequence was tested to determine the efficacy of CS-MRSI for low SNR signals, the efficacy of the CS acceleration was determined with statistical analysis.

DEDICATION

To my family and friends

ACKNOWLEDGMENTS

My Ph.D. journey has been a humbling experience and would not have reached this stage without the contributions of several individuals. First, I would like to express my sincere gratitude to my advisor Dr. Vikram Kodibagkar whose endless guidance and support have made this dissertation possible. His meticulous scrutiny, scientific approach, and enthusiasm have helped me shape my research to a great extent. I have learned from him to persevere. I owe it to him for uplifting my spirits during my lows and for always being available to address my concerns.

I would like to express my sincere thanks to Dr. John Chang at Banner MD Anderson Cancer Center for his unwavering support and encouragement. His formidable knowledge, insights and our numerous discussions have inspired me to explore further challenges at the clinical front. I am grateful to him for providing unlimited access to the MR scanner, recruiting subjects and providing the necessary resources for the study. I would like to thank the members of my committee: Dr. John Chang, Dr. Ryan Robison, Dr. Barbara Smith, and Dr. Sung-Min Sohn for their valuable inputs and guidance during the degree.

I would also like to thank Ms. Rhonda Hansen and Mr. David Baca at BMDACC for sharing their knowledge and experiences on routine clinical studies and for adjusting their schedules to make time for my research scans. I would like to extend my thanks to all members of the ProBE lab, especially Shubangi, Rohini, Babak, Sulagna, Richard, John, Yuka, and Chris for the fond memories and companionship over the years. I would like to

thank Munish for our numerous discussions on MR and his insights in developing MRI phantoms.

I would like to thank my Master's mentor Dr. Sairam Geethanath for invoking the researcher in me and for being a source of motivation and inspiration.

I am grateful to my parents, Ravikala and Jayadev, my sister Namratha and my wife Subhashini for their unwavering love and support. Thank you for the cheers and celebrations of my smallest of achievements. I would like to thank my friends: Vimala, Charan, Tejas, Vinay, Shruthi for all their support and encouragement. Thank you for making me feel at home in Arizona. I would like to thank my friends Ajit, Sachin, Manasi, and Padmashree, living outside of the US, for keeping in touch and checking on my health and well-being.

TABLE OF CONTENTS

Page

CHAPTER Page

LIST OF TABLES

Table Page

LIST OF FIGURES

Figure Page

Figure Page

Figure Page

Figure Page

Figure Page

CHAPTER 1

INTRODUCTION

Proton Magnetic resonance spectroscopic imaging (^{1}H MRSI) is a well-established method for the analysis and quantification of various metabolites present in tissue under investigation [1-7]. Due to its high sensitivity to the physiology and biochemistry of the tissue, irregular changes in metabolite concentration can be detected to assess disease conditions or their precursors [8 - 10]. For example, treatment responsive brain tumors can appear similar to non-responsive tumors on conventional anatomical MR images, earlier in the therapy, leading to a poor prognosis for many patients. Since metabolic changes precede structural changes, MRSI can be used for accurate and early detection of the extent and progression of the tumor [11-14]. Metabolite profiles of brain tumors for the major metabolites have been studied previously. Choline (Cho), creatine (Cr), N-acetyl aspartate (NAA), lactate (Lac) and lipid (lip), are some of the important metabolic markers. A general marker of brain tumors is the elevation of Cho, which is due to increased membrane turnover in neoplasms, and the reduction of the neuronal marker NAA. Furthermore, Cr reflects cellular bioenergetic and Lac is a marker of anaerobic metabolism. These markers together have been used in the investigation of diagnosis, grading, therapy and prognosis for patients with brain tumor.

While MRSI has been shown to be capable of providing clinically useful information associated with disease processes or treatment, it has not had much impact on clinical care and its use remains largely confined to the research community. This is because of several technical limitations which make it cumbersome to employ MRSI exams in a practical setting. Its inherently long acquisition time is one of the major deterrent

factors. Other limiting factors include low signal-to-noise ratio (SNR), insufficient water, and lipid suppression and requirement of higher-order shimming to maintain magnetic field homogeneity [15, 16]. These challenges and several other practical constraints related to patient compliance causes considerable compromises in terms of the data acquisition process. Therefore, translation of MRSI exams to regular clinical practice is challenging and less prevalent.

Considerable progress has been made to improve the sensitivity of the clinical scanners for the accurate detection of metabolites. The approval of higher field strengths for clinical use and the use of multichannel receive and transmit radio frequency (RF) coils have led to improvements in the SNR and spectral resolution. Over the years, numerous fast scanning procedures and data acquisition methods have been developed. However, these methods rely on additional hardware and software support from the vendor and have trade-offs in SNR, bandwidth or spectral resolution.

Compressed sensing (CS) has the potential to resolve the long acquisition drawback of MRSI [17]. CS combines many mathematical principles together, including the stochastic statistics and the mathematical optimization, to become a framework that can efficiently acquire and reconstruct a full-length signal from its highly undersampled measurements. Retrospective studies by Geethanath et al. [18] and Shankar et al. [19, 20] have demonstrated its application to MRSI to achieve a scan time reduction up to 80%.

In this work we develop and implement the CS-MRSI method on a clinical scanner to accelerate the conventional MRSI by sampling well below the Shannon-Nyquist limit. The iterative reconstruction framework is optimized and improved using *a priori* support information. We further demonstrate its application to lactate imaging.

This thesis is organized as follows:

Chapter 2 provides a brief overview of relevant background on MRSI data acquisition, post processing and the challenges affecting its inclusion in routine clinical studies. The compressed sensing method and its application to MRSI is also discussed.

Chapter 3 describes the clinical implementation of undersampled data acquisition based on CS. Two undersampling strategies namely the variable density and *a priori* methods were compared to achieve an 80% reduction is data time. A framework for CS reconstruction for multi-channel undersampled data was developed.

Chapter 4 describes the various procedures and challenges involved in CS-MRSI implantation at the clinic

Chapter 5 describes the development of an improved CS reconstruction framework using coil sensitivity weighting of the undersampled data.

Chapter 6 describes the application of the CS-MRSI framework for fast lactate imaging. Lactate Selective Multiple Quantum Coherence (SelMQC) sequence was implemented on a clinical scanner for accurate detection lactate with complete water and fat suppression.

Chapter 7 summarizes the major results of this study and proposes future studies.

CHAPTER 2

BACKGROUND AND LITERATURE REVIEW

This chapter provides a short overview of magnetic resonance (MR) scanners and reviews the basic magnetic resonance imaging (MRI), magnetic resonance spectroscopy (MRS) principles and how the two techniques coalesce as magnetic resonance spectroscopic imaging (MRSI). The focus is specifically set on ^{1}H MRSI, its implication at the clinic and the various challenges involved in its inclusion in routine clinical studies. Readers may consult the following books for a more detailed description of the topics: Magnetic resonance imaging: physical principles of the basic MR physics and sequence design by Robert Brown et al., *In vivo* NMR spectroscopy by Robin de Graff, and Clinical MR spectroscopy first principles by Nouha Salibi et al.

Next, a short overview of compressed sensing (CS) is provided with conditions necessary and fulfilled by MRSI for CS acceleration. This chapter closes with the previous research demonstrating in its CS-MRSI, laying the foundation for the current dissertation topic.

2.1 Introduction to Magnetic Resonance Imaging and Spectroscopy

2.1.1 MR Basics

Magnetic resonance originates form the interaction between an atom and an external magnetic field [21]. The nucleus has an intrinsic nuclear spin or nuclear spin angular momentum, which is proportional to the nuclear spin quantum number, *I*. The spin quantum number takes on multiples of $\frac{1}{2}$ values and can be + or – such that

$$I = 0, \pm\frac{1}{2}, \pm 1, \pm\frac{3}{2}, .. \tag{2.1}$$

Based on the atomic and mass number of an atom the spin of the nucleus is determined. Nuclei with non-zero nuclear spin interact with an external magnetic field, applied or resulting from local electronic configuration [22,23]. Under certain experimental conditions thisese properties provide us with a tool to probe the physical and chemical properties of materials. When protons are placed in a strong homogeneous magnetic field, the individual spins create an angular magnetic moment [24]. This moment precesses around the axis of the applied magnetic field with a frequency called as Larmor frequency (ω_0), is determined by the applied external homogenous magnetic field (B_0) and the gyromagnetic ratio (γ), which is constant for a given atom and is given by

$$\omega_0 = \gamma B_0 \tag{2.2}$$

Similar spins grouped together form spin isochromats resulting in a net magnetization vector (M_z) whose unit vector is aligned along B_0. Application of a RF pulse at resonant frequency transfers energy to the spins tipping them into the orthogonal plane. The excited spins tend to return to their ground state (i.e. along B_0) in form of a decaying sinusoid signal; free induction decay (FID). This is supported by spin-spin interactions and spin-lattice interactions, in general referred to as T_1 and T_2 relaxations [25] respectively. The former is attributed to energy exchange between the protons and their environment, returning the excited system to its thermal equilibrium and the latter is attributed to the effects of dipole-dipole interaction and diffusion of the molecules under the inhomogeneous magnetic fields. The Bloch equations describe these mechanisms.

$$\frac{dM}{dt} = M \times \gamma B + \begin{pmatrix} -M_x/T_2 \\ -M_y/T_2 \\ (M_0 - M_z)/T_1 \end{pmatrix} \tag{2.3}$$

In one dimensional (1D) experiments, time-varying signals detected from precessing magnetization is given by

$$S(t) = \int M_{\perp}(r) B_{\perp}(r) e^{-i\phi} dr \tag{2.4}$$

where, $S(t)$ is the detected signal, $M_{\perp}(r)$ is the transverse magnetization, $B_{\perp}(r)$ is the external magnetic field, ϕ is the phase of the magnetization vector, are r is the distance. The phase evolution given by

$$\phi = \omega . t \tag{2.5}$$

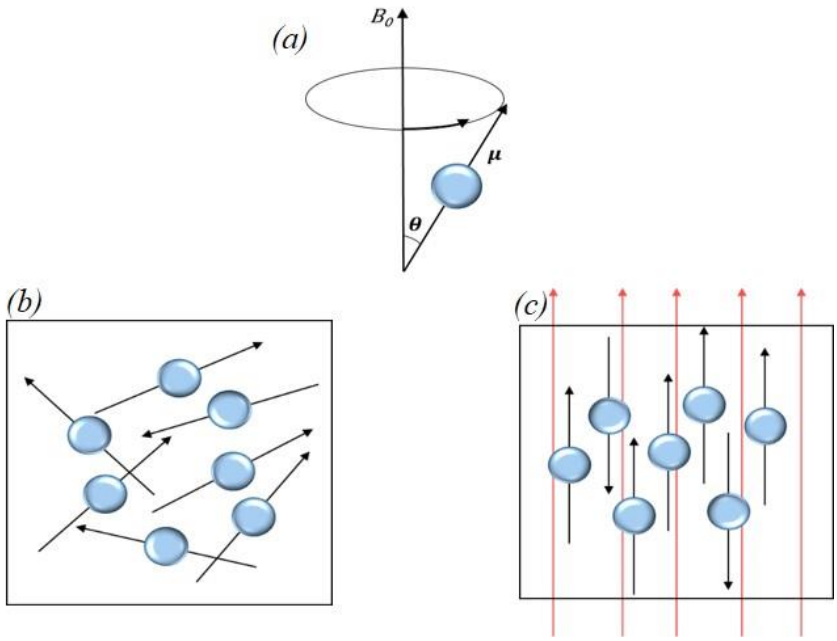

Figure 2.1: Precession. (a) Illustrates precession of a single proton. (b) Depiction of spin isochromats with zero net magnetization. (c) Alignment of spins along external magnetic field B_0 resulting in net magnetization vector M_z

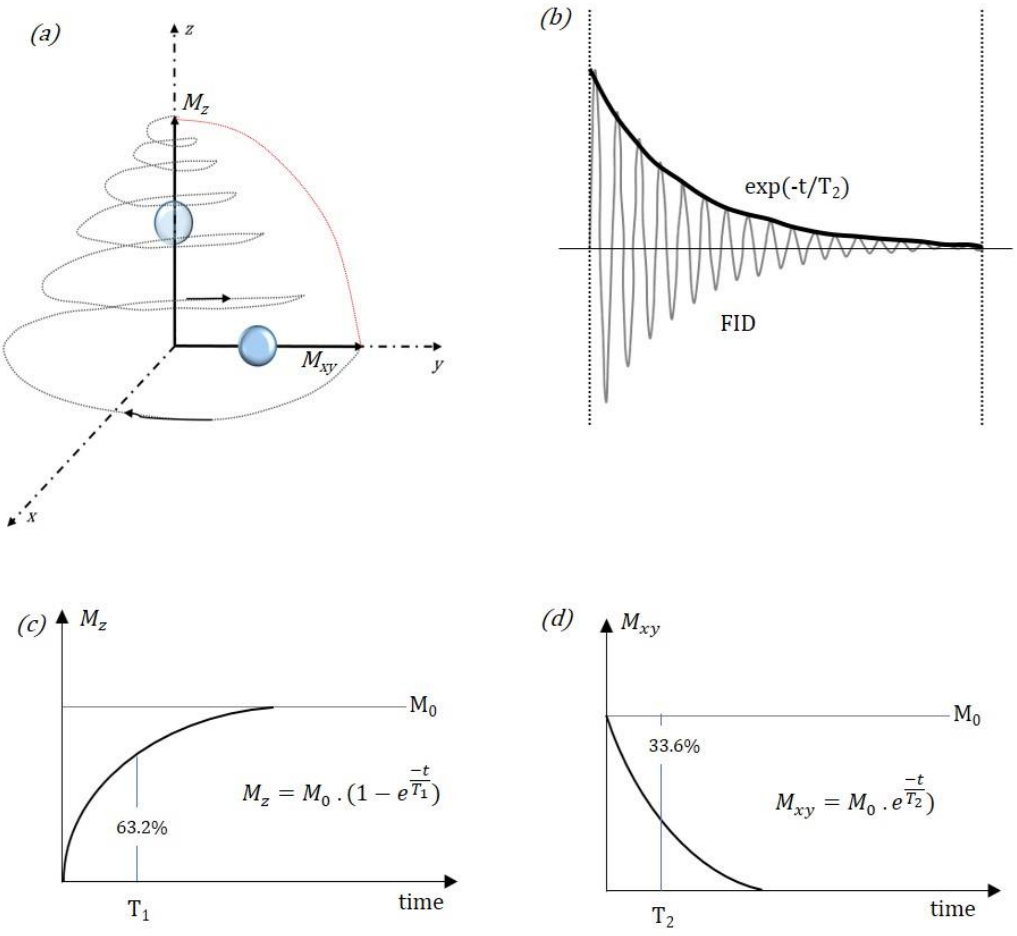

Figure 2.2: (a) The magnetization vector tends to realign with the B_0 field after being tipped to the xy plane using a 90° RF pulse. (b) Represents the Free Induction Decay (FID) i.e., the NMR signal. (c) Longitudinal relaxation T_1. (d) Transverse relaxation (T_2).

2.1.2 Basics of Magnetic Resonance Imaging

Expanding the data acquisition to higher dimensions, the time-varying signals detected from precessing magnetization could be analyzed by assigning a variation in frequency and phase to different locations in a 2D or 3D space. Gradient magnetic fields are used to encode MR signals by assigning a unique precession frequency and phase to each spin isochromat at a distinct spatial location along the gradient direction. This is

achieved by three orthogonal linear gradients through slice selection, frequency encoding and phase encoding. A frequency selective RF pulse with a central frequency ω_0 is applied simultaneously with a linear gradient to excite a slice of tissue such that the resonance condition is solely fulfilled at that position. The imaging plane at this stage is reduced to two dimensions. The decaying signals from the spin isochromats are further distinguished by applying the frequency and phase encoding gradient. The signals are acquired rapidly to form the *k*-space whose subsequent Fourier transform results in the MRI image.

Typically, the acquisition follows a geometric pattern called *k*-space trajectories whose path is maneuvered by the gradient waveforms. The phase evolution over time and position is given by

$$\phi(\boldsymbol{r}, t) = \gamma \int_0^t \boldsymbol{r}.\boldsymbol{G}(t')dt' \tag{2.6}$$

where $\boldsymbol{G}(t')$ is the gradient waveform, $\boldsymbol{r}$ is the distance from origin.

The extent of *k*-space covered with respect to the gradient waveforms is given by

$$k(t) = \frac{\gamma}{2\pi} \int_0^t \boldsymbol{G}(t')dt' \tag{2.7}$$

where $k(t)$ is the extent of *k*-space reached because of the area under the gradient waveforms.

Using equations 2.6 and 2.7 the signal equation in 2.4 and be equated with respect to the *k*-space data by replacing the phase term

$$S(t) = \int M_{\perp}(\boldsymbol{r})\, B_{\perp}(\boldsymbol{r}) e^{-i\, 2\pi\, \boldsymbol{k}(t).\boldsymbol{r}} d^3r \tag{2.8}$$

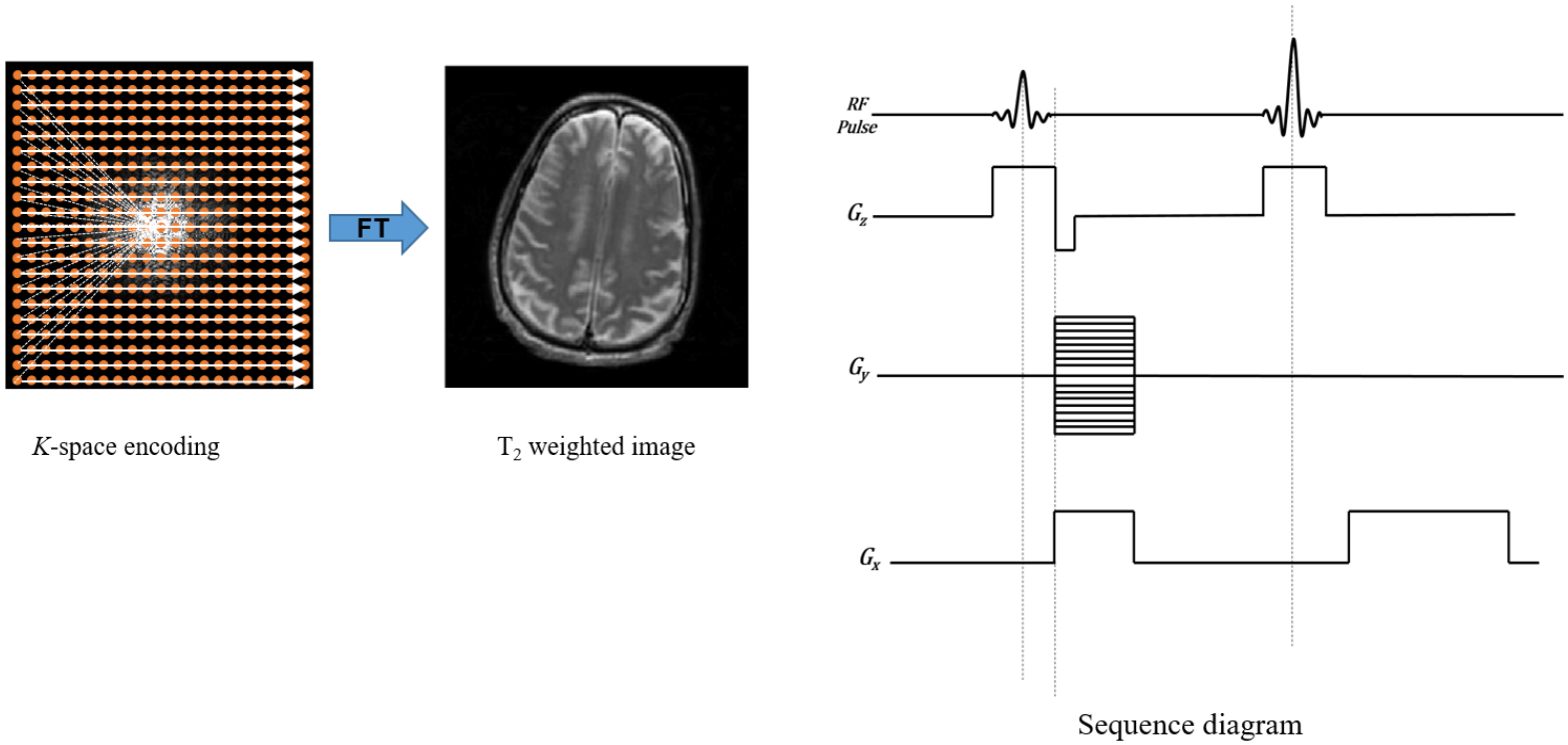

K-space encoding

T_2 weighted image

Sequence diagram

Figure 2.3: MRI *k*-space encoding. Representation of a typical frequency and phase encoding scheme in MRI also known as Cartesian sampling. The sequence diagram represents the timing of the RF and gradient pulses.

2.1.3 Clinical MRI

MRI offers high resolution and excellent soft tissue contrast and therefore has become a leading modality for diagnostic imaging at the clinic. *In vivo* MRI relies on the resonance signals from the water and fat hydrogen atoms and maps them according to their location within the patient. These signals are sensitive to physiological parameters, such as blood flow and are influenced by the immediate magnetic environment. Such parameters influence the T_1 and T_2 relaxation times in different tissue types; their normal and disease states. Image contrast could be generated for T_1-weighted, T_2-weigted and proton density weighted images by varying the pulse sequence parameters such as TE and TR. Numerous pulse sequence methods have been developed to characterize tissue types and diagnose diseases based on the weighting parameters. The conventionally used sequences and their scan times are tabulated in table 2.1.

For MRI exams of brain tumors, MR imaging alone is insufficient for the accurate detection of tumor location and their progression. Additionally, gadolinium-based contrast agents are injected to influence the relaxation times of the tumor regions for a more distinctive image representation of the affected regions. An example for the different weighting and contrast enhance (CE) MRI is shown in figure 2.4. The CE-MRI method however is qualitative and does not provide information regarding the prognosis of the disease.

Table 2.1: A Typical Clinical MR Exam Protocol

Sequence	***Scan time (min)***
SSFSE 3P	0:06

DWI Axial	1:30
Head TOF- MRA	5:04
FLAIR Axial	2:44
T2*w Axial	3:25
T1w Axial	3:21
T2w Axial	2:30
Neck TOF- MRA	9:01
Total	**27:40**

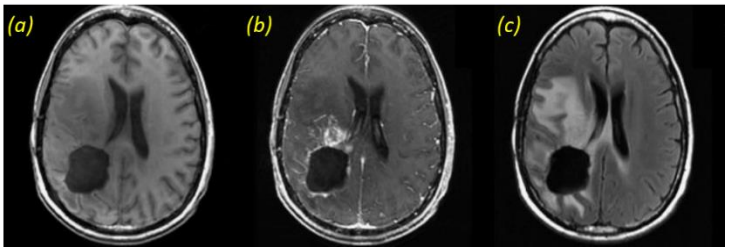

Figure 2.4: A typical MRI exam for brain tumors. (a)T_1-weighted pre/ (b) T_1-weighted post-contrast. (c)T_2-weighted images from a Grade IV glioma. Reproduced from [27].

2.1.4 Basics of Magnetic Resonance Spectroscopy

The magnetic resonance technique essential probes atoms and molecules based upon their interaction with an external magnetic field. The choice of probing the hydrogen protons (^{1}H) is due to their abundance in the human body as water and fat. Numerous other biochemicals have been identified to contain protons but are difficult to probe with conventional MRI due to their low signal to noise ratio (SNR) and are lost in translation during encoding. Over the decades, improvements in hardware and measurement techniques on the MRI scanners have permitted the detection of sparingly available

biomolecules. These biomolecules have been studied extensively in different healthy and disease states. In MRS studies, the signals from the biomolecules appear as distinct peaks based on their relative frequency to the Larmor frequency as described in the following section.

Chemical Shift

Protons in a molecule are surrounded by electrons and the other protons within the molecule. The electron cloud surrounding the proton modifies the Larmor frequency by

$$\omega = \gamma B_0(1 - \sigma) \tag{2.6}$$

where, σ is a shielding constant and is related to the chemical environment of the nucleus. As a result, the peaks from different metabolites appear at different frequency locations. This shift is also called chemical shift and is given by

$$\delta = \frac{\omega - \omega_{ref}}{\omega_{ref}} \times 10^6 \tag{2.7}$$

where δ is the chemical shift of nucleus under study with Larmor frequency of ω and ω_{ref} is resonant Larmor frequency of a reference nucleus. Chemical shifts are usually presented in parts per million (ppm). For ^{1}H-MRSI, tetramethylsilane (TMS) is used as a reference at 0 ppm. The non-exchangeable protons, which can be detected in *in vivo* MRSI, produce NMR signals in a relatively small frequency range (i.e., 1 – 5 ppm).

2.1.5 Conventional MRSI

MRSI, also referred to as Chemical shift imaging (CSI), coalesces the basic principles underlying MRI, and the spectral discrimination capabilities of nuclear magnetic resonance (NMR) spectroscopy in order to produce spatially localized distributions of

metabolic content. It measures the localized signals coming from small metabolites with concentrations tens of thousands of times smaller than that of water and lipid, which makes sensitivity and signal-to-noise ratio (SNR) critical for such acquisition.

Localization

Localization distinguishes the signal from within a volume of interest (VOI) with minimal contribution from outside of the defined volume. Point resolved spectral selection (PRESS) is one localization technique that has commonly been used to obtain MRS data [26]. Three slice-selective RF pulses, 90º-180º-180º, excite three intersecting orthogonal planes and pulse sequence diagram is illustrated in Figure 2.3. Other localization techniques for spectroscopy acquisition include stimulated echo acquisition mode (STEAM) and image-selected in vivo spectroscopy (ISIS).

Water and Lipid Suppression

Since the concentration of water is much higher than that of small metabolites, it is necessary to suppress the predominant water signals and thus makes it easy to observe weak signals from metabolites. Water suppression is generally achieved by eliminating the water signal prior to excitation and collection of the metabolite signals, such as chemical shift selective (CHESS) pulse. CHESS destroy the water signal by means of a spectral selective 90º pulse and followed by a dephasing pulse [27]. Multiple repetitions of CHESS pulses that are frequently used in practice can produce a better water suppression [28]. BASING (band selective inversion with gradient dephasing) pulse is a more improved technique using the frequency selective RF 180º pulse for both water and lipid suppression

[29]. Another way for water suppression is to only excite the frequency of interest, such as spectral-spatial pulses [30] with the metabolites of interest only in the pass band and water/lipid in the stop band.

To eliminate unwanted lipid signals from outside the VOI and preserve the metabolic information, outer volume saturation (OVS), saturation bands that surround the excitation volume and especially cover these regions that contain high lipid, is commonly used [31]. Compared with traditional OVS, very selective suppression (VSS) that was used in this project offers larger excitation bandwidth and narrow transition bands. These benefit for better lipid suppression, less chemical shift artifact and sharpen the edges of the PRESS selected box [32].

2.1.6 Important Metabolites

An example of ^{1}H MRSI of in vivo human brain from a 3 T MR scanner is illustrated in Figure 2.4. The major metabolites that are observed with an echo time of 144 ms are choline (Cho), creatine (Cr), N-acetyl aspartate (NAA), and lactate (Lac).

N-acetylaspartate

The methyl (CH_3) group of N-acetylaspartate (NAA) gives rise to a prominent singlet at 2.01 ppm in the proton spectrum observed in MRS/MRSI. NAA is found only in the brain and spinal cord and possibly function as an osmolyte. It is synthesized and stored in the neurons but hydrolyzed in oligodendrocytes [33-35]. Since NAA is a neuronal marker, any pathology with a loss of neurons or function results in reduced NAA levels, such as gliomas.

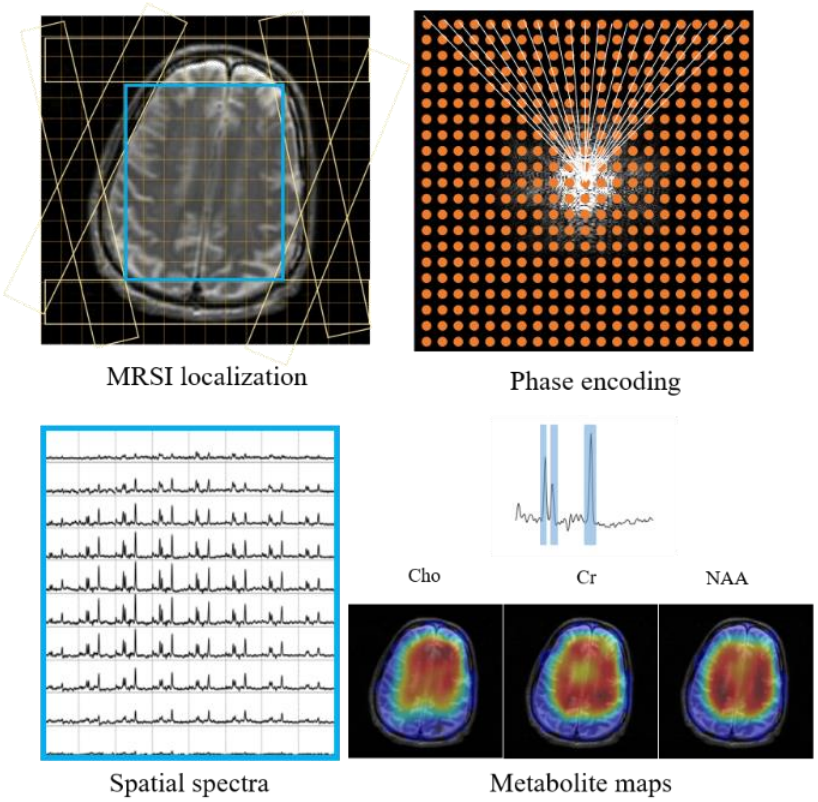

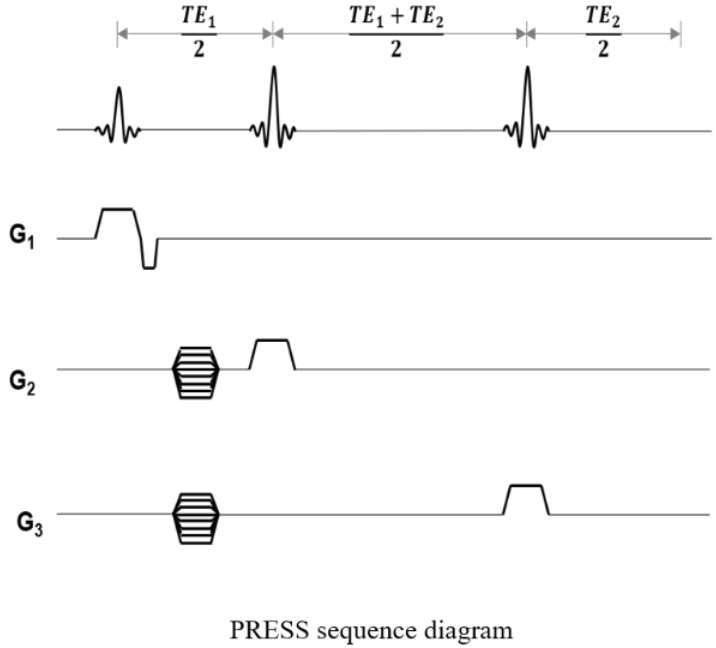

Figure 2.5: Conventional MRSI data acquisition

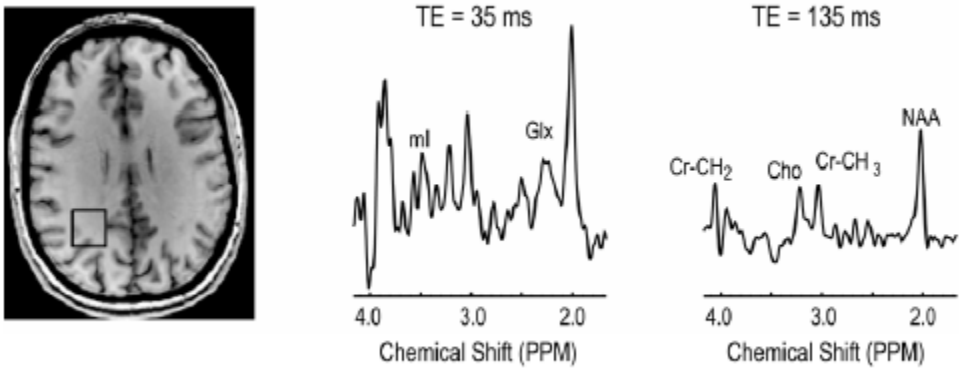

Figure 2.6: Normal brain spectra acquired with PRESS sequence. Reproduced from [27].

Creatine

The methyl and methylene protons of Cr and phosphorylated creatine (PCr) give rise to singlet resonances at 3.03 ppm and 3.93 ppm, respectively and are indistinguishable. Cr and PCr are involved in adenosine triphosphate (ATP) metabolism and thus the level of the total creatine is a marker for cellular bioenergetics. Creatine is mostly synthesized in the liver and kidneys. metabolism of tissues, along with adenosine triphosphate (ATP). TCr is frequently employed as an internal concentration reference as levels remain relatively constant in various diseases, with no changes being observed even with age. Chronic phases of various tumors and stoke have displayed a decrease in Cr levels. Increased metabolic activity in certain high-grade gliomas may reduce the total creatine concentration [36].

Choline

The methyl protons of choline-containing compounds give rise to a prominent singlet at 3.2 ppm in the ^{1}H MRS spectrum. It is a precursor of various metabolites such as phosphorylcholine (PC), and glycerophosphorylcholine (GPC), phosphatidylcholine (PtdCho), acetylcholine, and betaine. The peak at 3.2 ppm has a significant contribution from betaine in tissues present outside the central nervous system (CNS). Choline-containing compounds are reflective of membrane turnover, as they are involved in the phospholipid synthesis and degradation pathways. On the other hand, reduced choline signal has been detected in stroke and liver disease [33]. Multiple contributions to the

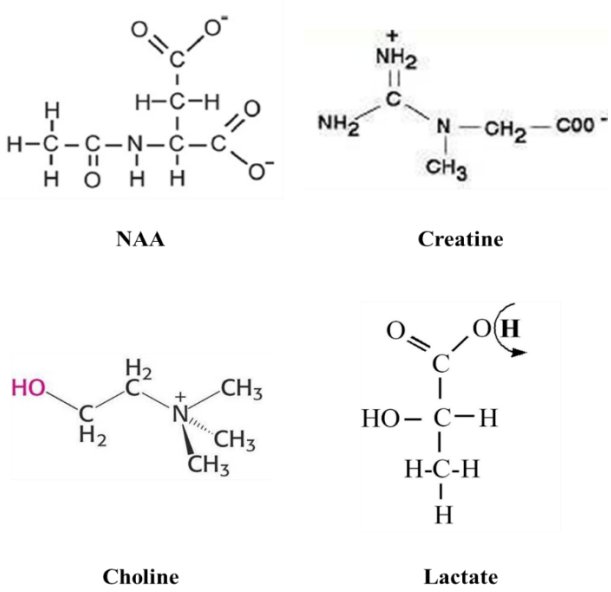

Figure 2.7: Chemical structure of major metabolites observed in the ^{1}H MRS/MRSI spectrum.

observed total choline signal tend to complicate an accurate interpretation of changes in tCho. In malignant tumors and (primary and secondary/metastatic) neoplasms, increased cellularity causes an increase in the total choline concentration [34].

Lactate

Lactate is the end product of anaerobic glucose metabolism and indicates hypoxia or poor perfusion within the lesion. The three-equivalent methyl (CH_3) protons of the lactate molecule produce a doublet at 1.31 ppm, while the single methine (CH) group gives rise to a quartet at 4.10 ppm. Typically, lactate is not observed in normal brain tissue due to its low concentration, but increased lactate has been seen in high grade gliomas. Lactate is also an important marker in tumor prognosis and monitoring efficacy of treatment. Large resonances from the lipid molecules tend to overlap with the lactate doublet, particularly in regions with poor localization. Under such circumstances, specialized spectral editing techniques need to be employed for improved detection of the lactate peak [33].

2.1.7 Challenges in clinical MRSI

Low signal to noise ratio (SNR)

The metabolites of interest to be imaged in MRSI are extremely low in concentration compared to water and fat molecules that are imaged in standard MRI. The three major metabolites in human brain are Choline (Cho), Creatine (Cre) and N-acetyl-aspartate (NAA). They are about tens of thousand times smaller in concentration compared to water. This low SNR often causes inaccuracies in quantification of metabolites.

Long scan time

In conventional MRSI, the data needs to be encoded in multiple dimensions, making it an extremely slow process. Additionally, to obtain considerable SNR sometimes several averages are collected The SNR is proportional to the voxel size and the square

root of the imaging time. This significantly prolongs the data acquisition limiting the practical utility.

Poor Spatial Resolution

To reduce scan time, the MRSI methods are restricted to limited number of spatial encodes and obtain reconstruction with large voxel size to get enough signal. This results in severe voxel interference restricting proper spatial resolution of spectroscopic information.

Water and lipid contamination

MRSI experiment also suffer from water and lipid contamination. The metabolites of interest are of low concentration and are resolved between the high peaks of water and fat. Poor linewidth estimation further leads to overlapping fat resonances and can have detrimental effects on the estimation of metabolic information.

2.1.8 MRSI Post-Processing

The acquired MRSI data are processed and analyzed to determine absolute/relative metabolite concentrations and to present the metabolic information in an easily interpretable format to the radiologist. Conventionally the following steps are performed for accurate data representation and mapping.

Apodization

Filter functions are used to reduce the truncation artifacts and thereby improve SNR. A spatial Hamming and spectral Gaussian filter are typically used to smoothen the spectra and reduce noise.

Phase Correction

Before quantification, the real and imaginary components of the complex spectrum need to be accurately determined from the pure absorption and dispersion modes. A constant or zero-order phase correction φ_0 is applied when all signal components experience the same phase shift, e.g. if the transmitted and received RF signals have a fixed phase difference. A linear or first-order phase correction $\varphi 1$ is required when various signal components experience different phase shifts. Both φ_0 and φ_1 are varied independently to get the best separation between the absorption and dispersion modes.

Channel Combination

The spectra processed for all the channels are combined based on the channel weighting. The weighting parameter depends on the location of the coil and its sensitivity. These weighting parameters are registered by the scanner during the prescan.

Removal of Residual Water

A significant residual water peak remains in the spectrum in regions where the localization and OVS suppression was poor, e.g. in the peripheral regions of the brain where the magnetic field may not be homogeneous. This residual water peak must be eliminated before metabolite fitting and quantification. Techniques like the singular value decomposition (SVD) and the Hankel-Lanczos variant (HLSVD) allow reliable automatic suppression of any residual water, with little to no user input required.

Spectral Fitting & Quantification

The final step in the processing and analysis of MRSI data involves fitting the various peaks of interest in the spectrum to known line shape functions such as the

Gaussian (more common for solids), Lorentzian, or a combination of two or more functions. Spectral components can be estimated using various quantification algorithms such as AMARES (Advanced Method for Accurate, Robust, and Efficient Spectral fitting), HLSVD, HTLS, and QUEST (QUantitation based on QUantum ESTimation). Curve fitting techniques can be applied in either the frequency or time domain. After post-processing, results are displayed either as an individual spectrum (in the case of SVS) or as individual metabolite maps overlaid/co-registered on the anatomical reference image in MRSI.

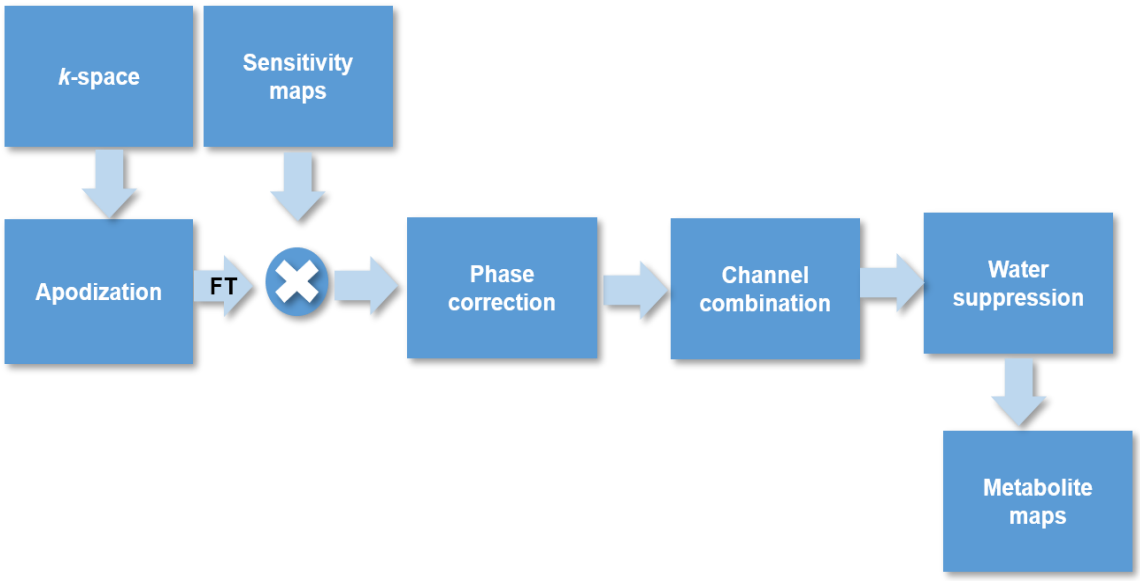

Figure 2.8: Conventional MRSI post-processing workflow.

2.2 Compressed Sensing and MRSI

Compressed Sensing is a novel approach that exploits the inherent sparsity of medical images in an appropriate transform domain to effectively undersampling *k*-space. This in turn reduces the number of samples that are required for reconstruction in MRI and MRSI [17-20, 40]. The CS theory successfully predicts that signals can be accurately recovered even when sampling well below the established Nyquist rate, if the signals under consideration are sparse in some transform domain (not just in the time or frequency domains) [41]. Data tend to be sparse in multiple dimensions of space and frequency in the wavelet transform domain, thus, making this technique particularly suitable for MRSI. Wavelets have been employed to achieve a sparse representation of MRSI data in both the spatial and spectral domains, facilitating the application of CS acquisitions in MRSI.

The CS based reconstruction of undersampled data has to fulfill three main requirements, namely, data sparsity, the implementation of pseudo-random undersampling, and a non-linear reconstruction algorithm for accurate recovery of the signals under consideration.

2.2.1 Transform Sparsity

A ‘sparse’ vector contains all information in a few non-zero coefficients, with all other coefficients being zero. ‘Strong’ sparsity is encountered when very few coefficients contain all the information in the signal. Most practical applications tend to exhibit ‘weak’ sparsity as a transition band exists been the few high-valued coefficients and the numerous

non-zero coefficients. Most of the signal energy is restricted to these few non-zero coefficients, while the remaining measurements are essentially zero or close to zero [42].

A sparsifying transform operator can be applied to map the image vector under consideration to a sparse vector. For e.g. the Fourier transform of a direct current signal is a delta function in the frequency domain, which contains all the signal information. Thus, a sparse representation of a signal can be obtained by applying the appropriate transform operator. Similarly, most MR images tend to be sparse in some transform domain. For e.g. angiograms tend to be sparse in the finite difference domain as most of the important information is contained in the boundaries [17, 42].

Many sparsifying transforms have been developed over the years to facilitate sparse representations of different kinds of images [43]. Two particular transforms of interest are the wavelet transform and the discrete cosine transform (DCT), which provide a sparse representation of several real-life images [44]. These transforms have been extensively employed in the field of image compression. A multi-scale representation of the image can be obtained using the wavelet transform. Fine-scale wavelet coefficients correspond to the high-resolution image components while coarse-scale wavelet coefficients represent the low-resolution components [17]. It is important to determine the minimum number of sparse coefficients that are required to obtain an accurate reconstruction of the MRSI data [42].

2.2.2 Pseudo-Random Undersampling

The second essential criterion in CS requires the random undersampling of the MRSI *k*-space in order to produce incoherent artifacts that resemble noise [17, 42].

Uniform *k*-space undersampling violates the Nyquist criterion producing coherent artifacts such as aliasing. While the random selection of *k*-space samples also violates the Nyquist limit, the resulting artifacts are sufficiently incoherent that they can be removed by denoising techniques. In the case of MRI/MRSI, the *k*-space is pseudo-randomly undersampled i.e. a certain fraction of the samples is placed at the center of *k*-space, while the remaining samples are randomly distributed in the peripheral *k*-space region. This is necessary as majority of the information and SNR is confined to the low frequency components, which are located at the *k*-space center. A truly random undersampling of the *k*-space also necessitates rapid gradient switching, which is constrained by the hardware and artifacts like eddy currents [18-20].

The number of required samples depends on the level of data sparsity and is usually five to eight times the number of sparse coefficients in the transformed data. Thus, identifying the number of sparse coefficients is critical to determining the acceleration limit of the CS reconstruction algorithm. The optimal sampling masks for MRSI continues to be an area of research. A retrospective evaluation of different sampling masks generation methods performed by Shankar et al. [20]. The variable density and *a priori* methods were found to be most optimal compared to the other methods.

2.2.3 Iterative Reconstruction

The reconstruction of the acquired CS-MRSI data can be formulated as a constrained optimization problem, as illustrated in equation 2.8 below:

$$\begin{aligned} &minimize \quad \|\psi m\|_1 \\ &such\ that \quad \|F_u m - y\|_2 < \varepsilon \end{aligned} \tag{2.8}$$

Where, m is the desired MRSI data to be reconstructed, y is the acquired *k*-space data from the scanner, F_u is the undersampled Fourier operator, ψ is the transform operator that provides a sparse representation of the data, and the parameter ε controls the tolerance error of the reconstruction. $\| \|_1$ and $\| \|_2$ are essentially operators representing the l_1 norm and l_2 norm, respectively. Minimizing $\|\psi m\|_1$ enforces sparsity, while the data consistency constraint is enforced via $\|F_u m - y\|_2 < \varepsilon$. A total variation (TV) penalty is often included in the objective function in addition to a specific sparsifying transform operator. In such cases, the objective function ensures that the MRSI data has a sparse representation from both the specific transform as well as from finite differences. Equation 2.2 can then be reformulated to include the TV operator as follows [70]:

$$\begin{aligned} &minimize \quad \|\psi m\|_1 + \alpha TV(m) \\ &such\ that \quad \|F_u m - y\|_2 < \varepsilon \end{aligned} \tag{2.9}$$

Wherein the operator α trades the sparsity from the finite differences and the ψ operator. Employing the Lagrange method, Equation 2.3 can recast as an unconstrained optimization problem that involves minimizing the following equation [70, 74]:

$$argmin \ \|F_u m - y\|_2^2 + \lambda_1 \|\psi m\|_1 + \lambda_2 TV(m) \tag{2.10}$$

Where, λ_1 and λ_2 are regularization parameters that need to balance the data consistency and sparsity terms. An iterative non-linear reconstruction algorithm such as the steepest descent method or the non-linear conjugate gradient technique can be employed to solve for the desired MRSI data m in Equation. For e.g. in the conjugate gradient algorithm, Equation is differentiated to determine the direction of the gradient each time. A line-search parameter is incorporated to evaluate the step-length to be advanced in the gradient direction. Convergence in the iterations is obtained when a) there

is negligible difference in the tolerance parameter values between successive iterations, and b) the tolerance parameter value is lower than the selected ε value. The total number of iterations required to obtain convergence in the cost function is dependent on problem at hand and the type of data being evaluated.

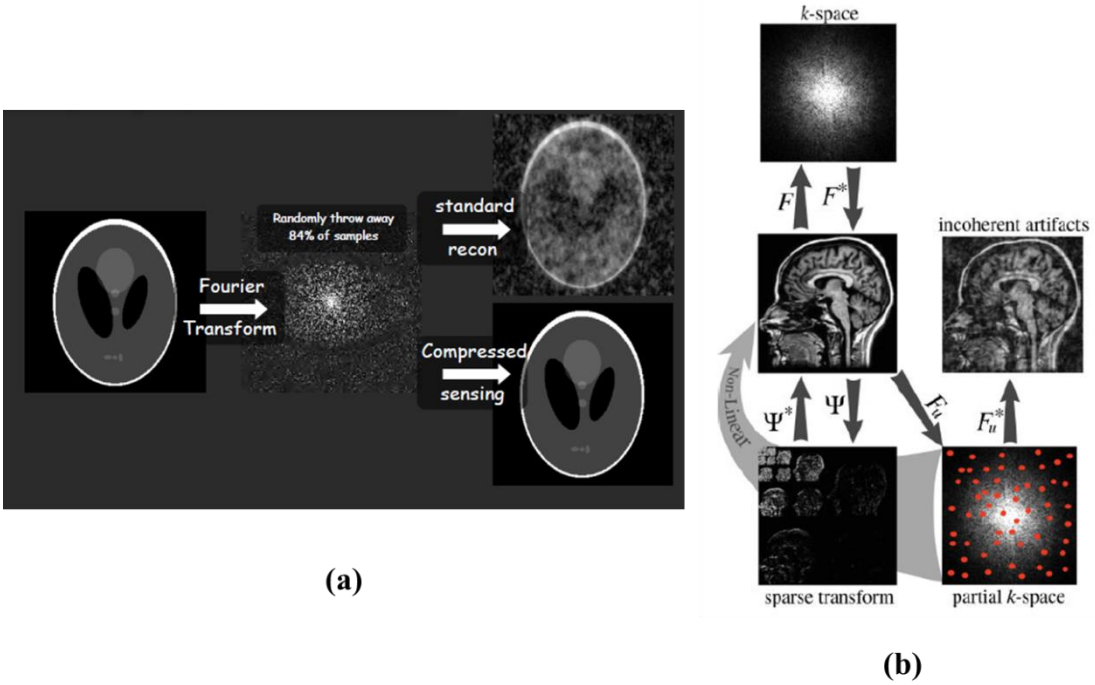

Figure 2.9: (a) An illustration of pseudo-random undersampling in CS. (b) Various domains and operators in CS. Reproduced from reference [17].

The first application of CS to MR imaging was by Lustig *et al* [17]. The application of CS to ^{1}H MRSI was investigated by Geethanath *et al* for various acceleration factors, retrospectively [18,19]. Sampling masks were generated for various acceleration factors, namely, two, three, four, five, and ten using variable density random undersampling. A two-dimensional probability density function was used to select the random samples, ensuring a denser sampling at the center of *k*-space and sparser sampling of points towards the periphery [18]. The reconstructions at various acceleration factors preserved the fidelity

of the metabolite spectrum when compared with the fully sampled conventional MRSI datasets. The algorithm broke down at an acceleration factor of ten, wherein the metabolite peaks began to show increased signal intensities when compared to the conventional MRSI datasets. The reconstruction, thus, faithfully preserved the prognostic and diagnostic value of the metabolite maps up to an acceleration factor of five; this retrospective study was an important first step that demonstrated the feasibility of the approach (Figure 2.6) [18].

2.2.4 Application of CS to MRSI

CS has been employed to accelerate multidimensional spectroscopic imaging in recent clinical studies [45-47]. A 4D echo planar imaging sequence based on J-resolved spectroscopy was implemented using CS to achieve a high acceleration *in vivo*, demonstrating the utility of multidimensional MRSI. The CS technique has also been applied to ^{13}C 3D MRSI, in the design and testing of a CS based new EPSI sequence [48, 49]. Hyperpolarized ^{13}C data are well suited for CS applications due to the fundamentally sparse spectrum and high SNR resulting from hyperpolarization. The T_1 decay of the hyperpolarized signal restricts the amount of time available for signal acquisition in the time-window when SNR is high, thus, necessitating the use of accelerated imaging techniques for optimal spatial coverage and speed. The sequence proposed by Hu *et al* achieves an acceleration factor of up to 7.53, and minimal artifacts in the reconstruction for 3D MRSI. A time-resolved 3D MRSI technique has been developed by Larson *et al* [50] for monitoring the dynamics of pyruvate conversion to alanine and lactate in a mouse model. This method effectively utilizes the magnetization using multiband excitation pulses in combination with CS for increased acceleration [50].

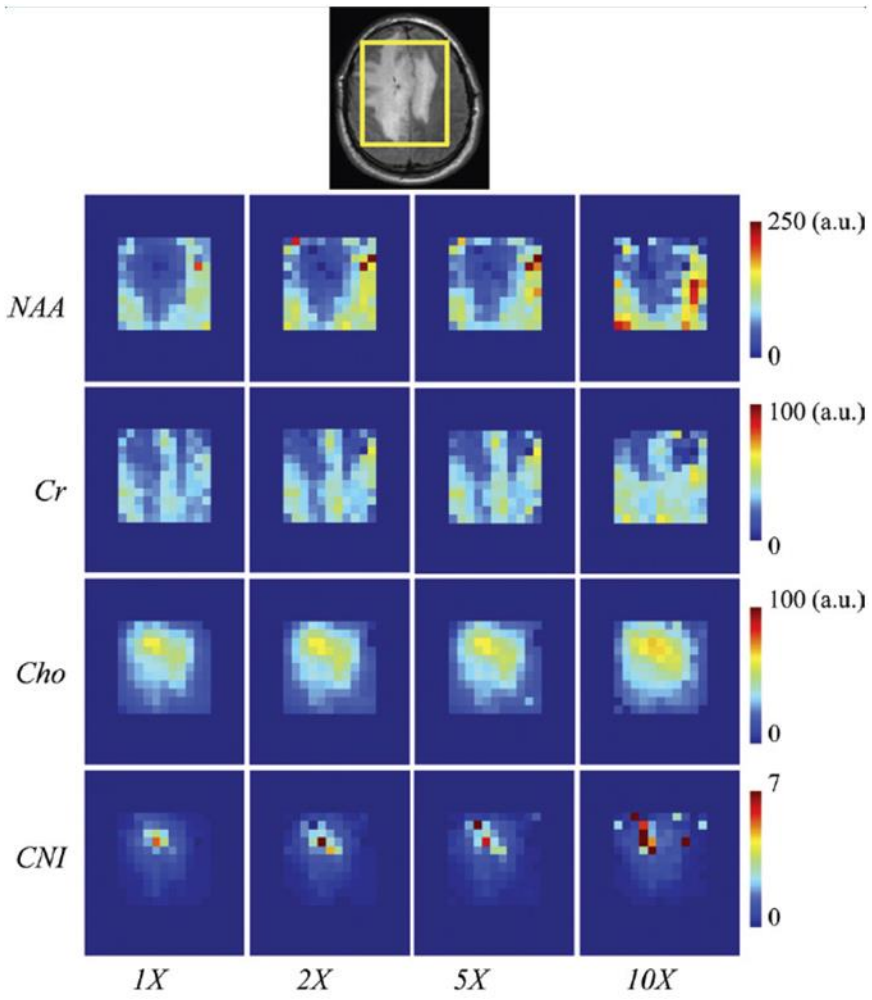

Figure 2.10: The retrospective application of CS-MRSI demonstrated in a brain tumor patient. Representative metabolite maps of NAA, creatine (Cr), choline (Cho), and choline to NAA index (CNI) for various acceleration factors. Reproduced from reference [18] .

The CS technique has also been applied to ^{31}P MRSI of the human brain by Askin *et al* [51]. The long scan times associated with ^{31}P MRSI restrict its widespread use in the clinic. Furthermore, ^{31}P MRSI requires larger voxels and increased signal averaging to obtain adequate SNR as the signal from ^{31}P is approximately 15 times less MR sensitive than that from protons. In this study, a higher SNR was observed in the CS reconstructed data, while the peak height ratios of the original and CS datasets were comparable [51].

Recent promising preclinical applications of CS MRSI *in vivo* include ^{19}F 3D spectroscopy in mice [52] wherein the non-existent background signal in ^{19}F MRSI makes it particularly suited to satisfy the sparsity constraint that is integral to CS. Exogenously administered ^{19}F MRSI has several markers with unique spectral signals that can be well detected in the presence of a negligible background signal. Kampf *et al* demonstrated the retrospective application of CS based ^{19}F MRSI both *in vitro* and *in vivo*, with the CS reconstructions preserving the fidelity of the data up to an acceleration factor of 8 [52]. The first application of high resolution ^{23}Na spectroscopic imaging in mouse hearts was recently demonstrated by Maguire *et al* [85]. The ^{23}Na MRSI data from *in vivo* mouse hearts were prospectively undersampled by 3X and reconstructed using the CS algorithm previously described in [18], to yield undersampled reconstructions that preserved the fidelity of the data.

CHAPTER 3

UNDERSAMPLING STRATEGIES FOR COMPRESSED SENSING MRSI

3.1 Introduction

Clinical ^{1}H MRSI is limited by its inherently long acquisition time. Retrospective studies by Geethanath *et al* [18] and Shankar *et al* [19, 20] have demonstrated the feasibility of CS based acceleration at the clinic. In this study, a prospective implementation of CS-MRSI is performed on a clinical scanner for fast *in vivo* brain MRSI.

3.2 Materials and Methods

3.2.1 Undersampling Pattern

Two spatial 2D *k*-space undersampling patterns were generated on MATLAB (The MathWorks Inc., MA), for 5X and 3X acceleration, and were implemented on a conventional PRESS sequence. The phase encodes for the zeros in the patterns were knocked out. The variable density pattern was generated based on the pseudorandom sampling strategy described by Lustig *et al.* [17]. This pattern remained unmodified throughout the study. The *a priori* undersampling pattern was derived from the *k*-space of

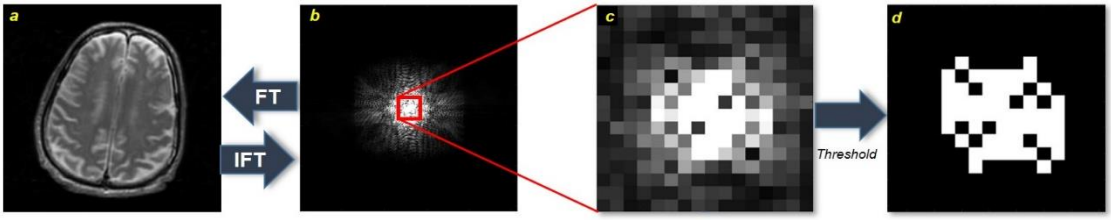

Figure 3.1: *A priori* mask generation. a) Raw *k*-space for T_2 weighted axial scout. b) 16×16 cropped *k*-space. c) T_2 weighted reference scout. d) *a priori* undersampling pattern for 5× acceleration

the axial T_2 weighted anatomical reference scout acquired during the study. The scout *k*-space was cropped to match the corresponding MRSI spatial grid size and intensity thresholding was applied to select the highest energy locations of *k*-space.

3.2.2 MRSI Experiments

All phantom and *in vivo* experiments were performed on a GE Discovery 3 T clinical scanner (General Electric Healthcare, Waukesha, WI) with a standard 12 channel head coil. For the phantom experiments, a spherical braino phantom (GE, Waukesha, WI) containing 12.5 mM N-acetyl Aspartate (NAA), 10.0 mM creatine, 3.0 mM choline, and 5 mM lactate was used. T_2 weighted imaging sequence and PRESS sequence were employed for the experiment.

3.2.3 MRSI Data Acquisition

The study was approved by the local institutional review board. Informed consent was obtained from 16 patients participating in the study. A single slice axial T_2 weighted scout was acquired with TE/TR = 100/3000 ms, matrix size of 128×128, and FOV of 22 cm isotropic. The manufacturer-provided PRESS sequence was used to obtain fully sampled (1×) MRSI data with the following parameters: TE/TR = 144/1200 ms, matrix size of 16×16×2048, slice thickness 10 mm, and FOV of 22 cm isotropic. Manual shimming was performed to obtain reliable linewidth. The acquisition time was 5 min 12 sec. A modified PRESS sequence was used subsequently to acquire a variable density and an *a priori* 5X undersampled data sets. Additionally, 3X undersampled data was acquired

for 5 subjects. The acquisition parameters, the shim, and gain parameters were kept consistent with the 1× scan. The scan time for each undersampled acquisition was 1 min 4 sec 5X and 2 min 1 sec for 3X acceleration.

3.2.4 Post Processing

A custom algorithm was implemented on MATLAB to reconstruct for the fully sampled and undersampled MRSI data sets. For each individual channel data, the residual water and fat were removed by Hankel-Lanczos Singular Value Decomposition (HLSVD) followed by a 3 Hz Gaussian and Hamming apodization along the spectral and spatial dimension. For the fully sampled data set, Fourier transformation, phase correction, and channel combination were performed to obtain 1× reference spectra and saved for quantitative comparison.

The filtered undersampled data sets were iteratively reconstructed based on the conjugate gradient algorithm. The CS-MRSI reconstruction was formulated as a convex optimization problem, which involved minimizing the following cost function:

$$*€(m) = \|F_u m - y\|_2 + \lambda_{L1}\|Wm\|_1 + \lambda_{TV} TV(m) \quad (3.1)$$

where, y is the measured *k*-space data, m is the desired MRSI data, F_u, W, and TV are the Fourier transform, wavelet transform, and total variation operators, respectively. $\|\,.\,\|_1$and $\|\,.\,\|_2$ are the l_1 and l_2 norm operators, respectively, λ_{L1} and λ_{TV} are the corresponding regularization parameter for the l_1 norm and TV operator, respectively. The $k_x - t$ matrix was encoded along each of the two dimensions using the Daubechies wavelet transform at

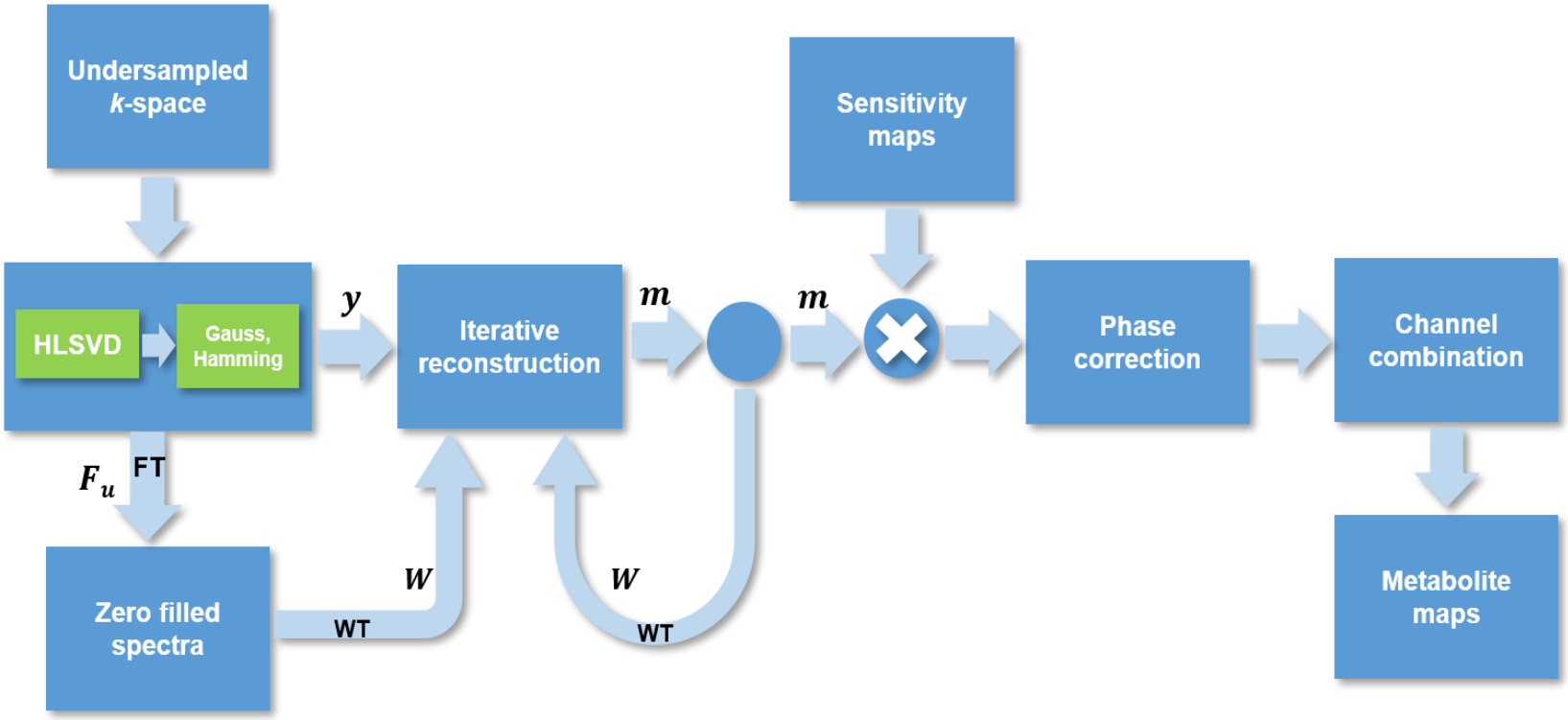

Figure 3.2 CS-MRSI Reconstruction workflow

all points in k_y. The regularization terms λ_{L1} and λ_{TV} were experimentally determined to be 0.001 and 0.005, respectively.

The CS reconstructed MRSI data for each channel was phase-corrected and combined. Metabolite maps were generated using the area integration method for N-acetyl aspartate (NAA), creatine, and choline. The resulting spectra for both variable density and *a priori* undersampling approach were quantitatively compared with the 1X spectra. The postprocessing pipeline is explained in detail in chapter 4.

3.2.5 Statistical Analysis

The fidelity of CS reconstruction was evaluated by a voxel-wise two-tailed *t*-test comparing individual metabolite maps generated from 1X, 5X and 3X reconstructed spectra. A region of interest (ROI) was used to delineate the spectra and noise regions. A *p*-value of < 0.05 was considered statistically significant and indicative of an incorrect reconstruction. The normalized root mean squared error was evaluated for the undersampled spectra(s) concerning the fully sampled spectra.

3.3 RESULTS

A prospective evaluation of CS-MRSI was conducted successfully for adult *in vivo* brain MRSI to achieve a five-fold scan time acceleration using two different undersampling schemes. The CS-MRSI reconstruction workflow is shown in figure 3.2. A total of 51/256 phase encodes were sampled for each 5X undersampling and 85/256 phase encodes for 3X undersampling acquisition. The 5X pseudorandom variable density undersampling pattern is as depicted in figure 3.3(d) and remained unchanged through all the subject scans.

Likewise, the 3X variable density undersampling pattern is shown in figure 3.7 (d) which remained unchanged for the 5 patients. The *a priori* undersampling pattern was obtained based on the T_2 weighted scout *k*-space and was different for each subject.

Figure 3.3 compares the prospective and retrospective 5X undersampled CS-MRSI reconstructions with the fully sampled reconstruction for the *in vivo* brain data acquired for a 66-year-old male patient screened for lung cancer without brain metastasis. Figure 3.3(a) represent the fully sampled reconstruction for conventional PRESS acquisition. Figure 3.3(e) and 3.3(f) represent the prospective CS-MRSI reconstruction for the *a priori* and variable density undersampled acquisitions respectively. Figure 3.3(b) displays the anatomical scout; blue box represents the PRESS volume of interest (VOI). The difference between fully sampled and prospective *a priori,* variable density CS-MRSI reconstruction is as shown in figure 3.3(i) and 3.3(j) respectively. Similarly, the panel with Figure 3.3(g, h, k, l) depicts the retrospective reconstructions and differences for *a priori* and variable density undersampling. The scale for all spectra data plots is the min to max of fully sampled spectra. The scale for all the difference plots is –max to +max of fully sampled spectra. Figure 3.3(c) represents a single voxel comparison of all reconstructed spectra. The line width and amplitude peaks for each metabolite of the CS reconstructed spectra data are comparable to the fully sampled spectra. The differences observed were lowest for the *a priori* retrospective and highest for variable density prospective reconstructions. Voxel-wise comparison shows that the metabolite ratios are consistent. Figure 3.4 depicts the metabolite maps generated from the reconstructed data for the spectra data shown in figure 3.3. The metabolite maps are obtained as the area under the NAA, Cr and Cho peaks. Same linewidths used for the fully sampled metabolite peaks and the CS-MRSI data. A

low-resolution 16×16 area integrated array is obtained for each of the metabolites; NAA, Creatine, and Choline and resized to a higher resolution 256×256 array and overlaid on the T_2 weighted anatomical scout.

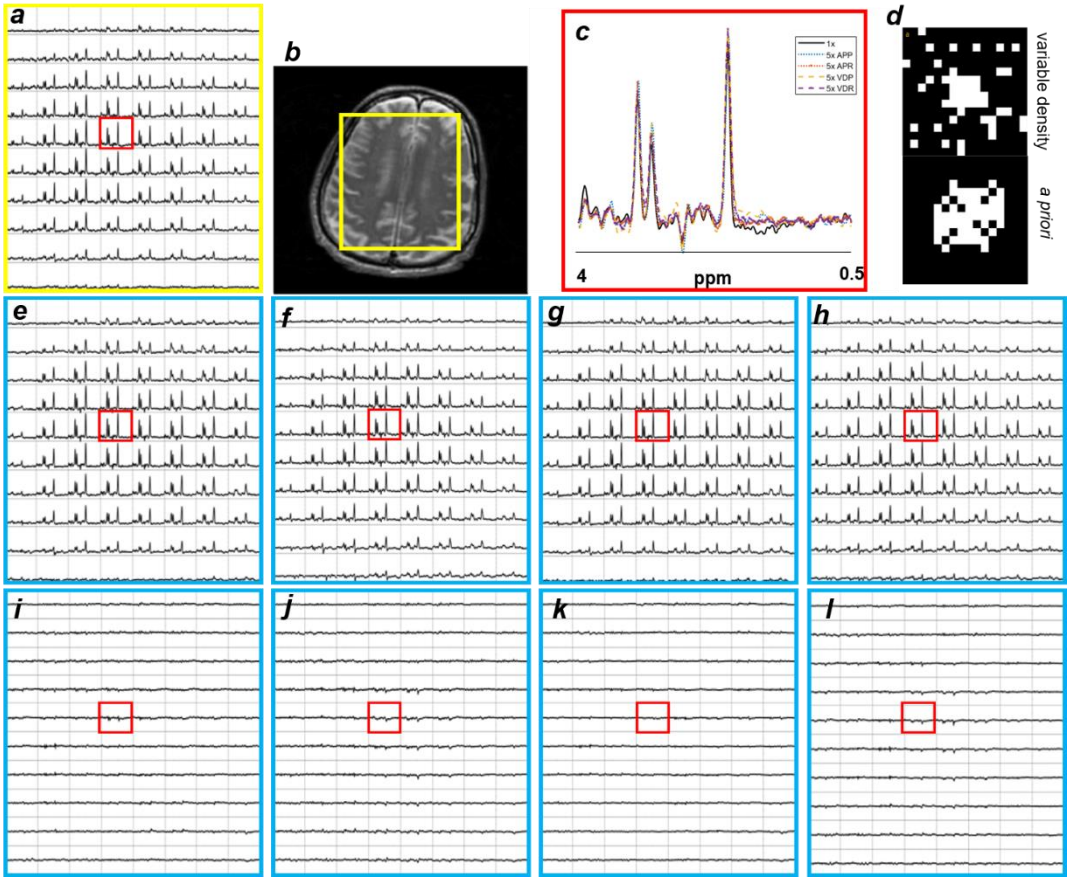

Figure 3.3: Displays the spectra of the *in vivo* brain comparing undersampled CS reconstruction (5X) to fully sampled Fourier reconstruction of a 66-year-old male patient. (a) MRSI reconstruction for the fully sampled *k*-space. (b) T_2 weighted anatomical scout with TE/TR = 104/3000 ms, FOV 22×22 cm, matrix 128×128). (c) Select voxel for comparison in red box (magnified). (d) variable density and *a priori* undersampling patterns. (e, i) *a priori* prospective CS-MRSI reconstruction and difference spectra. (f, j) variable density prospective CS-MRSI reconstruction and difference spectra. (g, k) *a priori* retrospective CS-MRSI reconstruction and difference spectra. (h, l) variable density retrospective CS-MRSI reconstruction and difference spectra.

Figure 3.5 compares the prospective and retrospective 5X undersampled CS-MRSI reconstructions with the fully sampled reconstruction for the *in vivo* brain data acquired for

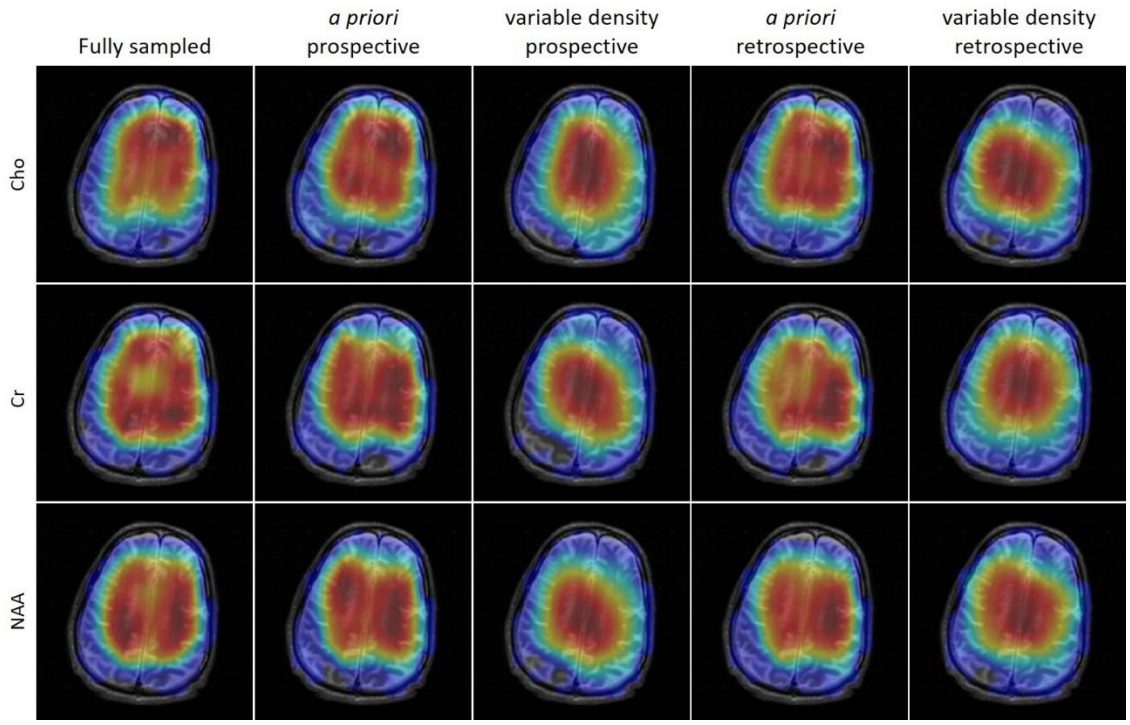

Figure 3.4: *In vivo* brain metabolite maps for the fully sampled and 5X CS reconstructed spectra displayed in Figure 3.3. Choline (Cho), Creatine (Cr) and N-acetyl aspartate (NAA) maps are generated as the area under the respective peak linewidths.

a 52-year-old male patient screened for lung cancer with brain metastasis. Figure 3.5(a) represent the fully sampled reconstruction. Figure 3.5(e) and 3.5(f) represent the prospective CS-MRSI reconstruction for the *a priori* and variable density undersampled acquisitions respectively. The difference between fully sampled and prospective *a priori*, variable density CS-MRSI reconstruction is as shown in figure 3.5(i) and 3.5(j) respectively. Similarly, the panel with Figure 3.5(g, h, k, l) depicts the retrospective reconstructions and differences for *a priori* and variable density undersampling. Figure 3.5(c) represents a single voxel comparison of all reconstructed spectra. The line width and amplitude peaks for each metabolite of the CS reconstructed spectra data are comparable to the fully sampled spectra. The differences observed were lowest for the *a priori* retrospective and highest for variable density prospective reconstructions. Voxel-wise

comparison shows that the metabolite ratios are consistent. Figure 3.6 depicts the metabolite maps generated from the reconstructed data for the spectra data shown in figure 3.5. The metabolite maps are obtained as the area under the NAA, Cr and Cho peaks.

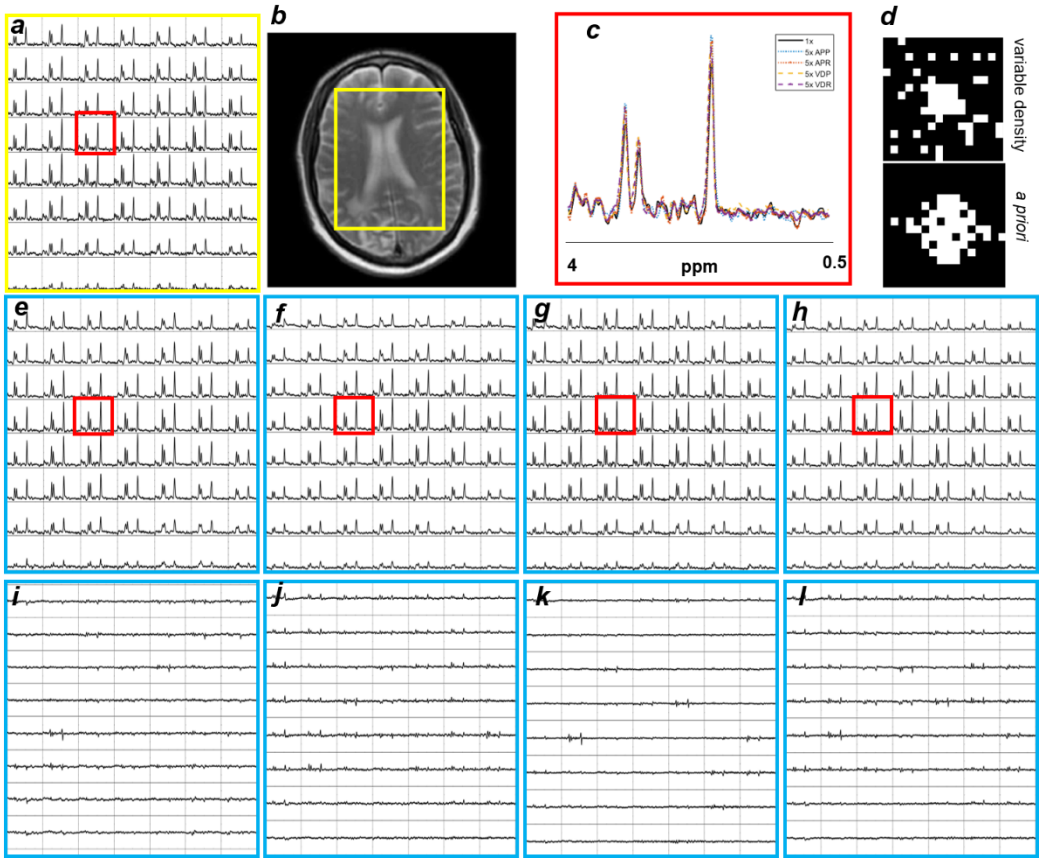

Figure 3.5: Displays the spectra of the *in vivo* brain comparing undersampled CS reconstruction (5X) to fully sampled Fourier reconstruction of a 52-year-old male patient. (a) MRSI reconstruction for the fully sampled *k*-space. (b) T_2 weighted anatomical scout with TE/TR = 104/3000 ms, FOV 22×22 cm, matrix 128×128). (c) Select voxel for comparison in red box (magnified). (d) variable density and *a priori* undersampling patterns. (e, i) *a priori* prospective CS-MRSI reconstruction and difference spectra. (f, j) variable density prospective CS-MRSI reconstruction and difference spectra. (g, k) *a priori* retrospective CS-MRSI reconstruction and difference spectra. (h, l) variable density retrospective CS-MRSI reconstruction and difference spectra.

The metabolite maps for the reconstructions for variable density undersampling were centered at the anatomy and did not comply fidelity with fully sampled spectra.

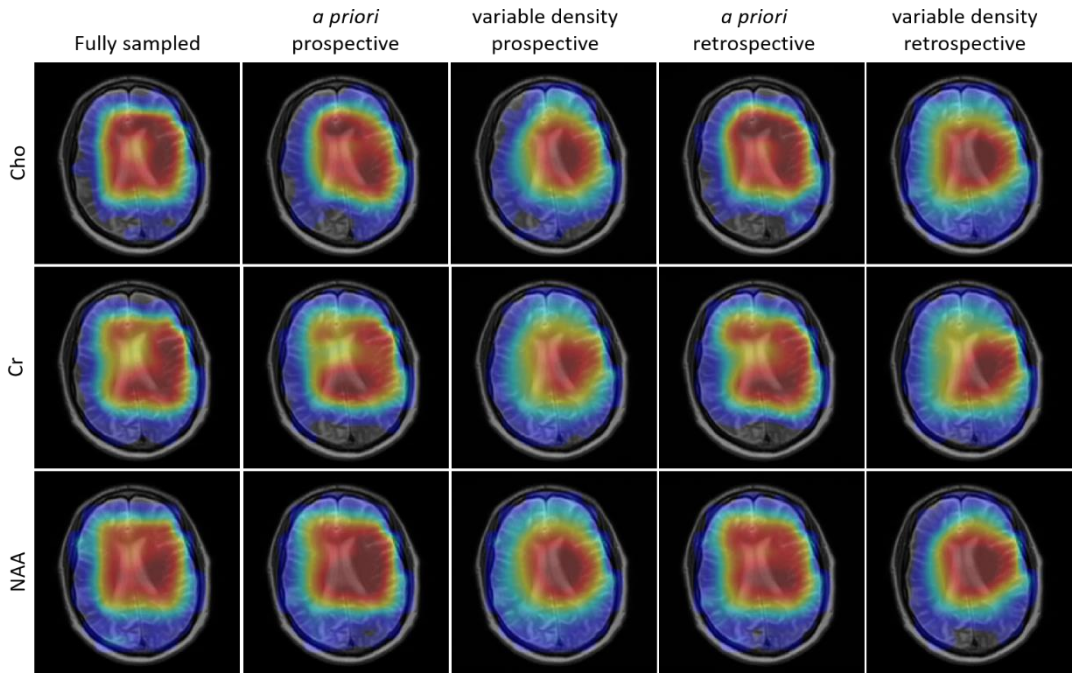

Figure 3.6: *In vivo* brain metabolite maps for the the fully sampled and 5X CS reconstructed spectra displayed in Figure 3.5. Choline (Cho), Creatine (Cr) and N-acetyl aspartate (NAA) maps are generated as the area under the respective peak linewidths.

Additionally, 3X undersampled data was acquired to determine the feasibility of prospective variable density undersampling.

Figure 3.7 compares the prospective and retrospective 3X undersampled CS-MRSI reconstructions with the fully sampled reconstruction for the *in vivo* brain data obtained from a 52-year-old male patient screened for lung cancer with brain metastasis. Figure 3.7(e) and 3.7(f) represent the prospective CS-MRSI reconstruction for the *a priori* and variable density undersampled acquisitions respectively. Figure 3.7(b) displays the anatomical scout. The difference between fully sampled and prospective *a priori*, variable density CS-MRSI reconstruction is as shown in figure 3.7(i) and 3.7(j) respectively. Similarly, the panel with Figure 3.7(h, i, j, k) shows the retrospective reconstruction and differences. The differences are evident for the prospective reconstructions when compared

to their respective retrospective reconstructions. Figure 3.8 depicts the metabolite maps generated from the reconstructed data for the *in vivo* brain in figure 3.7. The spatial distribution for the CS reconstructed spectra is comparable to fully sampled spectra. The metabolite peak ratios are consistent for individual voxels in CS reconstructed spectra for *a priori* undersampling compared to fully sampled spectra.

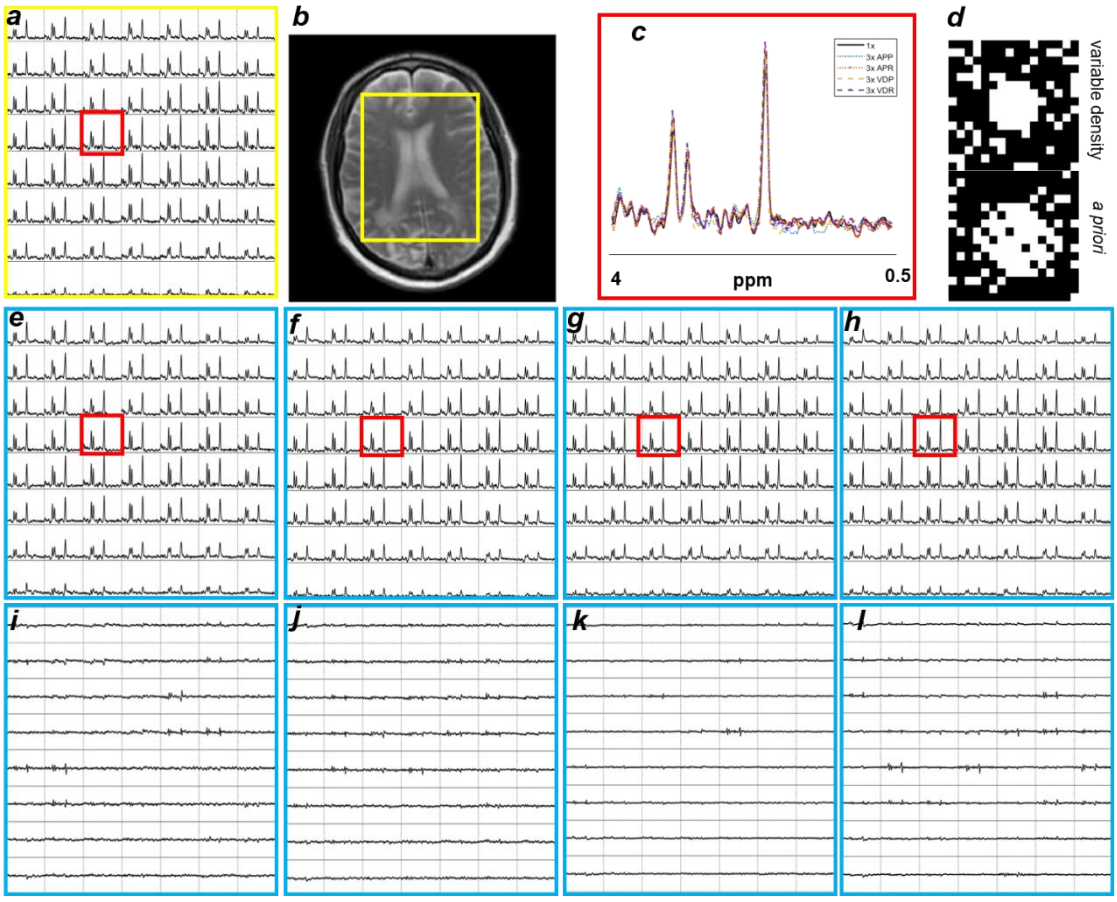

Figure 3.7: Displays the spectra of the *in vivo* brain comparing undersampled CS reconstruction (3X) to fully sampled Fourier reconstruction of a 52-year-old male patient. (a) MRSI reconstruction for the fully sampled *k*-space. (b) T_2 weighted anatomical scout with TE/TR = 104/3000 ms, FOV 22×22 cm, matrix 128×128). (c) Select voxel for comparison in red box (magnified). (d) variable density and *a priori* undersampling patterns. (e, i) *a priori* prospective CS-MRSI reconstruction and difference spectra. (f, j) variable density prospective CS-MRSI reconstruction and difference spectra. (g, k) *a priori* retrospective CS-MRSI reconstruction and difference spectra. (h, l) variable density retrospective CS-MRSI reconstruction and difference spectra.

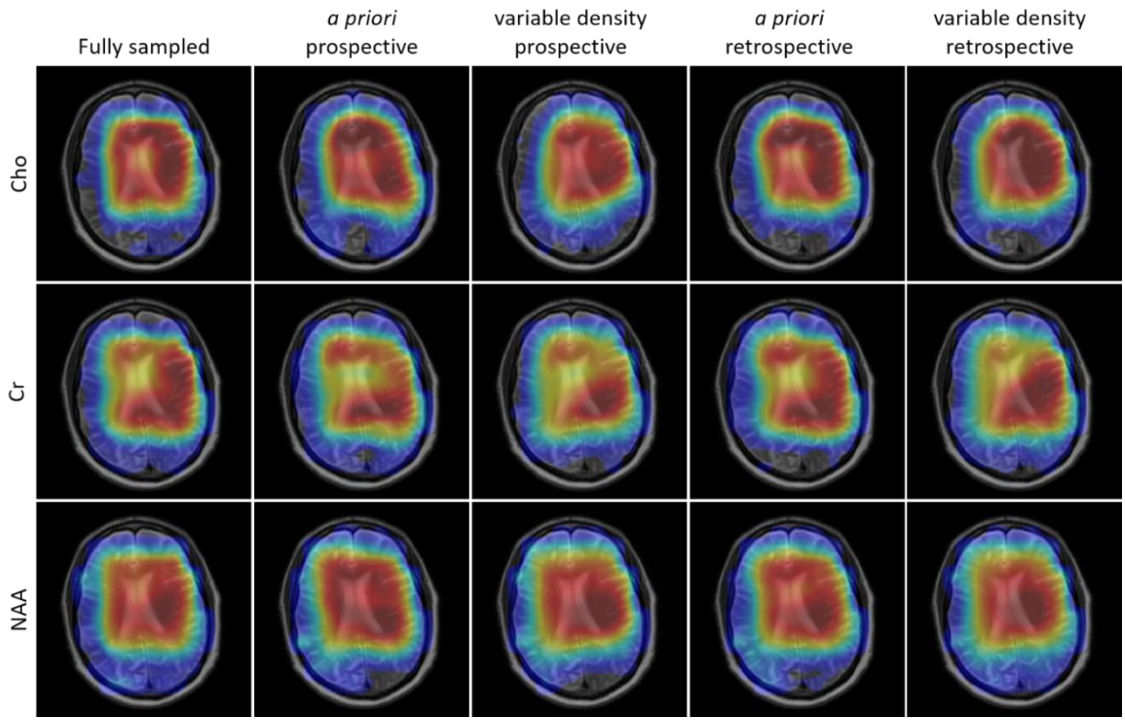

Figure 3.8: *In vivo* brain metabolite maps for the the fully sampled and 3X CS reconstructed spectra displayed in Figure 3.7. Choline (Cho), Creatine (Cr) and N-acetyl aspartate (NAA) maps are generated as the area under the respective peak linewidths.

The variable density undersampled reconstruction for the 3X undersampling yielded considerably better results compared to the 5X. The fidelity in reconstruction was yet not fulfilled by the variable density reconstruction for 3X.

Figure 3.9 shows the normalized root mean squared error (nRMSE) for the phantom and all nine *in vivo* brain CS-MRSI datasets for 5X. The nRMSE for NAA, creatine, and choline metabolites is computed individually for the undersampled CS reconstructed spectra datasets to fully sampled spectra dataset. The error is the lowest for the retrospective *a priori* spectra metabolites and the highest for the prospective variable density spectra metabolites in most cases. Voxel-wise paired *t*-tests comparing the CS reconstructed spectra to the fully sampled spectra yielded *p* values greater than 0.05 indicating fidelity for the *a priori* reconstructions, whereas, there were statistical

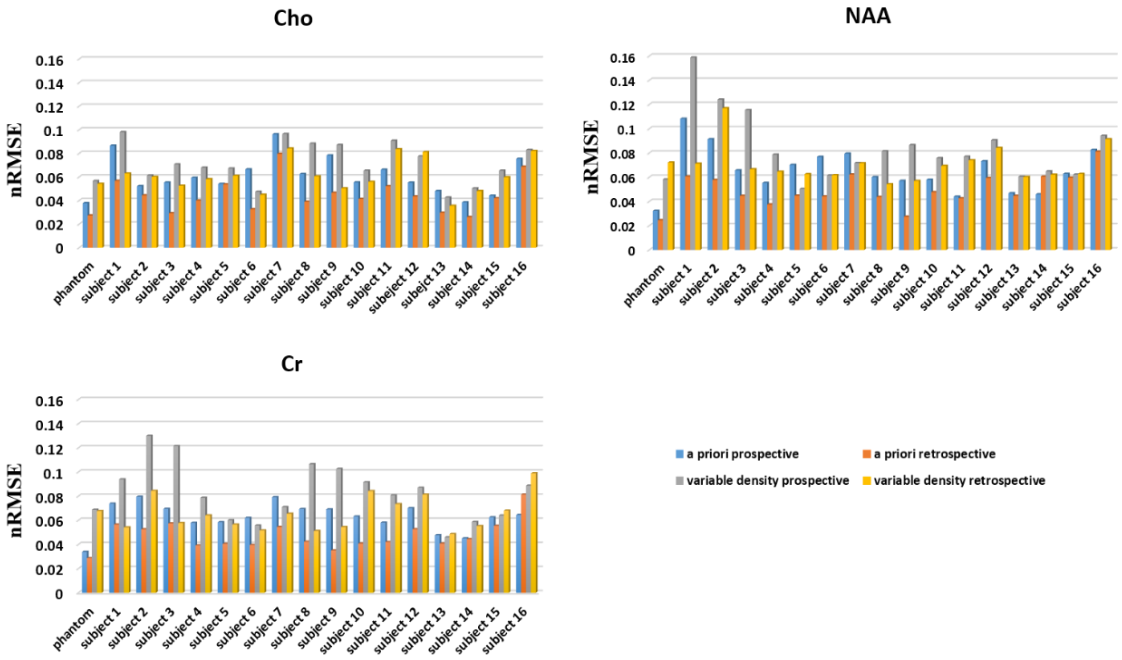

Figure 3.9: Normalized Root Mean Squared Error (nRMSE) plots for voxels located within the selected VOI of the phantom and brain for 5× CS-MRSI. The NAA, Creatine and Choline metabolite profiles for the CS reconstructed datasets is compared to the fully sampled reconstruction.

differences in the reconstructions for the variable density. A similar trend is observed for the nRMSE for the 3X acceleration for 5 subjects as depicted in figure 3.10. The nRMSE values did not exceed 8 % and was lower than the 5X error as expected.

Demographics of the patients scanned, the reason for MRI, mean metabolite ratios and standard deviations for NAA/Cr, Cho/NAA and Cho/Cr are tabulated in Table 3.1. The patient population consisted of 8 female and 8 male patients that included, healthy, tumor and non-tumor cases. The corresponding metabolite ratios from MRSI for 1X (fully sampled), 5X and 3X (for 5 patients) *a priori* and variable density CS-MRSI reconstructions are documented. Expected variations are observed with mean ratios being consistent between fully sampled and *a priori* reconstructions. The mean metabolite ratios for the variable density deviated from the fully sampled ratio means.

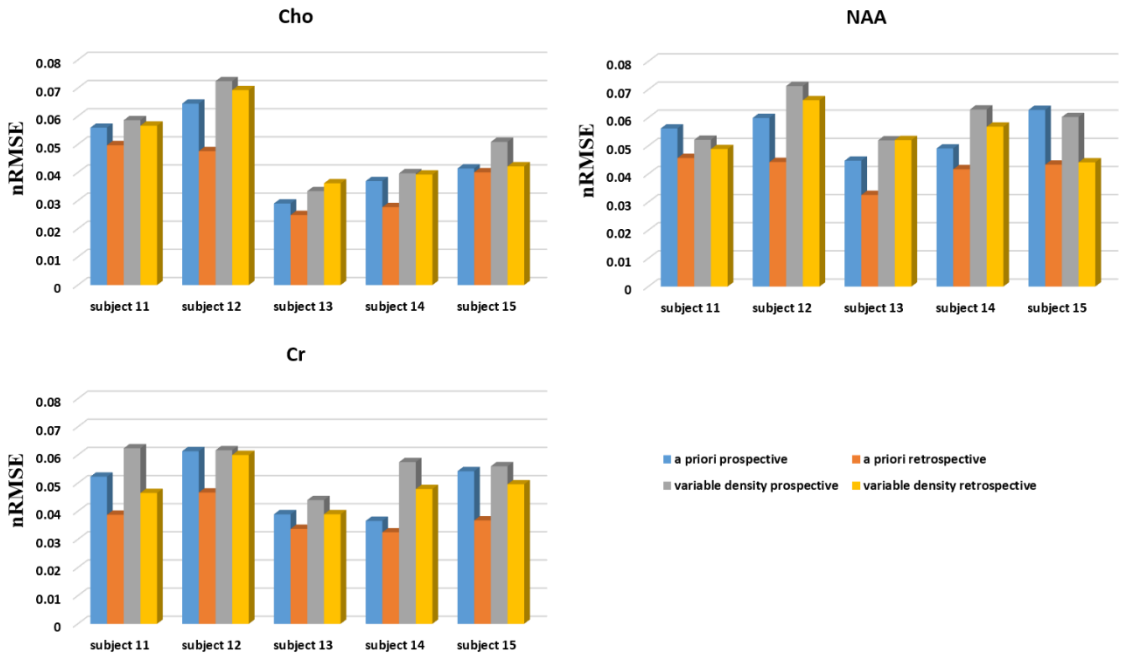

Figure 3.10: Normalized Root Mean Squared Error (nRMSE) plots for voxels located within the selected VOI of the *in vivo* brain for 3X CS-MRSI in 5 subjects. The NAA, Creatine and Choline metabolite profiles for the CS reconstructed datasets is compared to the fully sampled reconstruction.

3.4 Discussion and Conclusion

The proposed CS-MRSI protocol was employed as part of a routine MRI screening protocol. A five-fold reduction in scan time was achieved for PRESS-based *in vivo* brain MRSI. The CS-based reconstructions preserved spectral and spatial resolution with negligible differences for the *a priori* undersampling. The sparsity and the incoherence requirements for the iterative reconstruction were better fulfilled by the *a priori* undersampling strategy when compared to the variable-density approach since it sampled the most significant *k*-space locations instead of a pseudo-random assumption. The previous study from our group focused on the evaluation of the in-house developed

reconstruction algorithm and retrospectively demonstrated the feasibility of the CS-MRSI method [18, 19]. Undersampling strategies were examined to determine the most suitable pattern for CS-MRSI [20]. The retrospective evaluation confirmed variable density and *a priori* approach are feasible. In this study, we further evaluated the efficacy of the two methods prospectively.

Successful CS-MRSI reconstruction depends on the sparsity of the data. The variable density undersampling expects the most important points in spatial-spectral *k*-space to be confined at the center. This may not always be true when using phased array coils. The location of each coil and its sensitivity plays a major role in defining the sparse regions of the acquired *k*-space. Tailored undersampling for each channel is recommended for variable density undersampling. The current implementation did not allow such channel-wise undersampling and can be considered for future implementations. The *a priori* undersampling strategy determined the fidelity of CS-MRSI.

Apart from the qualitative inspection of the metabolite maps and spectra, the CS-MRSI reconstructions for the undersampled acquisitions are compared to the fully sampled spectra. Paired t-test were conducted and p-value threshold of 0.05 was considered optimal as in this study we were testing for non-significant differences and assessing spectral and spatial fidelity in the reconstruction. A p-value < 0.05 was considered to indicate a statistically significant difference between the reference and accelerated dataset, and thus, suggestive of a failed reconstruction. In our study, the p-values for the *a priori* reconstructions signified fidelity to the fully sampled spectra whereas the variable density reconstructions failed. MRSI analysis methods have commonly made use of metabolite ratios, which conveniently removes concerns for signal calibration and correction for

detection sensitivity variability. The mean and standard deviations for the NAA/Cr, Cho/NAA, Cho/Cr is tabulated in table 3.1. In normal adult brain, the concentration of NAA is always higher than the Cho and Cr. Increased concentration of Cho compared to NAA signifies tumor. The large Cho/NAA ratio is observed in subject 2 with mean and standard deviation = 1.50 ± 1.42. The expectations from the undersampled CS-MRSI reconstructions is to match the metabolite ratios of the fully sampled data. The metabolite ratios for the *a priori* reconstructions are having negligible deviation from the metabolite ratios for the fully sampled data. This provided additional evidence for the feasibility of the approach.

The pattern generation for *a priori* was based on the anatomical scout *k*-space. The important points in *k*-space were therefore targeted more efficiently with this method. The approach was more tailored to the anatomy and relied less on the chance of encoding the sparse *k*-space and had the coil weighting information. For higher accelerations, the *a priori* patterns are confined to a central region and do not sample any high-frequency *k*-space regions. This results in voxel bleeding and therefore lower spatial resolution. For higher accelerations, a combination of *a priori* for the central significant *k*-space encoding and variable density for peripheral *k*-space encoding is recommended.

Comparative studies require acquired data points to be subjected to the same conditions. Subject motion between and during scans is expected due to the long acquisition time. Motion is the major contributor to the differences between retrospective and prospective reconstructions. Minor fluctuations in the metabolite map comparison for the *a priori* retrospective CS-MRSI reconstruction and fully sampled MRSI are attributed to the irregular minimization for the finer coefficients during the iterative reconstruction.

In the current implementation, the weighting parameters for the l_1 norm and TV were fixed for all data channels and subjects. Since SNR depends on the coil location and the physiology of the patient, the regularization weights need to be tailored accordingly. A detailed account of the various factors affecting data acquisition and post-processing is discussed in the following chapter.

In conclusion, it has been demonstrated that 2D MRSI can be accelerated by 80% using compressed sensing in the clinical setting, with minimal loss in spectral fidelity and accuracy in metabolite quantification. This methodological advancement has the potential to increase the utility of MRSI in the routine clinical evaluation of brain morphology and function, as well as in other organs.

Table 3.1: Patient demographics and related information from MRI and MRSI for 16 subjects**,** scanned for brain related concerns**. (**NAA – N-acetyl aspartate, Cr – creatine, Cho – choline)

Case	Gender	Age	Reason for MRI	NAA/Cr		Cho/NAA		Cho/Cr	
Phantom	NA	NA	Test	1X:	1.2 ± 0.03	1X:	0.76 ± 0.06	1X:	0.92 ± 0.07
				5X APR:	1.21 ± 0.04	5X APR:	0.77 ± 0.07	5X APR:	0.93 ± 0.08
				5X APP:	1.21 ± 0.12	5X APP:	0.75 ± 0.03	5X APP:	0.93 ± 0.10
				5X VDR:	1.23 ± 0.07	5X VDR:	0.78 ± 0.06	5X VDR:	0.90 ± 0.05
				5X VDP:	1.27 + 0.03	5X VDP:	0.74 ± 0.04	5X VDP:	0.89 ± 0.02
Subject 1	F	47	Breast cancer surveillance	1X:	0.85 ± 0.29	1X:	1.14 ± 0.25	1X:	0.96 ± 0.30
				5X APR:	1.01 ± 0. 39	5X APR:	0.98 ± 0.23	5X APR:	0.98 ± 0.18
				5X APP:	1.17 ± 0.43	5X APP:	0.93 ± 0.29	5X APP:	1.01 ± 0.15
				5X VDR:	0.97 ± 0.11	5X VDR:	1.2 ± 0.33	5X VDR:	0.91 ± 0.21
				5X VDP:	0.95 ± 0.41	5X VDP:	1.25 ± 0.22	5X VDP:	0.89 ± 0.33
Subject 2	M	44	Lung cancer eval for progression	1X:	0.31 ± 0.19	1X:	1.50 ± 1.42	1X:	0.94 ± 0.61
				5X APR:	0.36 ± 0.23	5X APR:	1.28 ± 0.32	5X APR:	0.81 ± 0.20
				5X APP:	0.41 ± 0.20	5X APP:	1.18 ± 0.31	5X APP:	0.82 ± 0.23
				5X VDR:	1.13 ± 0.32	5XVDR:	0.92 ± 0.19	5XVDR:	1.01 ± 0.23
				5X VDP:	1.17 ± 0.38	5X VDP:	0.96 ± 0.28	5X VDP:	1.03 ± 0.21
Subject 3	M	77	Lung cancer with brain metastasis	1X:	0.95 ± 1.35	1X:	0.63 ± 0.89	1X:	0.62 ± 3.12
				5X APR:	1.02 ± 1.38	5X APR:	0.64 ± 0.45	5X APR:	1.08 ± 2.51
				5X APP:	1.04 ± 1.26	5X APP:	0.88 ± 1.01	5X APP:	0.13 ± 3.78
				5X VDR:	1.54 ± 0.64	5XVDR:	0.76 ± 0.70	5XVDR:	1.20 ± 1.34

				5X VDP:	0.69 ± 3.13	5X VDP:	0.65 ± 0.43	5X VDP:	0.50 ± 1.99
Subject 4	M	66	Lung cancer w/ brain metastasis	1X:	1.02 ± 0.11	1X:	0.87 ± 0.22	1X:	0.9 ± 0.27
				5X APR:	1.03 ± 0.09	5X APR:	0.95 ± 0.19	5X APR:	0.98 ± 0.22
				5X APP:	1.0 ± 0.09	5X APP:	0. 91 ± 0.25	5X APP:	0.9 ± 0.18
				5X VDR:	0.99 ± 0.08	5X VDR:	0.98 ± 0.18	5X VDR:	0.97 ± 0.67
				5X VDP:	1.01 ± 0.44	5X VDP:	1.04 ± 0.26	5X VDP:	1.01 ± 0.67
Subject 5	F	60	Lymphoma, Rule out meningeal disease	1X:	1.04 ± 0.27	1X:	0.86 ± 0.29	1X:	0.86 ± 0.29
				5X APR:	1.07 ± 0.26	5X APR:	0.75 ± 0.29	5X APR:	0.76 ± 0.27
				5X APP:	1.03 ± 0.21	5X APP:	0.76 ± 0.26	5X APP:	0.75 ± 0.20
				5X VDR:	1.05 ± 0.25	5X VDR:	0.87 ± 0.23	5X VDR:	0.88 ± 0.18
				5X VDP:	0.98 ± 0.17	5X VDP:	0.88 ± 0.20	5X VDP:	0.85 ± 0.19
Subject 6	M	68	Lung cancer, eval for metastasis	1X:	0.92 ± 0.21	1X:	1.04 ± 0.33	1X:	0.90 ± 0.26
				5X APR:	0.86 ± 0.18	5X APR:	1.16 ± 0.28	5X APR:	0.97 ± 0.19
				5X APP:	0.86 ± 0.17	5X APP:	1.0 ± 0.22	5X APP:	0.85 ± 0.17
				5X VDR:	0.89 ± 0.16	5X VDR:	1.05 ± 0.21	5X VDR:	0.91 ± 0.16
				5X VDP:	0.87 ± 0.17	5X VDP:	0.98 ± 0.18	5X VDP:	0.84 ± 0.15
Subject 7	F	77	NSCLC w/ brain metastasis	1X:	2.02 ± 0.33	1X:	0.45 ± 0.16	1X:	0.88 ± 0.33
				5X APR:	2.20 ± 0.27	5X APR:	0.41 ± 0.11	5X APR:	0.86 ± 0.18
				5X APP:	2.26 ± 0.30	5X APP:	0.43 ± 0.17	5X APP:	0.83 ± 0.42
				5X VDR:	2.11 ± 0.22	5X VDR:	0.49 ± 0.20	5X VDR:	0.93 ± 0.66
				5X VDP:	2.13 ± 0.15	5X VDP:	0.47 ± 0.29	5X VDP:	0.95 ± 0.13
Subject 8	M	77	NSCLC w/ brain met	1X:	1.13 ± 0.28	1X:	0.76 ± 0.22	1X:	0.83 ± 0.22
				5X APR:	1.05 ± 0.24	5X APR:	0.78 ± 0.18	5X APR:	0.80 ± 0.17

				5X APP:	1.11 ± 0.30	5X APP:	0.76 ± 0.21	5X APP:	0.82 ± 0.23
				5X VDR:	1.01 ± 0.21	5X VDR:	0.88 ± 0.19	5X VDR:	0.87 ± 0.20
				5X VDP:	0.91 ± 0.28	5X VDP:	0.93 ± 0.26	5X VDP:	0.72 ± 2.3
Subject 9	F	57	Oligoastrocytoma	1X:	1.04 ± 0.23	1X:	0.96 ± 0.26	1X:	0.99 ± 0.33
				5X APR:	1.07 ± 0.21	5X APR:	0.96 ± 0.25	5X APR:	1.01 ± 0.30
				5X APP:	1.11 ± 0.27	5X APP:	0.94 ± 0.25	5X APP:	1.01 ± 0.36
				5X VDR:	1.11 ± 0.21	5X VDR:	1.11 ± 0.28	5X VDR:	1.21 ± 0.32
				5X VDP:	1.24 ± 0.30	5X VDP:	0.92 ± 0.26	5X VDP:	1.18 ± 0.55
Subject 10	F	56	GBM	1X:	1.04 ± 0.27	1X:	0.86 ± 0.28	1X:	0.85 ± 0.29
				5X APR:	1.06 ± 0.26	5X APR:	0.75 ± 0.29	5X APR:	0.76 ± 0.27
				5X APP:	1.03 ± 0.20	5X APP:	0.76 ± 0.26	5X APP:	0.75 ± 0.26
				5X VDR:	1.05 ± 0.24	5X VDR:	0.87 ± 0.23	5X VDR:	0.88 ± 0.18
				5X VDP:	0.98 ± 0.17	5X VDP:	0.88 ± 0.20	5X VDP:	0.85 ± 0.18
Subject 11	M	52	Lung cancer w/ brain metastasis	1X:	1.67 ± 0.37	1X:	0.66 ± 0.08	1X:	1.12 ± 0.25
				5X APR:	1.69 ± 0.37	5X APR:	0.64 ± 0.13	5X APR:	1.10 ± 0.34
				5X APP:	1.90 ± 0.36	5X APP:	0.60 ± 0.19	5X APP:	1.14 ± 0.41
				5X VDR:	1.73 ± 0.35	5X VDR:	0.66 ± 0.11	5X VDR:	1.15 ± 0.32
				5X VDP:	1.78 ± 0.24	5X VDP:	0.62 ± 0.12	5X VDP:	1.09 ± 0.24
				3X APR:	1.66 ± 0.37	3X APR:	0.65 ± 0.13	3X APR:	1.09 ± 0.32
				3X APP:	1.85 ± 0.44	3X APP:	0.64 ± 0.16	3X APP:	1.18 ± 0.40
				3X VDR:	1.72 ± 0.34	3X VDR:	0.66 ± 0.14	3X VDR:	1.14 ± 0.35
				3X VDP:	1.87 ± 0.33	3X VDP:	0.62 ± 0.14	3X VDP:	1.17 ± 0.34
Subject 12	F	58	Lymphoma, Rule out	1X:	1.92 ±0.45	1X:	0.46 ± 0.10	1X:	0.85 ± 0.10
				5X APR:	2.03 ± 0.62	5X APR:	0.49 ± 0.13	5X APR:	0.95 ± 0.24

			meningeal disease	5X APP:	2.02 ± 0.58	5X APP:	0.50 ± 0.17	5X APP:	0.95 ± 0.23
				5X VDR:	2.06 ± 0.66	5X VDR:	0.50 ± 0.10	5X VDR:	1.01±0.28
				5X VDP:	2.17 ± 0.80	5X VDP:	0.53 ± 0.08	5X VDP:	1.12 ± 0.26
				3X APR:	1.92 ± 0.56	3X APR:	0.46 ± 0.17	3X APR:	0.83 ± 0.25
				3X APP:	2.21 ± 0.73	3X APP:	0.47 ± 0.19	3X APP:	0.94 ± 0.26
				3X VDR:	2.08 ± 0.61	3X VDR:	0.47 ± 0.13	3X VDR:	0.94 ± 0.28
				3X VDP:	2.12 ± 0.54	3X VDP:	0.52 ± 0.19	3X VDP:	1.04 ± 0.29
Subject 13	F	33	Breast cancer surveillance	1X:	2.20 ± 0.37	1X:	0.41 ± 0.11	1X:	0.90 ± 0.23
				5X APR:	2.26 ± 0.34	5X APR:	0.39 ± 0.07	5X APR:	0.87 ± 0.19
				5X APP:	2.27 ± 0.36	5X APP:	0.38 ± 0.06	5X APP:	0.87 ± 0.19
				5X VDR:	2.29 ± 0.28	5X VDR:	0.39 ± 0.05	5X VDR:	0.88 ± 0.14
				5X VDP:	2.21 ± 0.24	5X VDP:	0.39 ± 0.06	5X VDP:	0.87 ± 0.14
				3X APR:	2.25 ± 0.35	3X APR:	0.39 ± 0.09	3X APR:	0.87 ± 0.24
				3X APP:	2.24 ± 0.39	3X APP:	0.36 ± 0.08	3X APP:	0.80 ± 0.20
				3X VDR:	2.27 ± 0.25	3X VDR:	0.37 ± 0.09	3X VDR:	0.85 ± 0.23
				3X VDP:	2.28 ± 0.35	3X VDP:	0.37 ± 0.08	3X VDP:	0.84 ± 0.23
Subject 14	M	54	Lung cancer w/ brain metastasis	1X:	1.76 ± 0.29	1X:	0.54 ± 0.12	1X:	0.94 ± 0.22
				5X APR:	1.71 ± 0.32	5X APR:	0.62 ± 0.19	5X APR:	1.02 ± 0.21
				5X APP:	1.77 ± 0.24	5X APP:	0.64 ± 0.11	5X APP:	1.11 ± 0.14
				5X VDR:	1.75 ± 0.41	5X VDR:	0.61 ± 0.15	5X VDR:	1.04 ± 0.25
				5X VDP:	1.73 ± 0.31	5X VDP:	0.61 ± 0.16	5X VDP:	1.03 ± 0.24
				3X APR:	1.69 ± 0.28	3X APR:	0.61 ± 0.17	3X APR:	1.01 ± 0.25
				3X APP:	1.77 ± 0.28	3X APP:	0.61 ± 0.12	3X APP:	1.05 ± 0.15
				3X VDR:	1.68 ± 0.31	3X VDR:	0.64 ± 0.27	3X VDR:	1.02 ± 0.22

				3X VDP:	1.78 ± 0.43	3X VDP:	0.62 ± 0.23	3X VDP:	1.04 ± 0.18
Subject 15	F	60	Pituitary adenoma	1X:	0.98 ± 0.29	1X:	1.19 ± 0.60	1X:	1.05 ± 0.31
				5X APR:	0.99 ± 0.19	5X APR:	0.99 ± 0.20	5X APR:	0.97 ± 0.20
				5X APP:	0.90 ± 0.16	5X APP:	0.97 ± 0.16	5X APP:	0.88 ± 0.21
				5X VDR:	0.86 ± 0.13	5X VDR:	1.14 ± 0.46	5X VDR:	0.97 ± 0.33
				5X VDP:	0.91 ± 0.22	5X VDP:	1.09 ± 0.41	5X VDP:	0.99 ± 0.51
				3X APR:	0.92 ± 0.25	3X APR:	1.12 ± 0.18	3X APR:	1.06 ± 0.25
				3X APP:	0.99 ± 0.15	3X APP:	0.99 ± 0.18	3X APP:	1.07 ± 0.32
				3X VDR:	0.99 ± 0.19	3X VDR:	1.02 ± 0.27	3X VDR:	0.98 ± 0.18
				3X VDP:	0.85 ± 0.16	3X VDP:	1.03 ± 0.17	3X VDP:	0.87± 0.18
Subject 16	M	75	Lung cancer w/ brain metastasis	1X:	0.96 ± 0.22	1X:	0.85 ± 0.68	1X:	0.75 ± 0.27
				5X APR:	0.91 ± 0.17	5X APR:	0.99 ± 0.40	5X APR:	0.87 ± 0.31
				5X APP:	0.90 ± 0.22	5X APP:	1.22 ± 0.78	5X APP:	0.99 ± 0.25
				5X VDR:	1.11 ± 0.23	5X VDR:	0.80 ± 0.21	5X VDR:	0.88 ± 0.32
				5X VDP:	0.71 ± 2.4	5X VDP:	0.93 ± 0.26	5X VDP:	0.54 ± 2.92

CHAPTER 4

PROCEDURES AND CHALLENGES IN CS-MRSI

The integration of CS-MRSI in routine clinical studies is technically challenging and has major hindrances both at the data acquisition and the post-processing front. For the data acquisition, familiarity with the technical issues concerning conventional MRSI data is required to acquire good quality data. Unlike anatomical MRI, MRSI is yet to be fully automated and additional steps such as volume of interest (VOI) planning and sometimes manual shimming are required. For the post-processing of CS-MRSI data, several post-processing steps are required to resolve the spectra along with optimized iterative reconstruction. In this chapter, a note on the preliminary experience of CS-MRSI on a 3 T Discovery 750w (GE HealthCare: GE, Milwaukee, WI) clinical scanner is described in the first section followed by the data processing methods involved in CS reconstruction.

4.1 CS-MRSI Data Acquisition

The study described in chapter 3 involved fully sampled PRESS MRSI data acquisition to compare and determine the undersampled CS reconstructions. In the future, it is envisioned that only undersampled MRSI scans will be performed. MRSI is performed with a 12-channel head coil which is routinely used for the MRI study. Before beginning the scan, the control variable "Autolock" is set to 1 to save all raw data files (Refer to figure 4.1). Post MRI, a high resolution (10 mm thickness) T_2 weighted axial image is acquired. This image is used as a scout for vendor-supplied PRESS MRSI prescription. The first step in prescribing an MRSI is to place a rectangular box of the spectral volume of interest

(VOI) on the T2 axial on the largest cross-sectional area of the brain. The size of the box is adjusted to the brain with minimal inclusion of the cranial fat. To further maximize the exclusion of the fat, six very selective saturation (VSS) bands are placed at the corners of the VOI to best conform the spectroscopic volume to the actual shape of the brain as shown in figure 4.1. Next, we perform an automated prescan procedure that calibrates the transmit and receive gains, optimized the magnetic field shimming, and calibrates the transmit frequency. If the linewidth is suboptimal (>15 Hz) then a manual shimming is performed with the spectro-prescan tool (figure 4.2) by adjusting the shimming gradients such that the FID oscillates as far out as possible. The transmitter gain and frequency can also be adjusted for improved spectral quality but most often they are not toggled. Once the prescan settings are optimized, we can acquire high-quality fully sampled spectra successfully.

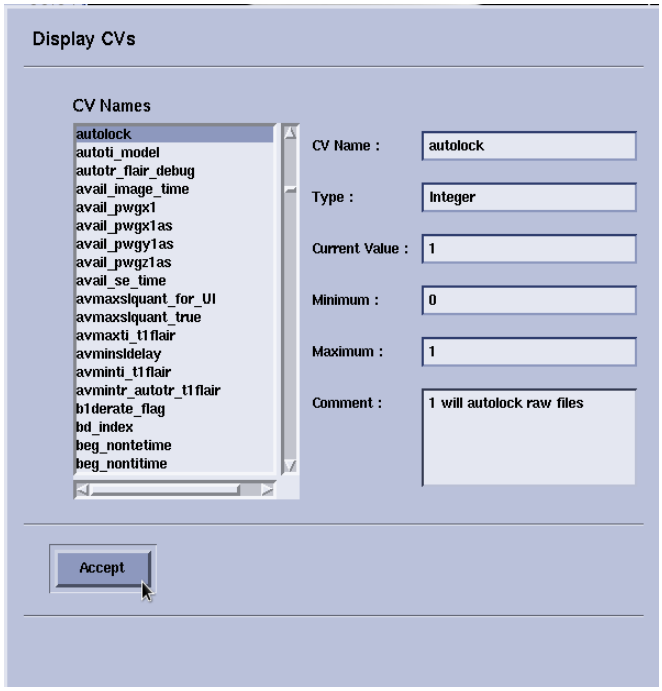

Figure 4.1: control variable tool. The tool is found under scan> research > Display CV's

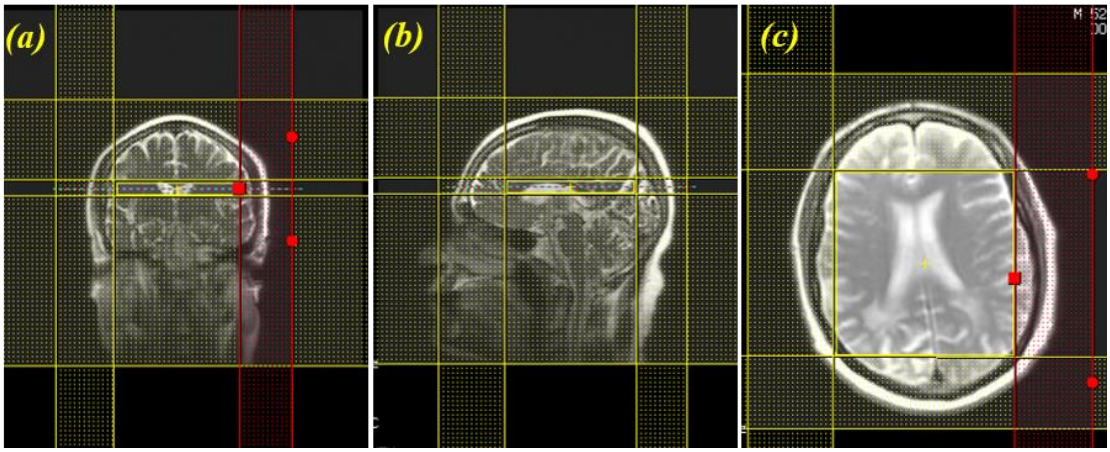

Figure 4.2: Volume of interest (VOI) and VSS band placement on T_2 weighted axial scout, excluding the cranial fat

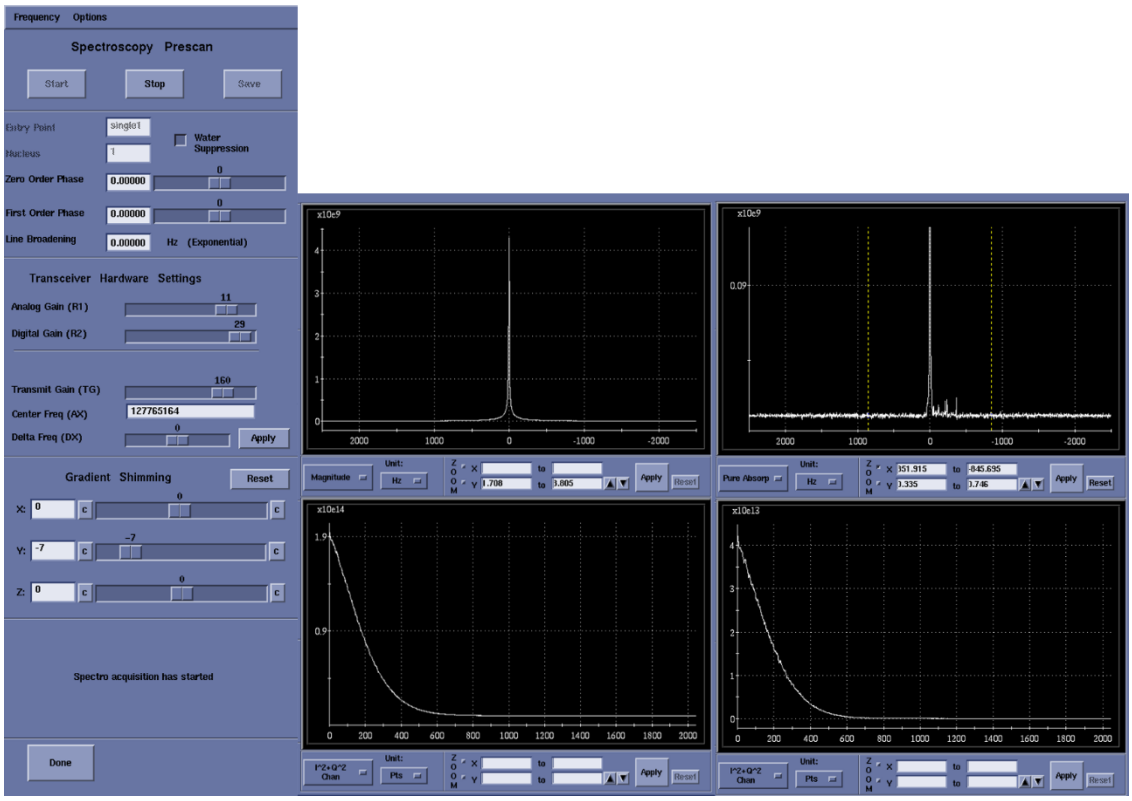

Figure 4.3: Spectro prescan tool for manual adjustments of shimming, gain and frequency parameters for optimal linewidth. The right most column represents the water suppressed spectra and FID.

.

For the CS-MRSI undersampled data acquisition, the modified PRESS sequence is initialized by directing the path to the sequence files (Refer to figure 4.4). The undersampling method is now loaded onto the scanner. The "CSSel" control variable is toggled for fully sampled, variable density, or *a priori* undersampling. A pre-generated variable density mask is made available in the same folder as the modified PRESS sequence folder ("/usr/g/bin/CSMRSI/"). The undersampling masks can be replaced when necessary but with the same filenames. Once the undersampling PRESS sequence is loaded successfully, "A GRx is lost" cautionary message appears. The VOI, VSS, and parameter prescriptions can be copied from the fully sampled prescription (In the future when only undersampled scans are performed, the vendor PRESS sequence will be used only for VOI

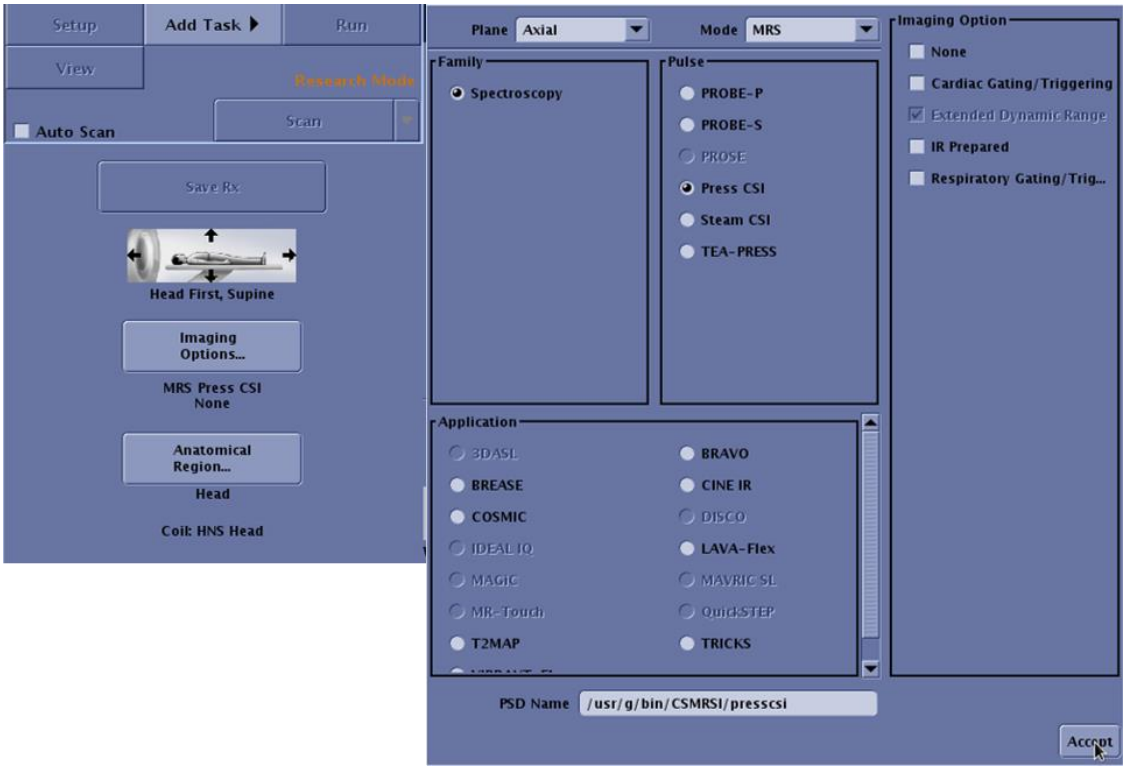

Figure 4.4: Imaging options tool for loading the modified CS-MRSI PRESS sequence. Manual entry is required in the PSD name. Once loaded successfully, a cautionary GRx error is displayed requesting re-prescription.

planning, prescan, and shimming. NOTE: The zeros in the undersampling pattern interfere with the spectro-prescan process and should be avoided). At this stage the manual prescan option is selected to bypass the auto prescan (NOTE: this re-evaluates the shim, gain and frequency parameters and must be avoid for data consistency).

To generate the *a priori* undersampling mask, the raw *k*-space of the anatomical scout is transferred to a portable universal serial bus (USB) drive. An in-house function in MATLAB generates the undersampling pattern and save a binary file .txt format. This file is transferred to the modified sequence folder.

4.2 Challenges in CS-MRSI Data Acquisition

In *in vivo* brain MRSI, the magnetic susceptibility-related field inhomogeneity from the brain-air cavity regions increases proportionally. A high-quality magnetic field shimming is necessary which requires expertise and additional time. Ideally, such regions are avoided during VOI planning, however, the study of diseased tissue in such regions is difficult and may not yield optimal results. Overlapping fat resonances arising from the skull is an additional hindrance to data quality. Although the volume suppression bands aid in suppressing the resonance from unwanted regions, quantifying a tumor close to the skull is a challenging task. Time spent on manual shimming affects the overall patient throughput at the clinic and tests the technician tolerance.

In multi-channel phased array coils, the sensitivity and relative position of the coil plays a major role in CS-MRSI. The low sensitive/ farther away coil acquires more noise compared to the coils closer to the slice. The iterative reconstruction essentially finds optimal solutions and thresholds noise. Spurious noise spikes may get resolved by the non-

linear conjugate gradient (NLCG) and may affect the reconstruction further along the pipeline. Proper tuning of regularization parameters is required for each channel.

4.3 Challenges in CS-MRSI Post-Processing

The MRSI reconstruction workflow shown in figure 2.8 successfully reconstructs for the fully sampled data however there are a few caveats to undersampled reconstruction using the same workflow. First, an iterative NLCG algorithm must be implemented to remedy the spurious noise in the spatial spectral-domain present to the non-encoded points in *k*-space. The NLCG cannot be performed after phase correction since this process fills the zero points in the spatial *k*-space and NLCG will not converge to an optimal solution. The raw undersampled spatial-spectral data has a large unsuppressed water peak and the NLCG algorithm tries to resolve for the water peak. In presence of such large dominant peaks, the low SNR metabolite signals are removed as noise and their temporal resolution is lost (Refer to figure 4.5 (a)). Therefore, the HLSVD water suppression filter, typically employed as one of the last steps in conventional MRSI, is used as the first step in CS-MRSI. The pre-processing is followed by a spectral Gaussian and spatial Hamming filter to remove the noise and the metabolites are distinctive as shown in figure 4.5 (c). The choice of apodization before or after the NLCG reconstruction did not change the outcome.

For successful CS-MRSI reconstruction, the CS requirements of sparsity and incoherent sampling must be fulfilled. The CS-MRSI reconstruction failed for the variable density undersampling strategy. The expectations with variable density undersampling was that the most significant points in *k*-space is at the center. Unfortunately, with phased array coil, the significant points in *k*-space may not always be at the center for each channel.

Figure 4.6 depicts the first time point of the fully sampled *k*-space with overlays of the variable density and *a priori* undersampling patterns. In the variable density case, a significant section of *k*-space with high intensity is not encoded whereas only a few significant points are missed by the *a priori* pattern.

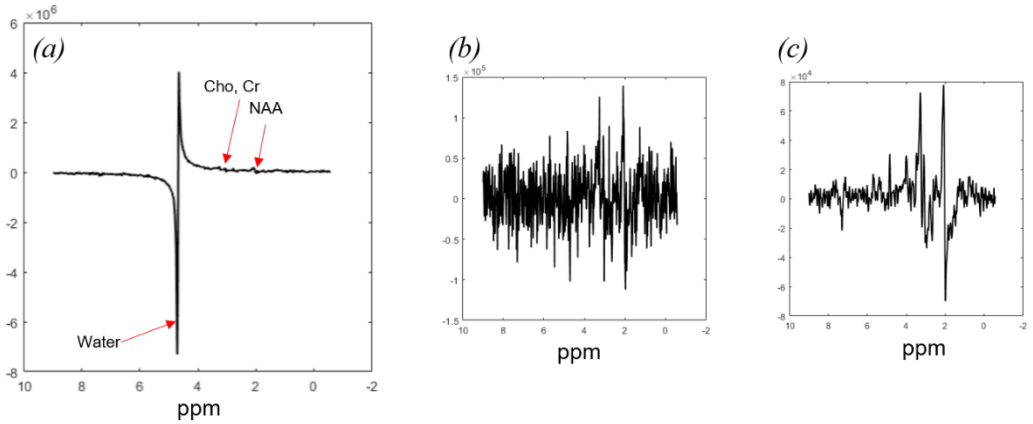

Figure 4.5: CS-MRSI post-processing (a) Raw spectra with large water peak. (b) Residual spectra post water removal. (c) Gaussian and Hamming filtered spectra with distinct peaks.

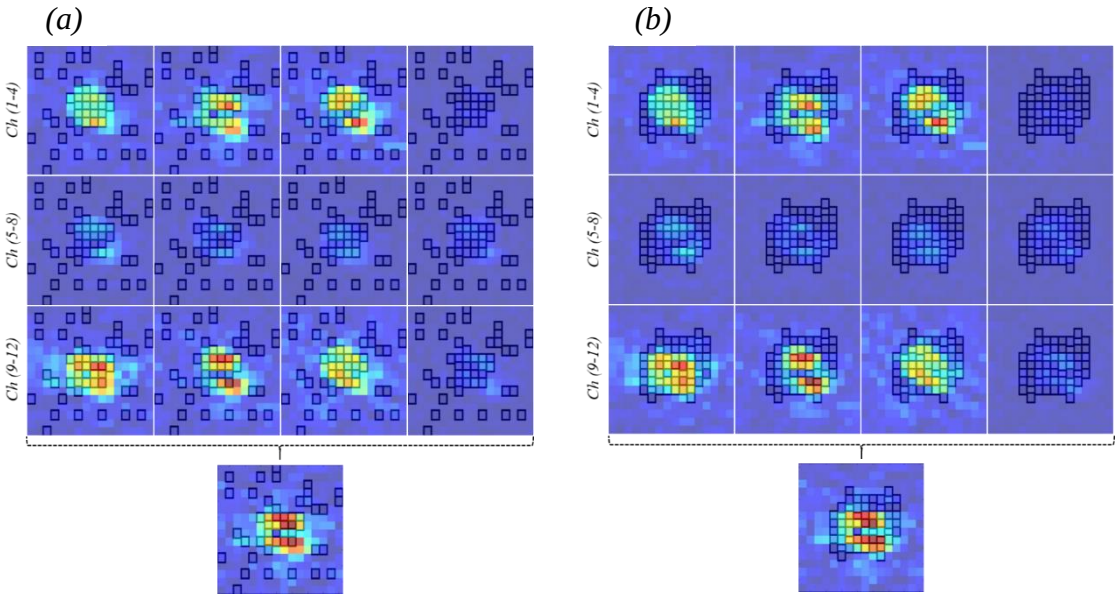

Figure 4.6: Channel wise first time point in fully sampled *k*-space with overlays of (a) variable density and (b) *a priori* undersampling patterns.

CHAPTER 5

IMPROVED RECONSTRCUTION USING A PRIORI SUPPORT

5.1 Introduction

In vivo ^{1}H MRSI is hampered by the low SNR of the metabolite signals. The development of phased array receiver coils has led to improved SNR as it employs multiple coils across the anatomy making it more sensitive [53,54]. Advanced image reconstruction methods such as compressed sensing (CS) can be used to reconstruct high-quality spectra from undersampled data sets. By incorporating prior information from anatomical MRI, which is always acquired for MRSI voxel planning, in the CS reconstruction, the spatial-spectral quality can be further improved since it preserves tissue boundaries and reduces partial volume effects [55,56]. The CS-MRSI reconstruction done previously in Chapter 3 involved the channel wise reconstruction of undersampled data followed by a weighted combination. In the previous method, the cost function is minimized for a normalized set of undersampled measurements to keep sparsity weighting parameters are same through all the channels. Since phased array coils are geometrically placed and are more sensitive to their immediate vicinity, the CS reconstruction could yield better results when the sensitivity maps are incorporated in the iterative reconstruction algorithm.

5.2 Materials and Methods

The coil sensitivity maps were obtained from the anatomical T_2 weighted scout using ESPIRiT [57]. This method computes the coil sensitivities by eigen value

decomposition in the image domain. The coil sensitivity maps were incorporated in the CS reconstruction algorithm described in chapter 3 as follows.

$$*€(m) = \|F_u Sm - y\|_2 + \lambda_{L1}\|Wm\|_1 + \lambda_{TV} TV(m) \quad (5.1)$$

where, y is the measured *k*-space data, m is the desired MRSI data, F_u, W, and TV are the Fourier transform, wavelet transform, and total variation operators, respectively. *S* is the coil sensitivity obtained from ESPIRiT. $\|\,.\,\|_1$ and $\|\,.\,\|_2$ are the l_1 and l_2 norm operators, respectively, λ_{L1} and λ_{TV} are the corresponding regularization parameter for the l_1 norm and TV operator, respectively. The $k_x - t$ matrix was encoded along each of the two dimensions using the Daubechies wavelet transform at all points in k_y. The regularization terms λ_{L1} and λ_{TV} were experimentally determined to be 0.001 and 0.005, respectively.

5.2.1 MRSI Data

The 5X variable density and *a priori* undersampled data described in chapter 3 where repurposed for the study.

5.2.2 Post Processing

A custom algorithm was implemented on MATLAB to reconstruct for the fully sampled and undersampled MRSI data sets. The residual water and fat were removed by Hankel-Lanczos Singular Value Decomposition (HLSVD) filtering followed by a 3 Hz Gaussian and Hamming apodization along the spectral and spatial dimension respectively. For the fully sampled data set, Fourier transformation, phase correction, and channel combination were performed to obtain 1X reference spectra and stored for quantitative comparison.

The filtered undersampled data sets were iteratively reconstructed based on the conjugate gradient algorithm. The CS-MRSI reconstruction with the coil sensitivity support was formulated as a convex optimization problem and iterative reconstructed for the cost function in equation 5.1. The CS reconstructed MRSI data for each channel was phase-corrected and combined. Metabolite maps were generated using the area under the curve method for N-acetyl aspartate (NAA), creatine (Cr), and choline (Cho). The resulting spectra were compared with the results from chapter 3.

5.3 Results

We study the utility of known support in the iterative process of the CS-MRSI reconstruction. Figure 5.1 (b) depicts the coil sensitivity maps obtained for the anatomical scout using ESPIRiT. The sensitivity maps were normalized with respect to the most sensitive coil. The modified CS-MRSI CS-MRSI reconstruction workflow is depicted in figure 5.2 wherein the sensitivity maps aided the evaluation of the cost function during iterative reconstruction. Figure 5.3 compares the *a priori* undersampled CS-MRSI

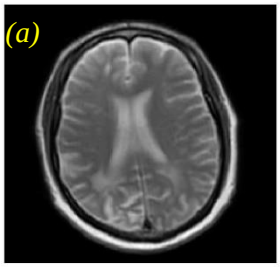

Anatomical Scout

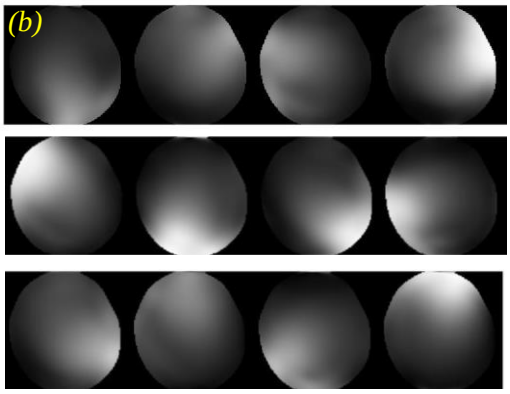

Figure 5.1: *A priori* support. (a) T_2 weighted anatomical scout. (b) Coil sensitivity maps generated using ESPIRiT.

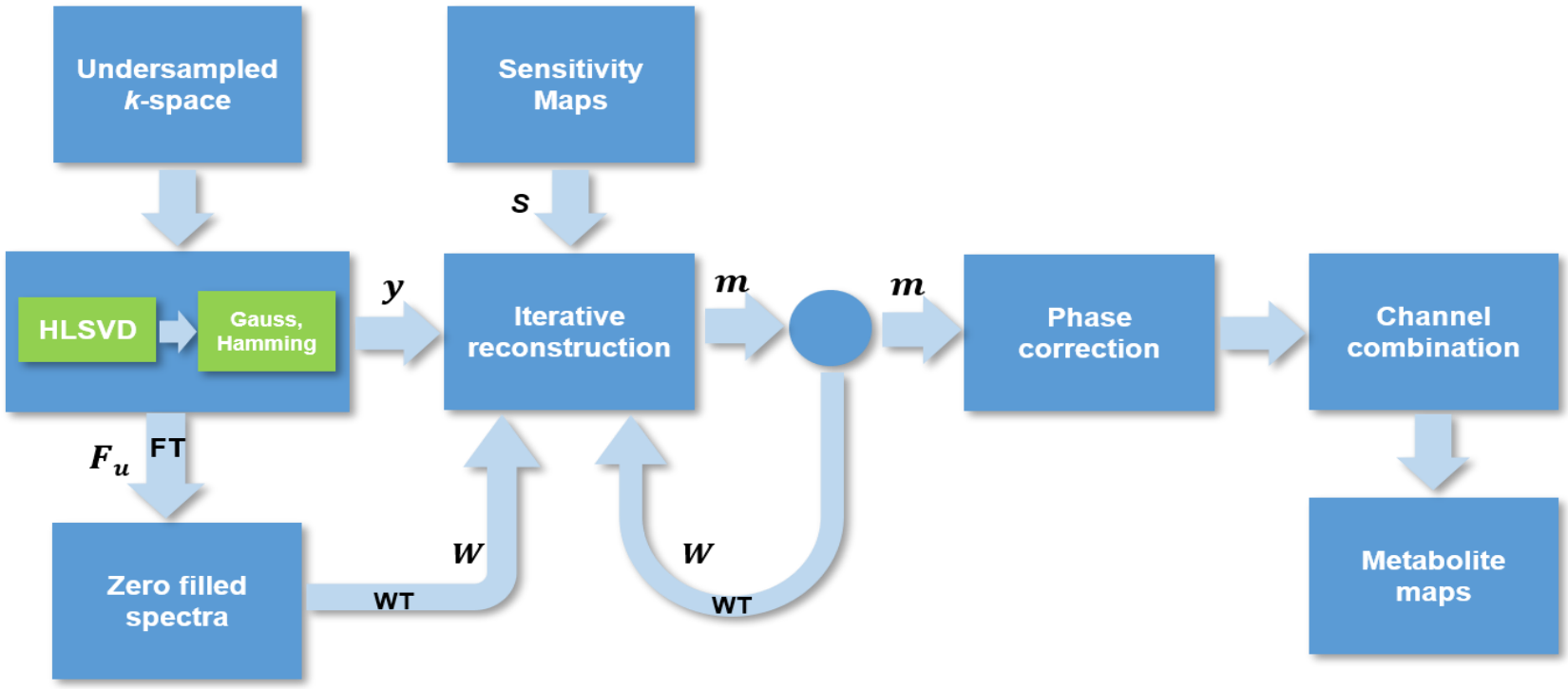

Figure 5.2: CS-MRSI with ROS support workflow

reconstructions to the proposed support-based reconstruction. Figure 5.3(a) represents the anatomical scout; the yellow box represents the fully sampled spatial spectra for the VOI. The CS-MRSI reconstruction (top row) and the voxel-wise difference plot (bottom row) is shown in the blue box for both prospective and retrospective reconstructions. The support-based CS-MRSI reconstruction (top row) and the voxel wise difference plot (bottom row) is shown in the orange box. The scale for all spectra data plots is the min to max of fully sampled spectra. The scale for all the difference plots is –max to +max of fully sampled spectra. Similarly, figure 5.4 represents the spatial-spectral plot for the variable density undersampled data with respective differences to the fully sampled data shown in the bottom row. The differences observed were the lowest for the *a priori* retrospective and highest for the variable density reconstructions.

Figure 5.5 represents the metabolite map comparison for the retrospective reconstructions of CS-MRSI and support-based CS-MRSI methods. The Cho, Cr, and NAA spatial maps were generated for the spatial-spectral matrix resolution (16×16) and resized to match the anatomical scout resolution (256×256). Similarly, figure 5.6 represents the metabolic map comparison for the prospective reconstructions of CS-MRSI and support-based CS-MRSI methods. The metabolite maps were consistent for the *a priori* reconstruction. The support-based CS-MRSI method had fewer significant differences with respect to the fully sampled spectra in comparison to the conventional CS-MRSI. A low-resolution 16×16 area integrated array is obtained for each of the metabolites; NAA, Creatine, and Choline andresized to a higher resolution 256×256 array and overlaid on the T_2 weighted anatomical scout.

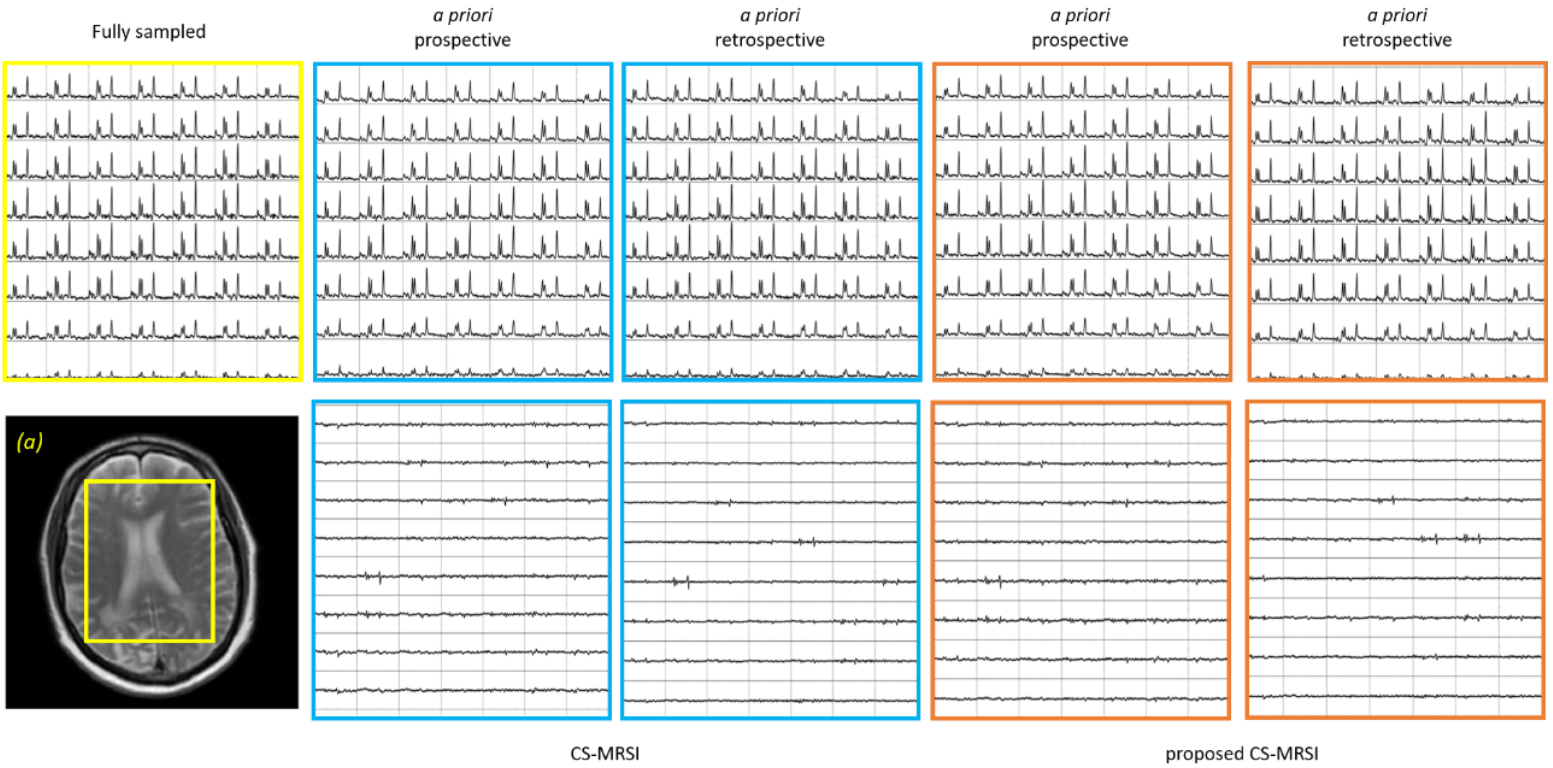

Figure 5.3: Support based CS-MRSI reconstruction spatial spectral comparison. Displays the spectra of the *in vivo* brain of a 52-year-old male subject. (a) T_2 weighted anatomical scout with TE/TR = 104/3000 ms, FOV 22×22 cm, matrix 128x128). Top row: the yellow box represents the fully sampled spectra data, blue box represents the CS-MRSI reconstruction for 5X *a priori*, orange box represents the support-based CS-MRSI reconstruction for 5X *a priori*. Bottom row represents the difference for the respect top row reconstructions to the fully sampled spectra.

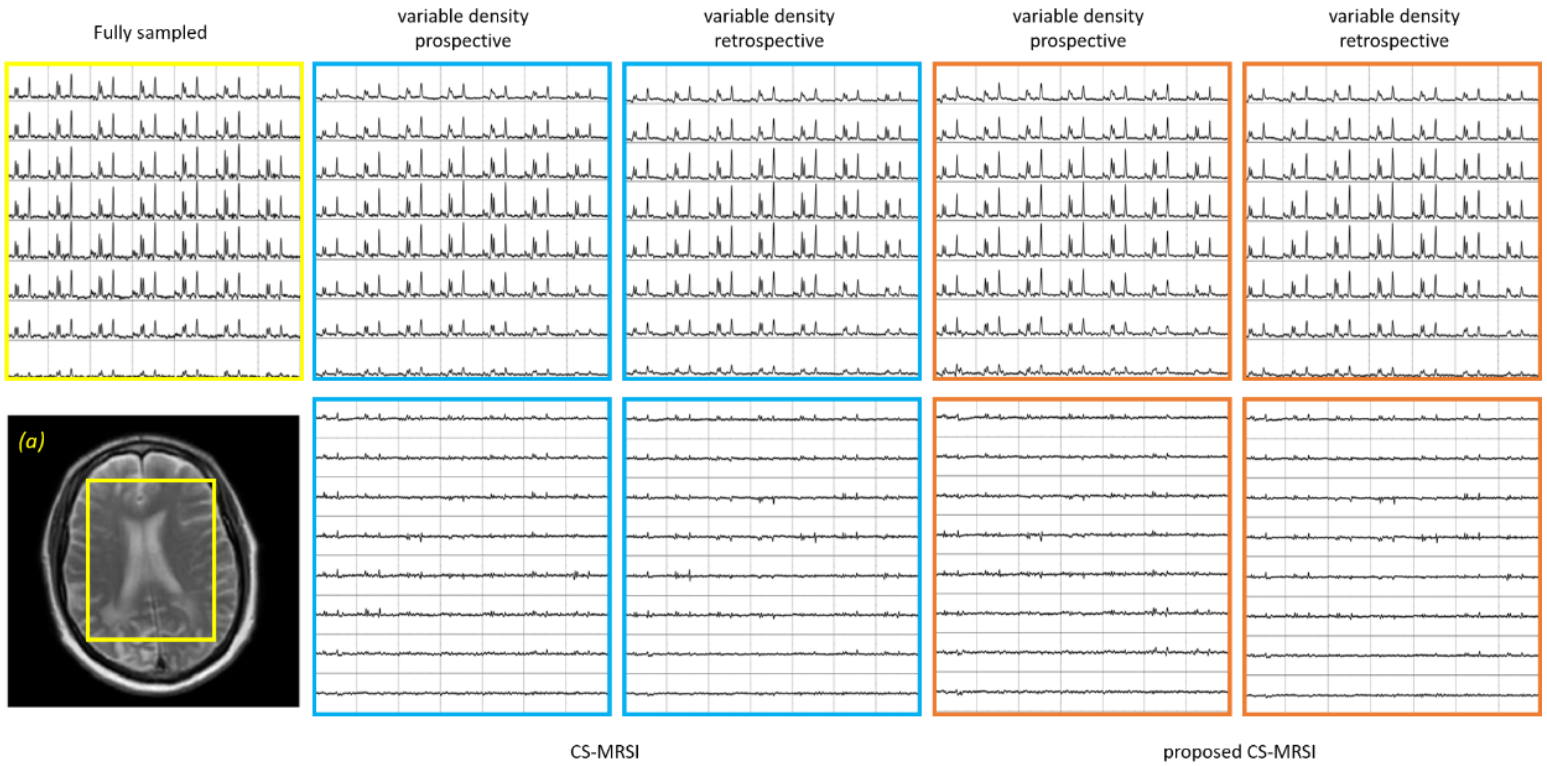

Figure 5.4: Support based CS-MRSI reconstruction spatial spectral comparison. Displays the spectra of the *in vivo* brain of a 52-year-old male subject. (a) T_2 weighted anatomical scout with TE/TR = 104/3000 ms, FOV 22×22 cm, matrix 128×128). Top row: the yellow box represents the fully sampled spectra data, blue box represents the CS-MRSI reconstruction for 5X variable density, orange box represents the support-based CS-MRSI reconstruction for 5X variable density. Bottom row represents the difference for the respect top row reconstructions to the fully sampled spectra.

Figure 5.7 represents the normalized root mean square for the phantom and all nine *in vivo* brain CS-MRSI datasets. The NRMSE Cho, Cr, and NAA metabolites is computed individually for the undersampled CS reconstructed spectra and support based CS-MRSI reconstrued datasets to fully sampled spectra dataset. The error was the lowest for the retrospective *a priori* support based CS-MRSI spectra metabolites and the highest for the prospective CS-MRSI variable density spectra metabolites in most cases. The *p*-value from the paired t-test for the *a priori* reconstructions were > 0.05 whereas most subject data the standard deviations for the variable density and *a priori* CS-MRSI reconstructions and the support-based CS-MRSI reconstructed compared to fully sampled. variable density reconstructions had significant differences ($p<0.05$).

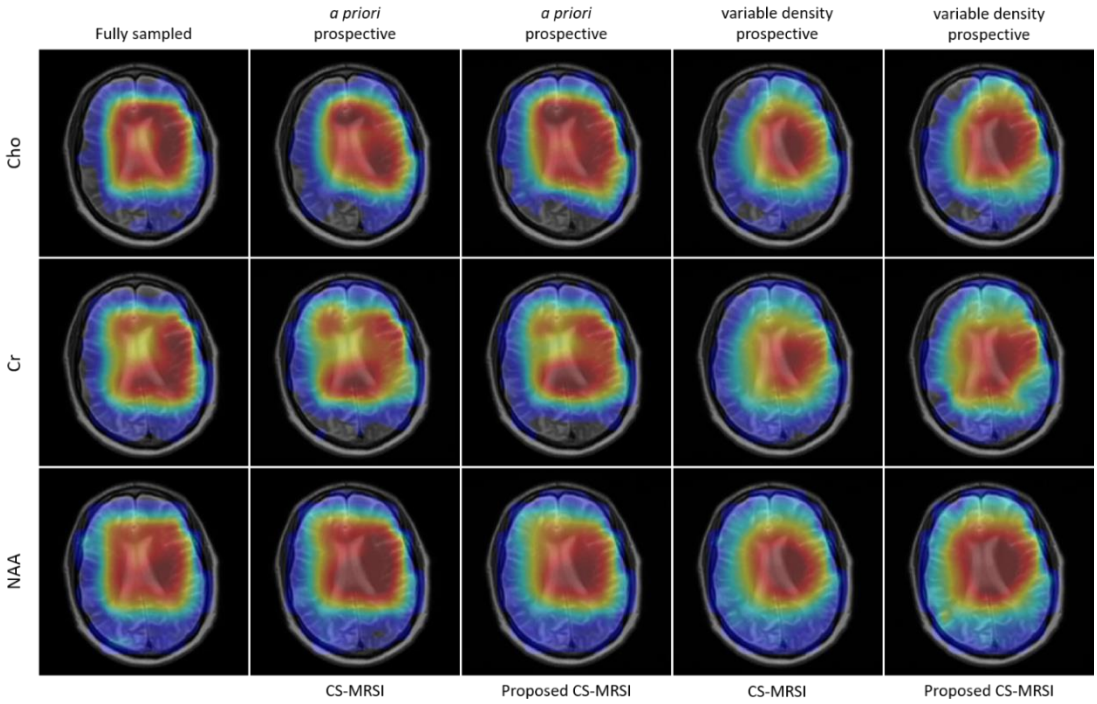

Figure 5.5: *In vivo* brain metabolite maps comparing fully sampled spectra metabolite maps to 5X prospective CS-MRSI reconstred and support based CS-MRSI reconstructed metabolite maps for prospective undersampled data. Metabolite maps are generated for Choline (Cho), Creatine (Cr) and N-acetyl aspartate (NAA) by intergrating the effecting arean under the metabolite peak linewidhs..

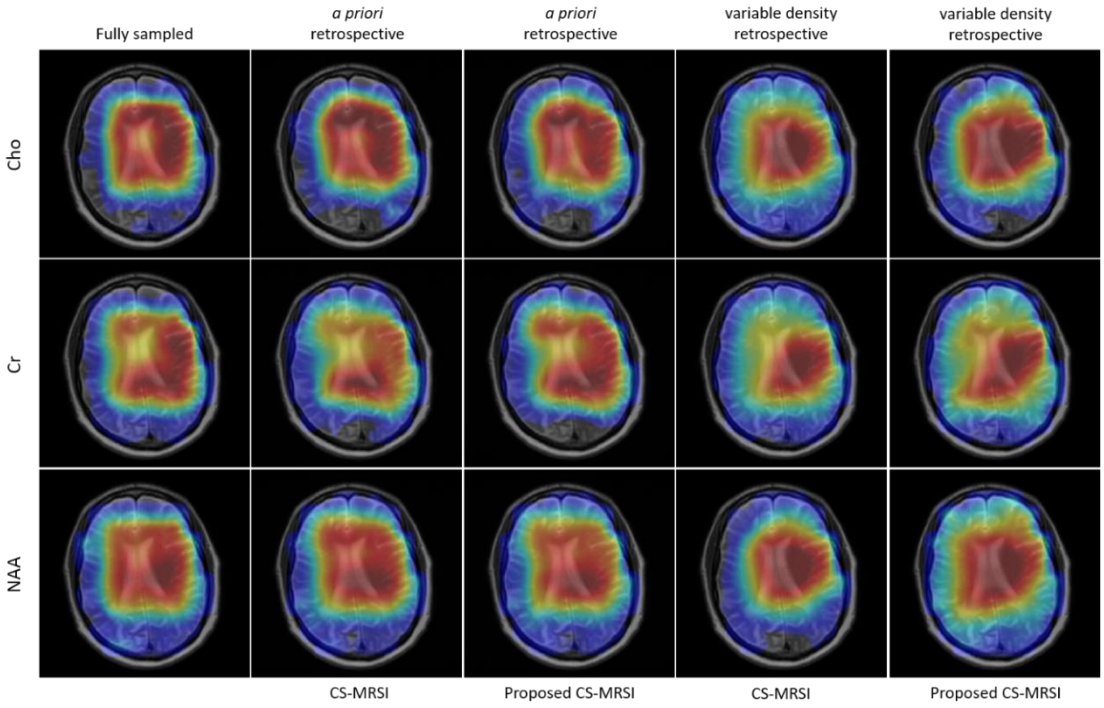

Figure 5.6: *In vivo* brain metabolite maps comparing fully sampled spectra metabolite maps to5X retrospective CS-MRSI reconstred and support based CS-MRSI reconstructed metabolite maps for retrospective undersampled data. Metabolite maps are generated for Choline (Cho), Creatine (Cr) and N-acetyl aspartate (NAA) by intergrating the effecting arean under the metabolite peak linewidhs..

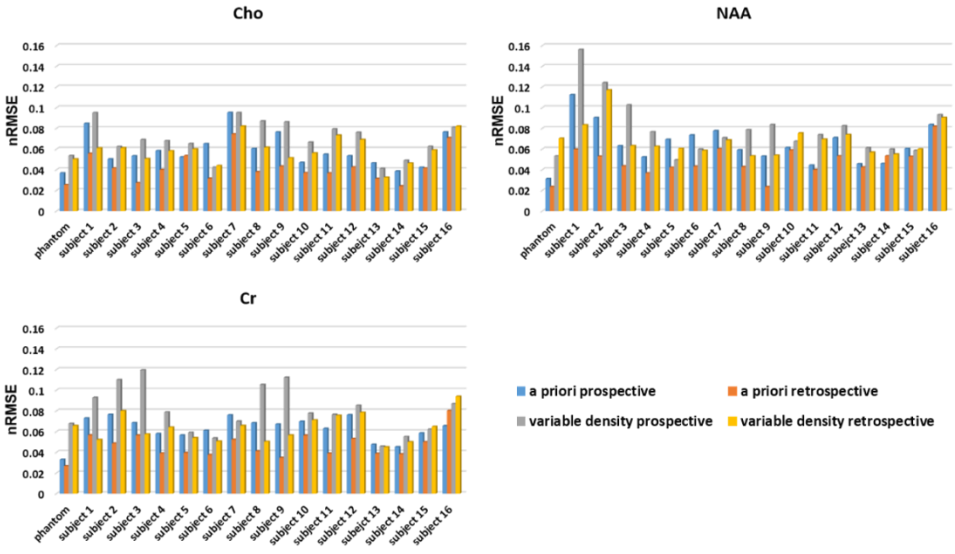

Figure 5.7: Normalized Root Mean Squared Error (nRMSE) plots for voxels located within the selected VOI of the phantom and brain.

5.4 Discussion and Conclusion

We implemented and evaluated a support-based CS-MRSI reconstruction algorithm for *in vivo* ^{1}H multi-channel brain data sets. The results were compared to the CS-MRSI reconstructions in chapter. The nRMSE values for the proposed support-based reconstruction were lower in comparison to the evaluation depicted in figure 3.9. The advantage of including the sensitivity maps in the iterative reconstruction is two-fold: The spectra data under iterative reconstruction is confined to the ROS and therefore thresholds any nuisance spectra outside of the VOI. The other advantage is that the coil weighting factor is translated during the iterative process. Channels with noisy data cannot induce spurious noise peaks as information and thereby improve the overall resolution of the final spectra. Since the same CS weighting factor is used for each channel- despite different noise levels and different object content – the CS reconstruction may not provide the most accurate reconstruction. In this study we use the coil sensitivity maps to aid the convex optimization function wherein an additional weighting parameter *S* is induced into the conjugate gradient algorithm for faster and optimal convergence. The support-based CS-MRSI algorithm converges to a solution at a substantially faster rate and yields lower nRMSE, signifying improved spatial-spectral quality compared to the channel-wise CS-MRSI described in chapter 3. An attempt to improve the variable density undersampling CS-MRSI was made using support information and a significant improvement was achieved. However, the reconstructions for variable density undersampling did not register fidelity to fully sampled spectra. It is important to note that for subject 10 and subject 16, the nRMSE values are higher compared to conventional CS-MRSI for reasons unknown to us at this stage. Further investigation is required to understand these anomalies.

The spatial spectral data acquired during MRSI is confined to the VOI. The effect of ROS support for the VOI region requires further investigation. In our approach the sensitivity maps were obtained from a 128×128 matrix and resized to the 16×16 MRSI data. An effective support would be of the same resolution as the MRSI data however, reducing the matrix size during scout data acquisition would lead to aliasing. Another approach to generate the support information is to obtain the B_0 map from the scanner. This process requires additional scan time. Since the anatomical scout is always acquired during MRSI experiments, it is advantageous to use software methods such as ESPIRiT to generate the necessary sensitivity maps. In chapter 3, the weights for the regularization parameters were same for all channels. The CS-MRSI reconstruction for noisy channels may result in spurious data due to the baseline noise removal efficacy of the iterative process. This substantially effects the effective spectra after coil combination. By using the sensitivity maps during the iterative process, the noisy channels are weighted accordingly therefore avoiding spurious reconstruction.

In conclusion, we have implemented and evaluated a support-based CS-MRSI reconstruction algorithm for ^{1}H multi-channel brain data sets for *a priori* and variable density undersampling. The results show that CS-MRSI reconstruction can be further improved by involving the anatomical support-based sensitivity map in the iterative reconstruction. The proposed algorithm can therefore be used to reconstruct undersampled multi-channel data sets with an improved spatial and spectral resolution for up to an 80% reduction in scan time.

CHAPTER 6

FAST LACTATE IMAGING USING CS-MRSI

6.1 Introduction

Lactate is a product of both aerobic and anaerobic glucose metabolism, normally only produced in small quantities in vivo in limited cell types, under certain conditions. However, in many disease states and under certain physiologic conditions, increased lactate is observed [58, 59]. Tumor cells exhibit enhanced glycolytic metabolism under aerobic and anaerobic conditions [60]. They have also been shown to compromise perfusion and exhibit high interstitial fluid pressure compared to normal tissues due to the absence of functioning lymphatics, increased vascular permeability, and rapid proliferation of cells in confined spaces [61]. Lactate has also been found to stimulate angiogenesis, promote inflammation, and contribute to immune escape [61, 62].

Typically, the increased uptake of glucose is measured by ^{19}F-fluorodeoxyglucose positron emission tomography (PET) studies of tumors [63]. Therefore, imaging lactate can potentially provide the same diagnostic information as ^{19}F-fluorodeoxyglucose positron emission tomography (PET) studies of tumors without the need for radioactivity or any exogenous probes.

The greatest difficulty for the *in vivo* MRSI mapping of lactate is the overlap of the -CH_2- resonance of lipids with the methyl resonance of lactate at 1.3 ppm. As a result, the lactate resonance is often obscured by the resonance of free fatty acids in the tissue of interest, in surrounding tissues, or in the pathological tissues, such as in tumors that contain lipid and lactate [64, 65]. Many techniques have been proposed for editing lactate and can be broadly categorized as difference techniques [66-73] or multiple quantum (MQ) filters

[73-80]. The difference techniques suffer from the fact that any instability in the specimen (patient) or instrument between acquisitions degrades the level of cancellation, resulting in spurious signals. Of the various MQ lactate editing techniques, the double frequency-selective multiple quantum coherence transfer (SelMQC) technique [81] has several advantages. The method detects the lactate signal in a single shot, making it less susceptible to motion and instability than difference and phase cycling methods. The utilization of two frequency-selective pulses tuned to the lactate methyl and methine resonances makes the protocol highly specific for lactate, requiring no water suppression beyond the MQ filter. The present report investigates the feasibility of using the SelMQC method to generate maps of lactate in vivo. Two-dimensional (2D) spatial encoding can easily be incorporated into the SelMQC pulse sequence by the introduction of chemical shift imaging (CSI) gradients in one of the evolution periods of the sequence.

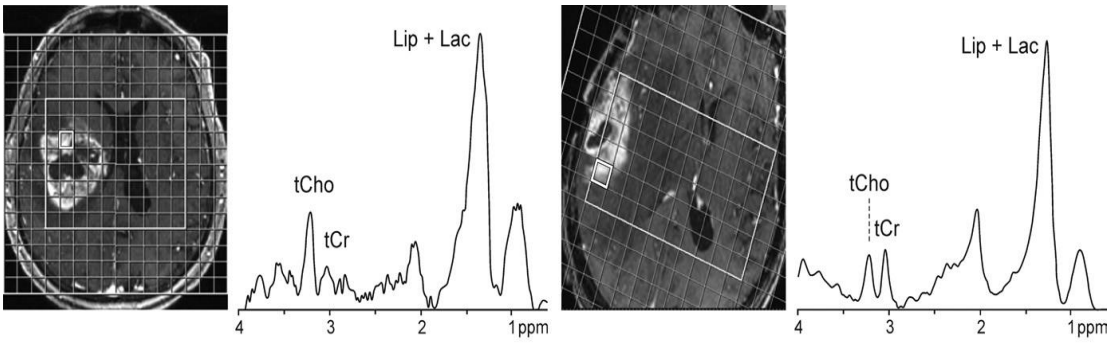

Figure 6.1: ^{1}H MR spectroscopy in glioblastomas. (a) patient with recurrent glioblastoma multiforme. (b) histologically proven case of post-radiation injury. Reproduced from [66].

6.1.1 Lactate Detection in ^{1}H MRSI

Lactate is essentially a J-coupled metabolite, with the methine (-CH) and methyl groups (-CH_3) forming an A_3X spin system [82] . Even at low magnetic fields, the scalar-

coupled spin system of lactate is considered to be weakly coupled [83]. The -CH_3 moiety is responsible for the doublet located at 1.31 ppm in the NMR spectrum, while the –CH moiety is responsible for the quartet at 4.1 ppm (Figure 5.2). The doublet is more commonly acquired but accurate detection and quantification are often complicated by the presence of macromolecules and huge overlapping resonances from lipid in the 0.8 – 1.3 ppm range. It is often difficult to detect the quartet at 4.1 ppm *in vivo* due to its proximity to water. Longer echo times (TE) are usually employed when acquiring the lactate peak to minimize contamination from the lipid resonances.

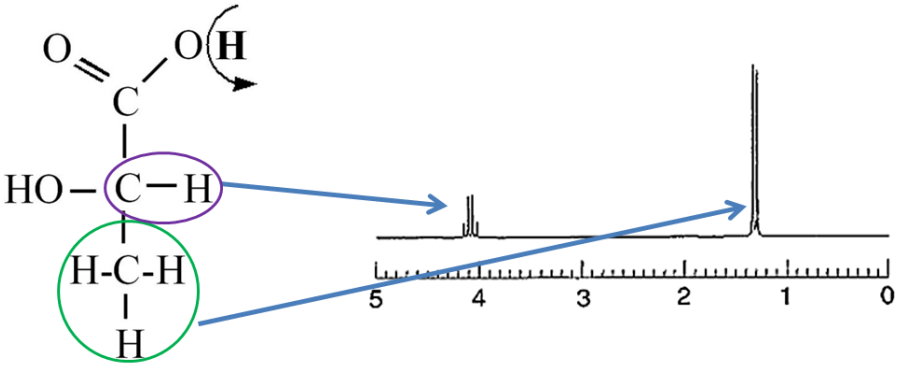

Figure 6.2: An illustration of the lactate molecule and its corresponding NMR spectrum. The CH_3 group produces the doublet at 1.31 ppm, while the CH moiety is responsible for the quartet located at 4.1 ppm.

6.1.2 Lactate Selective Multiple Quantum Coherence

Spectral editing techniques seek to separate the overlapping resonances and quantify the harder to detect metabolites like lactate, citrate, GABA (γ-Aminobutyric acid), and 2-hydroxyglutarate (2HG) to name a few. Such low concentration metabolites can be selectively recorded with specific acquisition schemes that retain only the metabolite peaks of interest while eliminating any interfering resonances particularly those from water and fat [84]. Pulse sequence optimization and a strict assessment of the specificity achieved by

the editing technique will ensure more reliable detection of these smaller metabolites [84]. The selective multiple-quantum coherence transfer (Sel-MQC) sequence developed by He *et al* [81] is one such spectral editing sequence that achieves selective water. A 2D MRSI implementation of the Sel-MQC sequence is depicted in Figure 3.4 (adapted from [87]) and involves the three distinct stages elucidated below for lactate excitation, selection, and detection.

(a) Preparation

The first part of the pulse sequence involves converting the lactate resonance into the multiple quantum coherence (MQC) state. A frequency-selective 90^o RF pulse is applied to excite fat and the CH_3 moiety corresponding to the lactate doublet. Scalar coupling (J), chemical shifts (ω_0), and B_0 field inhomogeneity effects contribute to the evolution of these single quantum coherences (SQCs). Following time $\tau = 1/2J$, where J = 6.93 Hz for lactate, a second 90^0 pulse is applied at the -CH peak frequency to convert the lactate magnetization into the MQC (zero and double quantum coherences, ZQ and DQ) mode, while all other resonances remain in the SQC mode.

(b) Gradient Selection & Labeling

A set of coherence selection gradients, namely g_1, g_2, and g_3, are applied in a specific ratio to select either the ZQ → DQ (0: -1:2) or DQ → ZQ (1:0:2) pathway of lactate. These coherence selection gradients act as a multiple quantum filter allowing only the MQCs from lactate to pass through, while at the same time dephasing all resonances in the SQ mode. The CH_3-selective 180^o pulse applied in

the middle of the gradient labeling period helps to refocus the B_0 inhomogeneity and chemical shift and eliminate J-modulation effects.

(c) Detecting the lactate doublet

The final stage of the pulse sequence involves acquiring the lactate doublet. A CH-selective 90° 'read' pulse applied at the beginning of the detection period converts the MQCs of lactate back into the SQ mode. This is necessary as the final signal can only be detected and acquired when in the SQ mode. The gradient g_3 applied during the time interval τ' refocuses the pathway selected during the prior gradient labeling period.

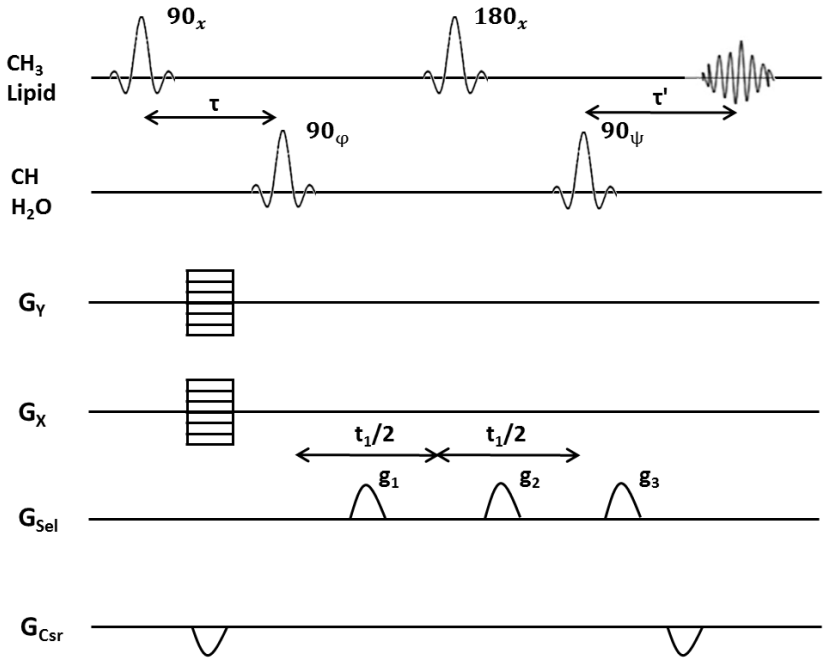

Figure 6.3: A 2D MRSI pulse sequence with lactate-specific editing based on the Sel-MQC technique. Adapted from [24].

Selection of either the ZQ → DQ or DQ → ZQ pathway allows a 50% recovery of the lactate signal intensity. Both pathways need to be refocused simultaneously to obtain

complete recovery of the lactate signal. All other resonances experience a set of unbalanced gradients and are completely dephased.

The objective of this study was to develop and implement CS based selective MQC for rapid lactate editing on a clinical scanner. The nuisance signals are filtered out by spectral editing leading to a reliable detection of the lactate peak.

6.2 Materials and Methods

6.2.1 Pulse Sequence

The lactate-CS-MRSI pulse sequence, depicted in Figure 6.3, was developed and implemented on a GE Discovery 3T clinical scanner. PRESS MRSI sequence from GE with Environment for pulse programming in C (EPIC) software package. The pulse sequence simulated for the current study is as shown in figure 6.4. Tailored RF pulses were introduced for frequency selection. Additional gradients were added as quantum filters. Spectral editing components were added to a conventional PRESS MRSI pulse sequence to enable selection of the ZQ → DQ pathway of lactate. Variable density and *a priori* undersampling patterns were generated to undersample the *k*-space.

6.2.2 Phantom Studies

All experiments were conducted on a GE Discovery 3 T clinical MRI scanner. Three phantom models were used in the study to determine reproducibility. The first phantom was developed to determine the efficacy of the SelMQC sequence to suppress water and fat. Three cylinders with 50 mM, 100 mM lactic acid solution and canola oil in an aqueous solution contained distilled water, copper sulphate, and salt was used as shown

in figure 6.5. Another phantom was designed to determine the resolving power of the SelMQC sequence. The sampling tubes were of three different sizes (1.0 cm, 1.5 cm and 2.6 cm, diameter) containing 25 mM, 50 mM and 100 mM concentration of lactic acid. For an additional validation, braino spectroscopy phantom (GE) was used to determine the efficacy of the sequence for *in vivo* applications. MR acquisition parameters were as follows: 16 × 16 × 1024 matrix, TE/TR = 144/1500 ms, 10 mm slice thickness, number of averages = 1, spectral width = 2500 Hz. The data acquisition time for the PRESS and fully sampled lactate SelMQC sequence was 6 min 4 sec. For the 5X *a priori* and variable density undersampling for SelMQC, the data acquisition time was 1 min 22 sec each. Auto and manual shimming was performed for reliable linewidth during the PRESS scan. The shim and frequency parameters remained same for the rest of the experiment.

6.2.3 CS-MRSI Reconstruction

A custom non-linear iterative reconstruction based on the conjugate gradient algorithm was implemented in MATLAB (The MathWorks Inc., MA) to reconstruct all the lactate-CS-MRSI datasets. The CS-MRSI reconstruction was formulated as a convex optimization problem, which involved minimizing the following cost function:

$$€(m) = \|F_u m - y\|_2 + \lambda_{L1}\|Wm\|_1 + \lambda_{TV} TV(m) \quad (5.1)$$

where, y is the measured *k*-space data, m is the desired MRSI data, F_u, W, and TV are the Fourier transform, wavelet transform, and total variation operators, respectively, $\|.\|_1$ and $\|.\|_2$ are the l_1 and l_2 norm operators, respectively, and, λ_{LI} and λ_{TV} are the

corresponding regularization parameters for the L_1 norm and TV operator, respectively. The k_x - t matrix was encoded along each of the two dimensions using the Daubechies wavelet transform at all points in k_y. The regularization terms λ_{TV} and λ_{LI} were experimentally determined to be 0.005 and 0.001, respectively. Eight iterations were found to be optimal to obtain convergence of the cost function.

6.2.4 Post processing and Error Metric

All reconstructed lactate CS-MRSI datasets were quantitatively compared with the 1X fully sampled reference dataset by evaluating metrics like the SNR, lactate peak amplitude, and the total acquisition time. In each case, the error in reconstruction, as defined by the root mean square error (RMSE) metric was calculated as:

$$RMSE = \sqrt{\frac{1}{N}\sum_{i=1}^{N}(y_i - y_i')^2} \tag{5.2}$$

Where, N is the total number of points in the MRSI dataset, y is the reconstructed data from the fully sampled (1X) *k*-space, and y' is the data reconstructed from undersampled *k*-space. The RMSE defined here can be equivalent to the normalized RMSE as the data range was normalized from 0 to 1.

6.2.5 Statistical Analysis

A voxel-wise 2-tailed paired t-test was applied to the lactate maps generated from each reconstructed dataset with the fully sampled reference dataset using the GraphPad Prism (San Diego, CA, USA) scientific software. A p-value < 0.05 was considered statistically significant and indicative of an incorrect reconstruction.

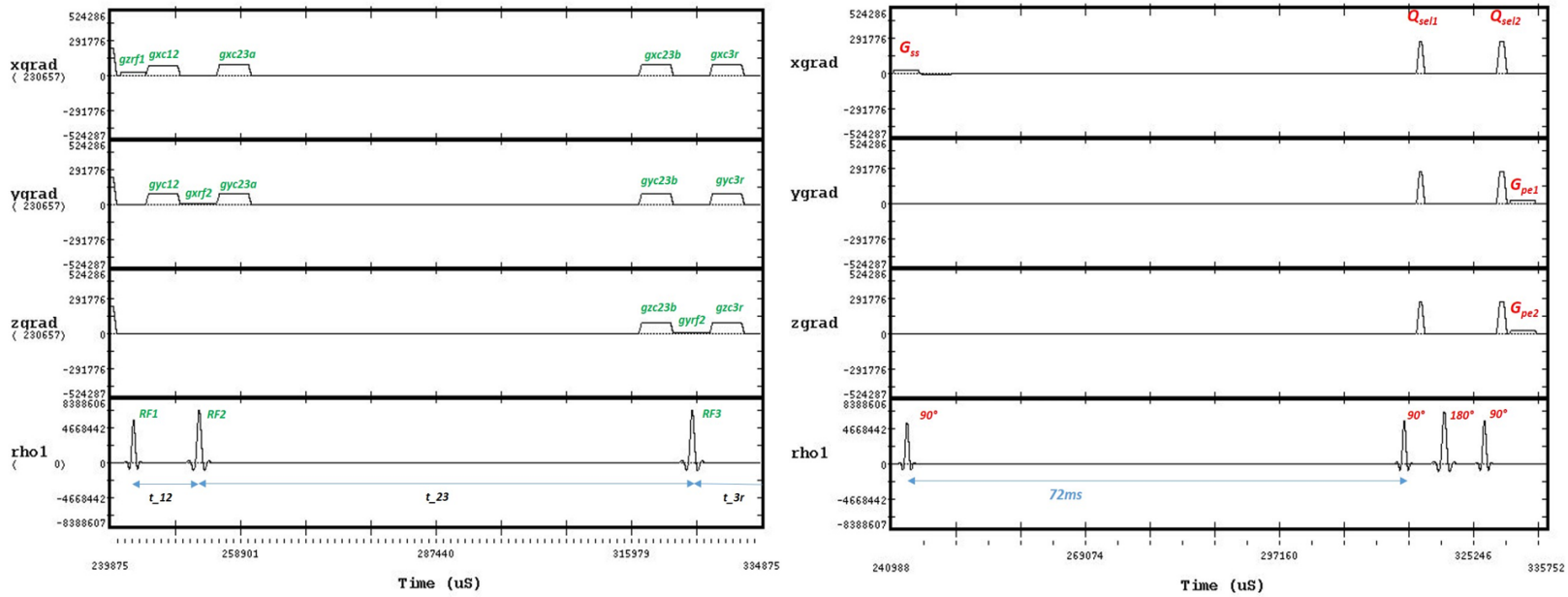

PRESS pulse sequence

SelMQC pulse sequence

Figure 6.4: SelMQC pulse sequence implementation (WTools, GE). The SelMQC was designed based on the PRESS MRSI sequence by modifying the gradient pulse amplitudes and timings Tailored RF pulses were designed and using RF tool (WTools).

6.3 Results

Figure 6.5 represents the spectral data from a water/oil/lactate phantom. The PRESS MRSI in figure 6.5(b) has all the three spectral components in the respective voxel locations. The lactate peak is at 1.3 ppm and is difficult to observe among the dominating fat and water peaks. The fat peaks have a large linewidth spanning from 0 ppm to 4 ppm. The lactate selective SelMQC acquisition in figure 6.5(c) shows the resolved lactate peaks with complete suppression of fat and water. A trace amount of unsuppressed water and fat was also observed. This is due to the tail ends of large water and fat peaks occupying other

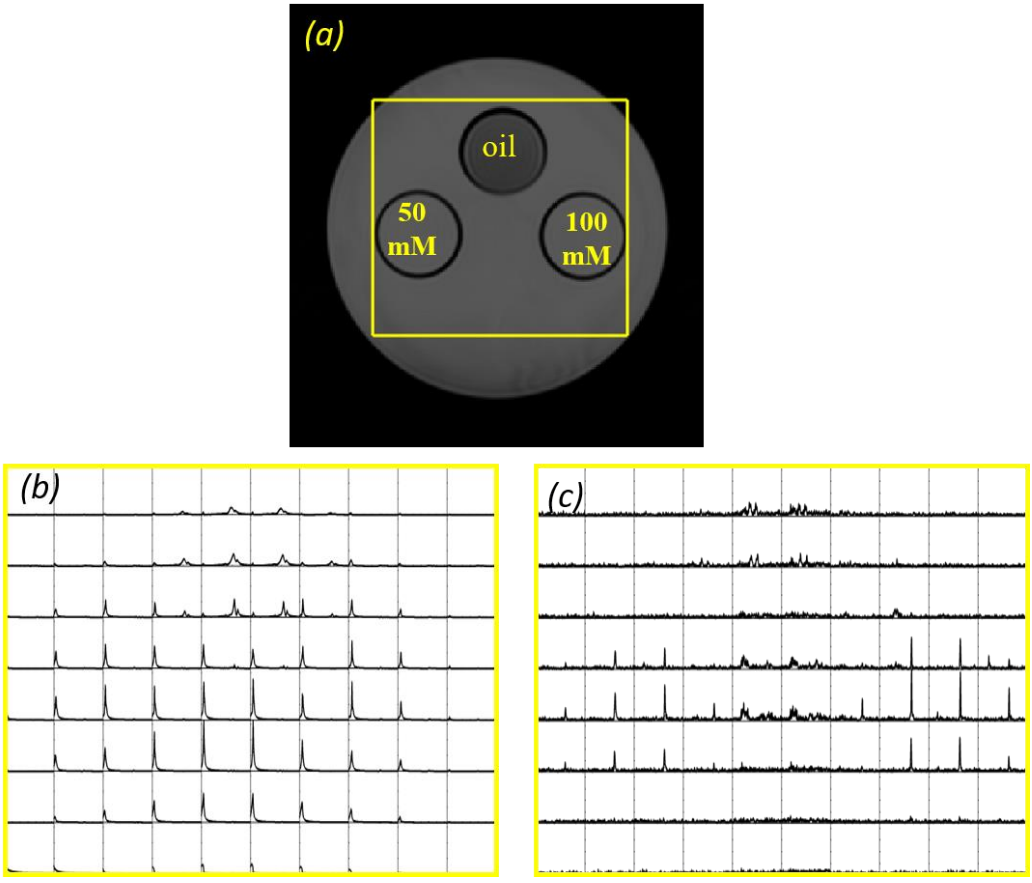

Figure 6.5: Water/oil/lactate phantom. (a) Coronal T_2 weighted image of the water/oil/lactate phantom. (b) PRESS acquisition showing larger water and fat peaks. (c) Lactate SelMQC with complete water and fat suppression. Y-axis scale normalized to largest peak, x-axis scale: -2 ppm to 5 ppm (right to left)

spectral regions. The lactate peaks from SelMQC where 50% lower in amplitude when measured against the PRESS-MRSI. Additional tests on spherical braino phantom show in figure 5.6 validates the efficacy of the SelMQC. Complete water suppression is achieved with no traces of other peaks in the 0.5 ppm to 4 ppm range except lactate.

Figure 6.6 displays the CS-MRSI reconstructions for the variable density and *a priori* undersampling strategies for a 5X undersampled prospective data. The nRMSE for the reconstructions were below 4 % and the *p*-value was > 0.05 indicating no significant differences compared to the fully sampled data.

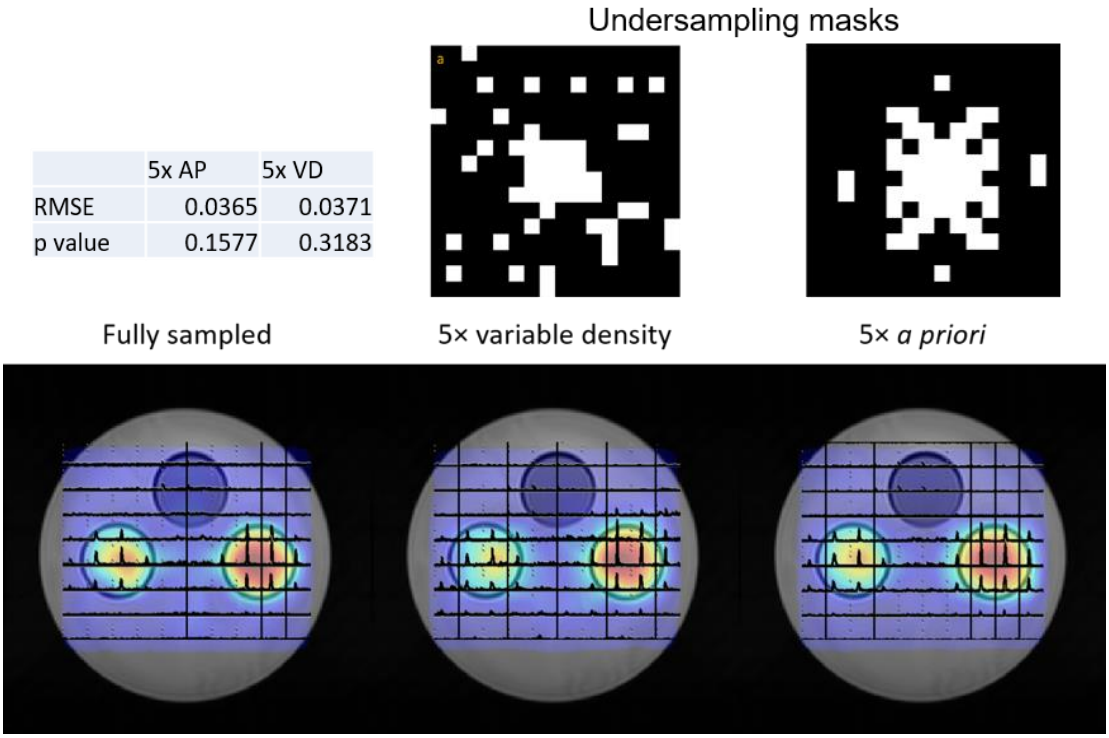

Figure 6.6: Lactate metabolite maps for water/oil/lactate phantom. Comparing undersampled CS reconstruction to fully sampled data

Figure 6.7 depicts the lactate detection in a spherical brain mimicking phantom (braino phantom, GE Healthcare). The phantom comprises of all major brain metabolites such as water, NAA, Cr, Cho, myo-inositol. The concentration of lactate in the solution is about 5 mM. The signals from water, NAA, Cr, Cho and other metabolites are completely suppressed with retention of lactate signal. The sequence was accelerated using CS with variable density and *a priori* undersampling strategies for 5X acceleration. Figure 6.8 shows the undersampling patterns and the CS reconstructed metabolite maps. The CS reconstruction failed for the variable density undersampling with a p value < 0.05. The *a priori* undersampling strategy demonstrates high fidelity with the fully sampled spectra.

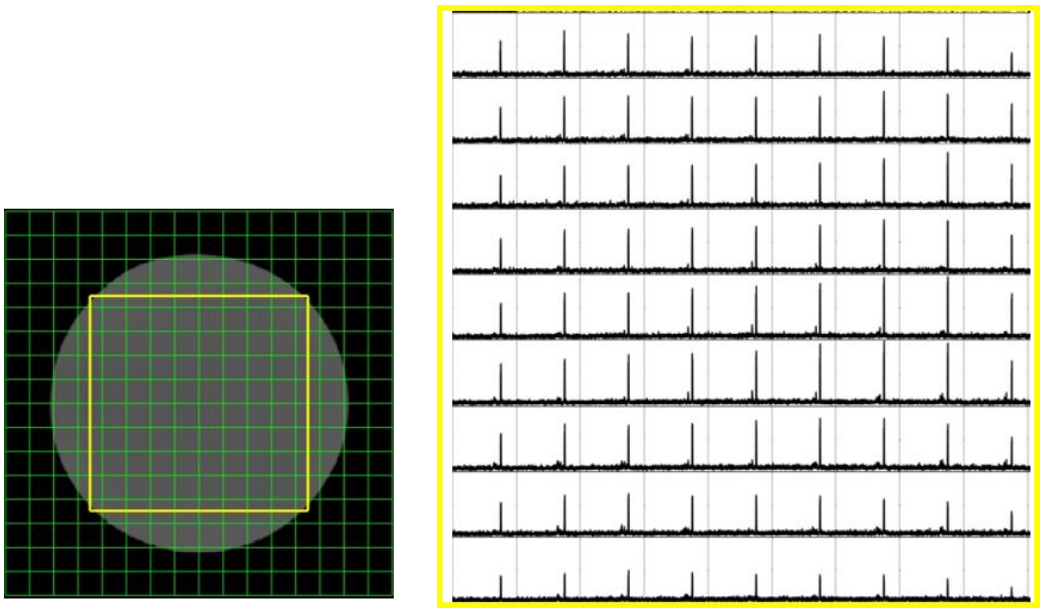

Figure 6.7: SelMQC data acquisition on braino phantom. (a) displays the T_2 axial image of the spherical phantom. (b) displays the lactate only peak acquired with SelMQC pulse sequence. X-axis scale: 0.5 ppm to 4 ppm (right to left).

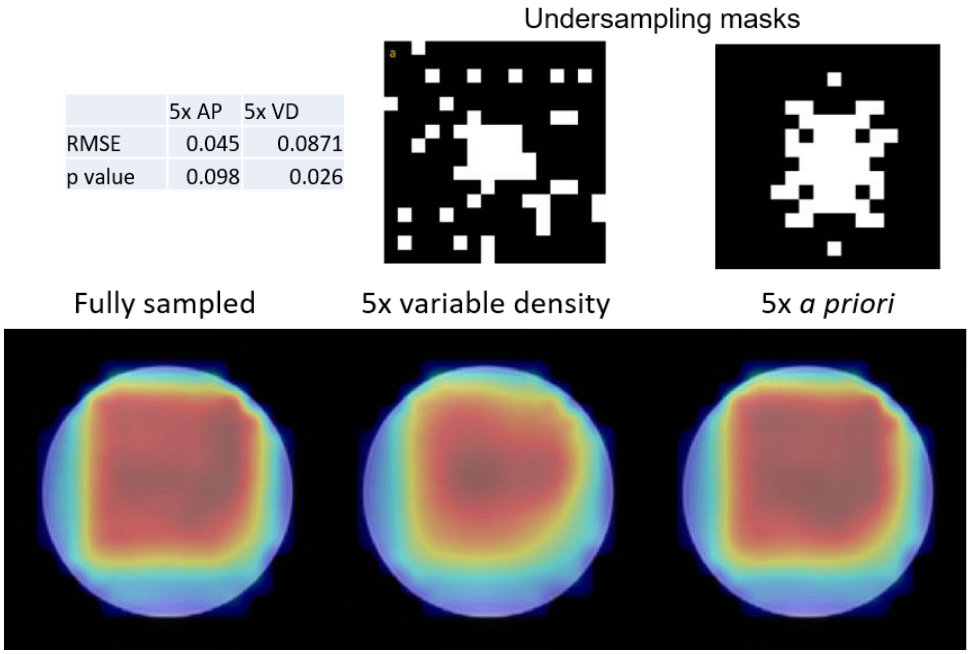

Figure 6.8: Lactate metabolite maps for the braino phantom. Comparison of undersampled CS reconstruction to fully sampled data

6.4 Discussion and conclusion

The results presented on phantoms demonstrate the feasibility of fast lactate measurement with the CS accelerated SelMQC technique at the clinic. Lactate detection with water and lipid suppression is possible by the application of frequency selective RF excitation and inversion pulses at 1.3 ppm and 4.1 ppm and the use of strong gradients as quantum filters. The current implementation allows the choice of the different pathways for lactate detection. In both ZQ-DQ and DQ-ZQ pathways, only 50 % of the lactate signal was achieved. Full lactate signal recovery is possible by employing both the pathways with a phase-cycling of lactate CH-pulse. This approach increases scan time and is susceptible to patient motion and therefore not recommended for *in vivo* studies.

One of the important aspects of lactate detection is single-frequency excitation. The frequency precision of the RF pulses is inversely proportional to their duration. Increasing the RF pulse duration leads to loss of signal due to molecular diffusion and J-modulation effects. In our experiment, sinc pulses were designed on WTools (GE Healthcare) for frequency-selective excitation for 100 Hz. A trade-off was necessary in selecting excellent frequency selective RF pulses and duration. Methods for tailored RF pulses for frequency selection are studied extensively. Binomial RF pulse excitation in SelMQC developed by Thakur et al. [86] has been demonstrated to improve the signal detection of lactate.

For the water/oil/lactate phantom, residual water and fat peaks with amplitudes less than the lactate are observed. The canola oil used in the experiment has small resonant peaks at 2 ppm and 2.8 ppm which were not completely suppressed. Complete suppression of this water and fat can be theoretically possible by increasing the gradient strength of the quantum filters. At a clinical front, the use of strong gradients with short ramp times may cause eddy currents, peripheral nerve stimulation (PNS), and increased acoustic noise which leads to patient discomfort. In our phantom experiments, the amplitudes for Qsel gradients were 14 mT/m and 28 mT/m which are considered safe. Further *in vivo* testing may be required to account for patient experience during the experiment.

The ability to directly measure the lactate distribution in solid tumors can prove to be significantly beneficial as this metabolite is a key marker of altered metabolism, possible malignancy, and tumor hypoxia. As previously discussed, tumor metastasis and recurrence have been linked to elevated lactate concentrations, while variations during radiotherapy and treatment can provide insights into the efficacy of a therapeutic strategy. While various MRI sequences are capable of measuring tumor characteristics such as perfusion, apparent

diffusion coefficient (ADC), and pO2, MRSI is the only technique that can map the spatial heterogeneity of lactate in cancer. The developed 1H lactate-CS-MRSI sequence could potentially be beneficial for a regular assessment of lactate changes in the clinic, particularly to assess and personalize therapeutic outcomes. The method is specifically useful in monitoring tumors close to the cranium which is often affected by the overlapping fat resonances. Other applications of the SelMQC techniques are found in the detection of polyunsaturated fatty acids (PUFA) in human breasts [87]. In their study, fast spiral SelMQC was developed for rapid detection of PUFA which can be further accelerated by employing compressed sensing.

In conclusion, SelMQC MRSI offers a good means of lipid suppression while maintaining good lactate detection efficacy. Lactate was successfully measured in both the phantoms. Fast lactate MRSI was implemented in the clinical setting with a reduction in the acquisition time by up to 80%. Further study with this method will include its application in *vivo* brain tumor cases to study lactate in non-enhancing peritumoral regions and evaluation of lactate in extracranial tumors.

CHAPTER 7

CONCLUSION AND FUTURE DIRECTION

Long MR spectroscopic imaging acquisition times represent a significant limitation to its widespread use in the clinic. Although conventional MRI is comparatively fast and provides significant information regarding the structure and location of the disease it is necessary to quantify and determine the biological properties to aid in the development of tailored therapeutic strategies. Acceleration methods can fundamentally improve the diagnosis by providing a significantly large amount of information within the study duration. The rapid examination protocols could potentially offer other benefits like reduced costs, increased patient throughput, less patient discomfort, and lower susceptibility to motion artifacts. Such advancements are critical for the establishment of sophisticated yet affordable patient care. The compressed sensing method has been established to provide the necessary acceleration at the clinic. Recently, the major vendors have started employing CS for MRI and have demonstrated its acceleration capabilities for up to three-fold. Despite the technical developments and considerable application of CS-MRI, there is little attention to the development of CS-MRSI. To our knowledge, this is the first study to translate CS-MRSI at the clinic and demonstrate fast MRSI during routine clinical studies. A rigorous evaluation of the performance of CS-MRSI is undertaken with undersampling strategies for a five-old reduction in scan time.

7.1 Clinical CS-MRSI

A detailed description of the clinical development and implementation of CS-MRSI is in chapter 3. The prospective application of CS-MRSI was demonstrated on 16 patients

scanned for various brain-related concerns. Informed consent was obtained from the subjects identified for the study with a request for an additional 15 to 30 mins of their time on the scanner. Fully sampled conventional MRSI and undersampled CS-MRSI data was acquired following the routine MRI protocol. Two key undersampling strategies were employed for a 5X reduction in scan time in 16 patients. Additionally, 3X undersampled data was acquired for 5/16 patients of the same population. The variable density method used a pseudo-random pattern and the *a priori* method used the anatomical *k*-space. A CS reconstruction pipeline for multi-channel undersampled MRSI data was developed on MATLAB. The CS reconstructions for the *a priori* undersampling maintained high fidelity and statistical similarity with the fully sampled reference data. The variable density undersampling strategy failed to register fidelity with fully sampled data.

The data acquisition of MRSI data involves complicated steps like B_0 shimming and water/lipid suppression, which play a critical role in determining the quality of MRSI data. This would require specialized operator training as in most cases a manual optimization of the above parameters is required to achieve the desired spectral quality. One of the drawbacks of this study was its application limited to brain studies. Other potential organs such as prostrate, liver and muscles were not included since they are affected by motion. Apparent patient motion also occurred during the fully sampled and undersampled data acquisition for the brain. A comparison of fully sampled and undersampled *k*-space had minor errors which later propagated during CS reconstruction. This is evident from the differences in the retrospective and prospective evaluation.

For CS-MRSI, several post-processing operations were needed to be applied before presenting the final metabolite maps/spectra for interpretation. One of the challenges

during post-processing was the large water and fat peaks. In presence of water and fat signals, the CS reconstruction algorithm solves for the large peaks resulting in significant loss of metabolite information in the denoising process, leading to their poor resolution. To avoid such reconstructions, we employed channel-wise water and fat suppression routine before iterative reconstruction. Further post-processing of spectra data involves phase correction followed by coil combination. However, for the multi-channel undersampled *k*-space data, the phase correction in the spatial spectral domain introduces data in the undersampling zero points in *k*-space resulting in poor CS reconstruction. One way to address this issue is to phase correct during the iterative reconstruction which requires phasing and de-phasing of data for each iteration. This substantially increases the computational time and therefore was avoided.

The non-linear iterative CS reconstruction preserves the spectral line shapes but at the same time causes a gradual smoothing of the spectra with increasing acceleration. This is due to the denoising introduced by the wavelet and total variation terms in the CS reconstruction algorithm. CS denoising could lead to a smoothing of smaller metabolites that are close to the noise floor in the MRS spectrum, thus, presenting the disadvantage of missing these less prominent signals altogether. This dissertation focused on the larger metabolites, namely, NAA, creatine, choline, and lactate, which appear as prominent peaks in the MRS spectrum. However, there are other smaller metabolites such as alanine, glycine, glutamate, ^{2}HG, and myo-inositol that are important biomarkers and relatively hard to detect. In such cases, the reconstruction algorithm would need to be tailored to ensure a reliable representation of low concentration metabolites at higher accelerations, especially when the acquired MRSI data is SNR limited.

The time gained by employing the CS-MRSI approach can be further utilized to obtain a higher resolution or boost the SNR by increasing the number of averages. This SNR is critical for low concentration metabolite imaging. Furthermore, metabolite selective sequence combined with CS-MRSI can be employed for their rapid imaging. Chapter 5 describes one such method, the lactate SelMQC wherein the dominant water and fat peaks are completely suppressed. The only drawback of this study was that it was performed *in vitro*. The method was tested on multiple phantoms for validation. The CS reconstruction for the undersampled data showed high fidelity with the fully sampled acquisition.

7.2 Future Direction

The inclusion of MRSI in scan protocols is essential for a true multi-parametric assessment of cancer, on both the clinical and preclinical fronts. The information from various MRI sequences like diffusion-weighted imaging (DWI), dynamic contrast-enhanced imaging (DCE), and MRSI would enable the clinician to assess different parameters and variations from voxel-to-voxel, leading to potentially improved diagnosis and treatment strategies. The non-invasive extraction of various quantitative parameters like the tumor perfusion, pO_2, apparent diffusion coefficient (ADC), and metabolite concentrations necessitates a multi-modality approach that achieves a differential gain in information from different techniques that probe cancer metabolism. An optimal trade-off between various parameters like the resolution, SNR, sensitivity, penetration depth, artifacts, imaging speed, and costs will facilitate a more comprehensive multi-parametric assessment in cancer targeting and therapeutics. Patient tolerance is minimal during long

scan times and motion during long MRSI studies is expected. Comparative studies for anesthetized studies can be done. However, it is not recommended in a clinical setting unless advised in the exam. Other approaches to remedy motion correction is to using navigators for fast MRSI can be considered in future implementations.

The success of *a priori* undersampling over variable density undersampling is attributed to its ability to target the most significant points in *k*-space. The current implementation uses the combined scout *k*-space to determine the encoding regions. For higher acceleration, the *a priori* undersampling is confined to lower frequencies in *k*-space resulting in voxel bleeding among neighboring voxels. This effect can be mitigated by sampling a few higher frequency points in *k*-space. A combination of *a priori* undersampling and variable density undersampling can be effective in acquiring the significant points in *k*-space as well as a few higher frequency points. An illustration of a combined undersampling pattern is as shown in figure 7.1. In this retrospective example, the effective acceleration is 70%. The retrospective reconstructions for the combination approach are shown in figure 7.2. Pilot study yielded improved reconstruction with a slight decrease in acceleration.

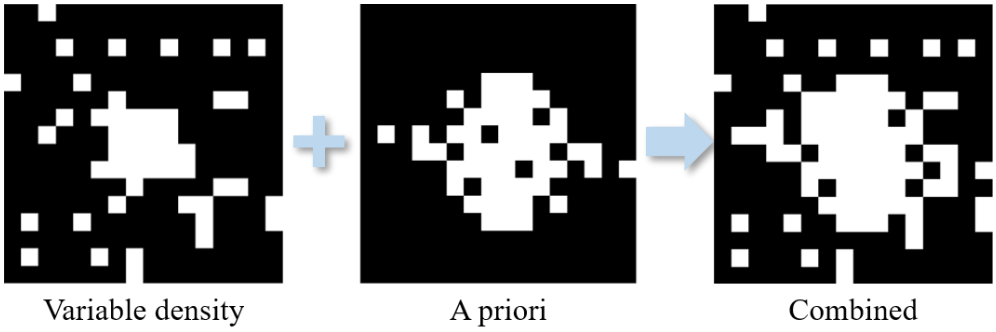

Figure 7.1: Hybrid undersampling pattern obtained by combining *a priori* and variable density undersampling. The effective sampling is 30%.

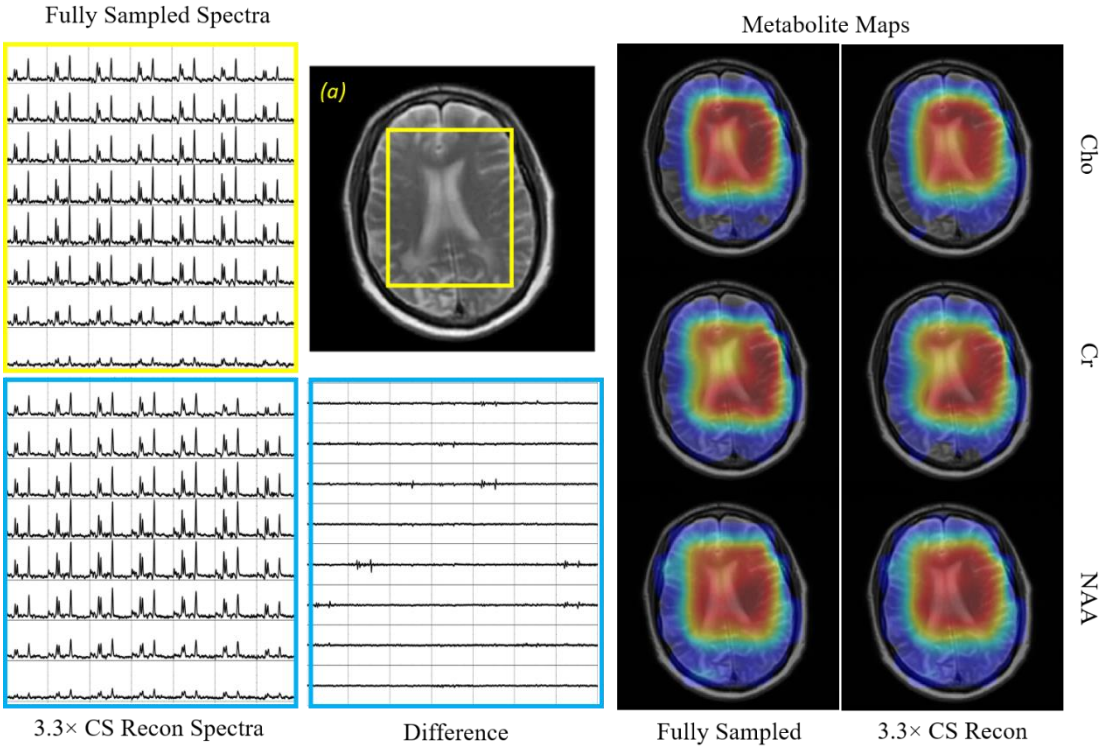

Figure 7.2: Retrospective reconstruction for proposed *a priori* and variable density combined undersampling CS-MRSI

In this work, the *a priori* undersampling patterns are generated based on the *k*-space of the anatomical scout. The effective *k*-space comprises signals from both the water and fat regions. Since MRSI data acquisition is affected by overlapping fat resonances from the skull and is avoided by selecting a VOI, it is beneficial to generate *a priori k*-space information for the VOI. However, it is impossible to obtain anatomical images for a reduced MRSI VOI FOV with conventional techniques due to aliasing. Inner FOV echo planar imaging (EPI) [88] using blipped gradient during the frequency excitation can be sed to generate the necessary inner *k*-space for a more accurate *a priori* undersampling pattern generation. Another approach to improve the *a priori* undersampling is to consider

channel-wise undersampling followed by an effective weighted combination. A channel-wise undersampling can prove to be efficient especially in parallel MRSI.

In the current implementation, the *a priori* undersampling pattern generation and the post-processing reconstructions are done offline. Future implementation of *a priori* CS-MRSI can be done online by parsing the scout information to a thresholding subroutine within the scanner. Vendor support is required for compatible implementation. For CS-MRSI, a channel-wise reconstruction takes ~ 1 hour 30 min for a 2D MRSI dataset on a 3 GHz computer, with larger grid sizes and datasets of higher dimensionality requiring more computation time. Parallel processing and the use of efficient graphical processing units (GPUs) can improve the reconstruction time. An efficient post-processing pipeline compatible with the scanner software is required for future online processing and data display.

REFERENCES

1. Hajek, M. and M. Dezortova, Introduction to clinical in vivo MR spectroscopy. Eur J Radiol, 2008. **67**(2): p. 185-93.

2. Kreis R. Quantitative localized 1H MR spectroscopy for clinical use. Prog Nucl Magn Reson Spectrosc 1997;31(2-3):155-195.

3. Williams S. Cerebral amino acids studied by nuclear magnetic resonance spectroscopy in vivo. Prog Nucl Magn Reson Spectrosc 1999;34(3–4):301-326.

4. Howe FA, Opstad KS. 1H MR spectroscopy of brain tumours and masses. NMR Biomed 2003;16(3):123-131.

5. Barker P. B., Bizzi A., DeStefano N., Gullapalli R., M. LDD. Clinical MR Spectroscopy: Techniques and Applications: Cambridge University Press; 2009.

6. Choi C, Ganji SK, DeBerardinis RJ, Dimitrov IE, Pascual JM, Bachoo R, Mickey BE, Malloy CR, Maher EA. Measurement of glycine in the human brain in vivo by 1H-MRS at 3 T: application in brain tumors. Magn Reson Med 2011;66(3):609-618.

7. Choi C, Ganji SK, DeBerardinis RJ, Hatanpaa KJ, Rakheja D, Kovacs Z, Yang XL, Mashimo T, Raisanen JM, Marin-Valencia I, Pascual JM, Madden CJ, Mickey BE, Malloy

8. J. Kurhanewicz, D. B. Vigneron, and S. J. Nelson, "Three-dimensional magnetic resonance spectroscopic imaging of brain and prostate cancer," Neoplasia, vol. 2, pp. 166-89, Jan-Apr 2000.

9. P. J. Bolan, S. Meisamy, E. H. Baker, J. Lin, T. Emory, M. Nelson, L. I. Everson, D. Yee, and M. Garwood, "In vivo quantification of choline compounds in the breast with 1H MR spectroscopy," Magn Reson Med, vol. 50, pp. 1134-43, Dec 2003.

10. H. M. Baik, M. Y. Su, H. Yu, R. Mehta, and O. Nalcioglu, "Quantification of choline-containing compounds in malignant breast tumors by 1H MR spectroscopy using water as an internal reference at 1.5 T," MAGMA, vol. 19, pp. 96-104, May 2006.

11. A. Shukla-Dave, H. Hricak, C. Moskowitz, N. Ishill, O. Akin, K. Kuroiwa, J. Spector, M. Kumar, V. E. Reuter, J. A. Koutcher, and K. L. Zakian, "Detection of prostate cancer with MR spectroscopic imaging: an expanded paradigm incorporating polyamines," Radiology, vol. 245, pp. 499-506, Nov 2007.

12. J. M. Duarte, H. Lei, V. Mlynarik, and R. Gruetter, "The neurochemical profile quantified by in vivo 1H NMR spectroscopy," Neuroimage, vol. 61, pp. 342-62, Jun 2012.

13. E. M. Spur, E. A. Decelle, and L. L. Cheng, "Metabolomic imaging of prostate cancer with magnetic resonance spectroscopy and mass spectrometry," Eur J Nucl Med Mol Imaging, vol. 40 Suppl 1, pp. S60-71, Jul 2013.

14. T. Kobus, A. J. Wright, T. W. Scheenen, and A. Heerschap, "Mapping of prostate cancer by 1H MRSI," NMR Biomed, vol. 27, pp. 39-52, Jan 2014.

15. Spielman, D.M., E. Adalsteinsson, and K.O. Lim, Quantitative assessment of improved homogeneity using higher-order shims for spectroscopic imaging of the brain. Magn Reson Med, 1998. **40**(3): p. 376-82.

16. Zierhut, M.L., et al., (1)H spectroscopic imaging of human brain at 3 Tesla: comparison of fast three-dimensional magnetic resonance spectroscopic imaging techniques. J Magn Reson Imaging, 2009. **30**(3): p. 473-80.

17. M. Lustig, D. Donoho, and J. M. Pauly, "Sparse MRI: The application of compressed sensing for rapid MR imaging," Magn Reson Med, vol. 58, pp. 1182-95, Dec 2007.

18. Geethanath S, Baek HM, Ganji SK, Ding Y, Maher EA, Sims RD, Choi C, Lewis MA, Kodibagkar VD. Compressive sensing could accelerate 1H MR metabolic imaging in the clinic. Radiology. 2012 Mar;262(3):985-94. doi: 10.1148/radiol.11111098.

19. Rohini Vidya Shankar, Houchun Harry Hu, Nutandev Bikkamane Jayadev, John C. Chang, and Vikaram D. Kodibagkar "2D MR Spectroscopic Imaging of the Pediatric Brain using Compressed Sensing". Pediatric Radiology. 2019 (Accepted/in press). PRAD-D-19-00008.

20. Rohini Vidya Shankar, Houchun Harry Hu, Nutandev Bikkamane Jayadev, John C. Chang, and Vikaram D. Kodibagkar "Undersampling strategies for compressed sensing accelerated MR spectroscopic imaging", Proc SPIE 10137, Medical Imaging 2017: Biomedical Applications in Molecular, Structural, and Functional Imaging, 101372l (13 March 2017); https://doi.org/10.1117/12.2254614.

21. C.P. Slichter, Principles of Magnetic resonance, rd ed., Springer-Verlag, New York, 1990.85

22. Macomber RS. A complete introduction to modern NMR spectroscopy. Nova York 1998.

23. Levitt MH. Spin dynamics: basics of nuclear magnetic resonance: John Wiley & Sons; 2008.

24. Ernst RR, Bodenhausen G, Wokaun A. Principles of nuclear magnetic resonance in one and two dimensions: Clarendon Press; 1987.

25. Abraham A. The Principles of Nuclear Magnetism, 1963, 313. Oxford University Press, London.

26. Bottomley, P.A., Spatial localization in NMR spectroscopy in vivo. Ann N Y Acad Sci, 1987. 508: p. 333-48.

27. Haase, A., J. Frahm, W. Hanicke, et al., 1H NMR chemical shift selective (CHESS) imaging. Phys Med Biol, 1985. 30(4): p. 341-4.

28. Ernst, T. and J. Hennig, Improved water suppression for localized in vivo 1H spectroscopy. J Magn Reson B, 1995. 106(2): p. 181-6.

29. Star-Lack, J., S.J. Nelson, J. Kurhanewicz, et al., Improved water and lipid suppression for 3D PRESS CSI using RF band selective inversion with gradient dephasing (BASING). Magn Reson Med, 1997. 38(2): p. 311-21.

30. Star-Lack, J., D.B. Vigneron, J. Pauly, et al., Improved solvent suppression and increased spatial excitation bandwidths for three-dimensional PRESS CSI using phase-compensating spectral/spatial spin-echo pulses. J Magn Reson Imaging, 1997. 7(4): p. 74557.

31. Duyn, J.H., J. Gillen, G. Sobering, et al., Multisection proton MR spectroscopic imaging of the brain. Radiology, 1993. 188(1): p. 277-82.

32. Tran, T.K., D.B. Vigneron, N. Sailasuta, et al., Very selective suppression pulses for clinical MRSI studies of brain and prostate cancer. Magn Reson Med, 2000.43(1): p. 23-33

33. M. van der Graaf, "In vivo magnetic resonance spectroscopy: basic methodology and clinical applications," *Eur Biophys J,* vol. 39, pp. 527-40, Mar 2010.

34. N. Salibi and M. A. Brown, *Clinical MR Spectroscopy First Principles*: John Wiley & Sons, Inc., 1998.

35. H. Zhu and P. B. Barker, "MR spectroscopy and spectroscopic imaging of the brain," *Methods Mol Biol,* vol. 711, pp. 203-26, 2011.

36. D. P. Soares and M. Law, "Magnetic resonance spectroscopy of the brain: review of metabolites and clinical applications," *Clin Radiol,* vol. 64, pp. 12-21, Jan 2009.

37. R. N. Al-Okaili, J. Krejza, S. Wang, J. H. Woo, and E. R. Melhem, "Advanced MR imaging techniques in the diagnosis of intraaxial brain tumors in adults," *Radiographics,* vol. 26 Suppl 1, pp. S173-89, Oct 2006.

38. M. Dezortova, F. Jiru, J. Petrasek, V. Malinova, J. Zeman, M. Jirsa, and M. Hajek, "1H MR spectroscopy as a diagnostic tool for cerebral creatine deficiency," *MAGMA,* vol. 21, pp. 327-32, Sep 2008.

39. P. R. Carroll, F. V. Coakley, and J. Kurhanewicz, "Magnetic resonance imaging and spectroscopy of prostate cancer," *Rev Urol,* vol. 8 Suppl 1, pp. S4-S10, 2006.

40. P. Cao and E. X. Wu, "Accelerating phase-encoded proton MR spectroscopic imaging by compressed sensing," *J Magn Reson Imaging,* vol. 41, pp. 487-95, Feb 2015.

41. E. J. Candes, J. Romberg, and T. Tao, "Robust uncertainty principles: Exact signal reconstruction from highly incomplete frequency information," *Ieee Transactions on Information Theory,* vol. 52, pp. 489-509, Feb 2006.

42. S. Geethanath, R. Reddy, A. S. Konar, S. Imam, R. Sundaresan, R. R. D, and R. Venkatesan, "Compressed sensing MRI: a review," *Crit Rev Biomed Eng,* vol. 41, pp. 183-204, 2013.

43. J. L. Starck, M. Elad, and D. L. Donoho, "Image decomposition via the combination of sparse representations and a variational approach," *IEEE Trans Image Process,* vol. 14, pp. 1570-82, Oct 2005.

44. D. S. Taubman and M. W. Marcellin, *JPEG2000 : image compression fundamentals, standards, and practice*. Boston: Kluwer Academic Publishers, 2002.

45. J. K. Furuyama, N. E. Wilson, B. L. Burns, R. Nagarajan, D. J. Margolis, and M. A. Thomas, "Application of compressed sensing to multidimensional spectroscopic imaging in human prostate," *Magn Reson Med,* vol. 67, pp. 1499-505, Jun 2012.

46. R. Nagarajan, Z. Iqbal, B. Burns, N. E. Wilson, M. K. Sarma, D. A. Margolis, R. E. Reiter, S. S. Raman, and M. A. Thomas, "Accelerated echo planar J-resolved spectroscopic imaging in prostate cancer: a pilot validation of non-linear reconstruction using total variation and maximum entropy," *NMR Biomed,* Sep 7 2015.

47. M. K. Sarma, R. Nagarajan, P. M. Macey, R. Kumar, J. P. Villablanca, J. Furuyama, and M. A. Thomas, "Accelerated echo-planar J-resolved spectroscopic imaging in the human brain using compressed sensing: a pilot validation in obstructive sleep apnea," *AJNR Am J Neuroradiol,* vol. 35, pp. S81-9, Jun 2014.

48. S. Hu, M. Lustig, A. P. Chen, J. Crane, A. Kerr, D. A. Kelley, R. Hurd, J. Kurhanewicz, S. J. Nelson, J. M. Pauly, and D. B. Vigneron, "Compressed sensing for resolution enhancement of hyperpolarized 13C flyback 3D-MRSI," *J Magn Reson,* vol. 192, pp. 258-64, Jun 2008.

49. S. Hu, M. Lustig, A. Balakrishnan, P. E. Larson, R. Bok, J. Kurhanewicz, S. J. Nelson, A. Goga, J. M. Pauly, and D. B. Vigneron, "3D compressed sensing for highly accelerated hyperpolarized (13)C MRSI with in vivo applications to transgenic mouse models of cancer," *Magn Reson Med,* vol. 63, pp. 312-21, Feb 2010.

50. P. E. Larson, S. Hu, M. Lustig, A. B. Kerr, S. J. Nelson, J. Kurhanewicz, J. M. Pauly, and D. B. Vigneron, "Fast dynamic 3D MR spectroscopic imaging with compressed sensing and multiband excitation pulses for hyperpolarized 13C studies," *Magn Reson Med,* vol. 65, pp. 610-9, Mar 2011.

51. N. C. Askin, B. Atis, and E. Ozturk-Isik, "Accelerated phosphorus magnetic resonance spectroscopic imaging using compressed sensing," *Conf Proc IEEE Eng Med Biol Soc,* vol. 2012, pp. 1106-9, 2012.

52. T. Kampf, A. Fischer, T. C. Basse-Lusebrink, G. Ladewig, F. Breuer, G. Stoll, P. M. Jakob, and W. R. Bauer, "Application of compressed sensing to in vivo 3D (1)(9)F CSI," *J Magn Reson,* vol. 207, pp. 262-73, Dec 2010.

53. Roemer PB, Edelstein WA, Hayes CE, Souza SP, Mueller OM. The NMR phased array. Magn Reson Med. 1990; 16(2):192–225. [PubMed: 2266841]

54. Hardy CJ, Bottomley PA, Rohling KW, Roemer PB. An NMR phased array for human cardiac 31P spectroscopy. Magn Reson Med. 1992; 28(1):54–64. [PubMed: 1435221]

55. Gnahm C, Bock M, Bachert P, Semmler W, Behl NG, Nagel AM.Iterative 3D projection reconstruction of23Na data with an1H MRIconstraint. Magn Reson Med 2014;71(5):1720–32.

56. Gnahm C, Nagel AM. Anatomically weighted second-order total varia-tion reconstruction of23Na MRI using prior information from1H MRI.Neuroimage 2015;105:452–61.

57. Uecker M, Lai P, Murphy MJ, et al. ESPIRiT—an eigenvalue approach to autocalibrating parallel MRI: where SENSE meets GRAPPA. Magn Reson Med. 2014;71:990-1001.

58. Gatenby RA, Gillies RJ. Why do cancers have high aerobic glycolysis? Nat Rev Cancer 2004;4:891–899

59. Bui T, Thompson CB. Cancer's sweet tooth [comment]. Cancer Cell 2006;9:419–420.

60. M. G. V. Heiden, L. C. Cantley, and C. B. Thompson, "Understanding the Warburg Effect: The Metabolic Requirements of Cell Proliferation," Science, vol. 324, pp. 1029-1033, May 22, 2009.

61. Jain RK. Transport of molecules in the tumor interstitium: a review. Cancer Res 1987;47:3039–3051.

62. J. R. Doherty and J. L. Cleveland, "Targeting lactate metabolism for cancer therapeutics," J Clin Invest, vol. 123, pp. 3685-92, Sep 2013.

63. F. Hirschhaeuser, U. G. Sattler, and W. Mueller-Klieser, "Lactate: a metabolic key player in cancer," Cancer Res, vol. 71, pp. 6921-5, Nov 15 2011.

64. Czernin J, Phelps ME. Positron emission tomography scanning: current and future applications. Annu Rev Med 2002;53:89–112.

65. Li X, Vigneron DB, Cha S, Graves EE, Crawford F, Chang SM, Nelson SJ. Relationship of MR-derived lactate, mobile lipids, and relative blood volume for gliomas in vivo. AJNR Am J Neuroradiol 2005;26:760–769.

66. Oz et al. Clinical Proton MR Spectroscopy in Central Nervous System Disorders, RSNA 2014

67. Rothman DL, Behar KL, Hetherington HP, Shulman RG. Homonuclear 1H double-resonance difference spectroscopy of the rat brain in vivo. Proc Natl Acad Sci USA 1984;81:6330–6334.

68. Wild JM, Marshall I. In vivo lactate editing in single voxel proton spectroscopy and proton spectroscopic imaging by homonuclear polarization transfer. Magn Reson Imaging 1999;17:131–139.

69. Adalsteinsson E, Spielman DM, Pauly JM, Terris DJ, Sommer G, Macovski A. Feasibility study of lactate imaging of head and neck tumors. NMR Biomed 1998;11:360–369.

70. Shen J, Novotny EJ, Rothman DL. In vivo lactate and beta-hydroxybutyrate editing using a pure-phase refocusing pulse train. Magn Reson Med 1998;40:783–788.

71. Reese T, Norris DG, Leibfritz D. A fast method for in vivo lactate imaging. NMR Biomed 1995;8:225–231.

72. Adalsteinsson E, Spielman DM, Wright GA, Pauly JM, Meyer CH, Macovski A. Incorporating lactate/lipid discrimination into a spectroscopic imaging sequence. Magn Reson Med 1993;30:124–130.

73. Marjanska M, Henry PG, Bolan PJ, Vaughan B, Seaquist ER, Gruetter R, Uurbil K, Garwood M. Uncovering hidden in vivo resonances using editing based on localized TOCSY. Magn Reson Med 2005;53:783–789.

74. Lei H, Dunn J. The effects of slice-selective excitation/refocusing in localized spectral editing with gradient-selected double-quantum coherence transfer. J Magn Reson 2001;150:17–25.

75. de Graaf RA, Luo Y, Terpstra M, Garwood M. Spectral editing with adiabatic pulses. J Magn Reson Ser B 1995;109:184–193.

76. Lei H, Peeling J. Simultaneous lactate editing and observation of other metabolites using a stimulated-echo-enhanced double-quantum filter. J Magn Reson 1999;137:215–220.

77. Keltner JR, Wald LL, Ledden PJ, Chen YC, Matthews RT, Kuestermann EH, Baker JR, Rosen BR, Jenkins BG. A localized double-quantum filter for the in vivo detection of brain glucose. Magn Reson Med 1998;39: 651–656.

78. Jouvensal L, Carlier PG, Bloch G. Practical implementation of singlevoxel double-quantum editing on a whole-body NMR spectrometer: localized monitoring of lactate in the human leg during and after exercise. Magn Reson Med 1996;36:487–490.

79. Lazeyras F, Terrier F, Aue WP, Frey FJ, Howarth N. Measurement of lactate in acutely ischemic rat kidneys using magnetic resonance spectroscopy. Invest Radiol 1994;29:24–30.

80. Kingsley PB. Scalar coupling and zero-quantum coherence relaxation in STEAM: implications for spectral editing of lactate. Magn Reson Med 1994;31:315–319.

81. He Q, Shungu DC, van Zijl PC, Bhujwalla ZM, Glickson JD. Single-scan in vivo lactate editing with complete lipid and water suppression by selective multiple-quantum-coherence transfer (Sel-MQC) with application to tumors. J Magn Reson Ser B 1995;106:203–211.

82. V. Govindaraju, K. Young, and A. A. Maudsley, "Proton NMR chemical shifts and coupling constants for brain metabolites," NMR Biomed, vol. 13, pp. 129-53, May 2000.

83. R. A. d. Graaf, In Vivo NMR Spectroscopy: Principles and Techniques, 2nd ed.: John Wiley & Sons Ltd., 2007.

84. A. Naressi, C. Couturier, I. Castang, R. de Beer, and D. Graveron-Demilly, "Java-based graphical user interface for MRUI, a software package for quantitation of in

vivo/medical magnetic resonance spectroscopy signals," Comput Biol Med, vol. 31, pp. 269-86, Jul 2001.

85. Q. He, D. C. Shungu, P. C. van Zijl, Z. M. Bhujwalla, and J. D. Glickson, "Single-scan in vivo lactate editing with complete lipid and water suppression by selective multiple-quantum-coherence transfer (Sel-MQC) with application to tumors," *J Magn Reson B,* vol. 106, pp. 203-11, Mar 1995.

86. S. B. Thakur, J. Yaligar, and J. A. Koutcher, "In vivo lactate signal enhancement using binomial spectral-selective pulses in selective MQ coherence (SS-SelMQC) spectroscopy," *Magn Reson Med,* vol. 62, pp. 591-8, Sep 2009.

87. H. Zhu, D Rubin, Q. He, " The fast spiral-selMQC techniqe for in vivo MR spectroscopic imaging of polysaturated fatty acids (PUFA) in human breast tissue," Magn reson Med, vol. 67(1): 8-19, Jan 2012.

88. J Finterbusch, "High-resolution diffusion tensor imaging with inner field-of-view EPI," J. Magn. Reson. Imaging 2009;29:987-993.